Durham E-Theses

Electronic states in semiconductor superlattices and quantum wells

Hughes, D.T.

How to cite:

Hughes, D.T. (1989) *Electronic states in semiconductor superlattices and quantum wells*, Durham theses, Durham University. Available at Durham E-Theses Online: http://etheses.dur.ac.uk/6519/

Use policy

ELECTRONIC STATES IN SEMICONDUCTOR SUPERLATTICES

AND QUANTUM WELLS.

by

D.T. Hughes, M.A.

A thesis submitted for

the Degree of Doctor of Philosophy

at the University of Durham

January 1989

ABSTRACT

The aim of this thesis is two-fold. Firstly to show how a complex bandstructure matching technique has been developed which allows detailed investigations to be made of various low dimensional structures. Secondly the method will be used to investigate interesting physical properties of quantum wells and superlattices.

Consequently the thesis will begin with an exposition of the matching technique, giving an indication of the numerical methods used for computational calculations. Evidence will then be given, in the form of a comparison between the present work and the experimental and theoretical results to be found in the literature, of the efficacy of the method.

A detailed description of results of calculations carried out on the valence band of AlAs/GaAs and AlGaAs/GaAs quantum wells will show how energy levels and wavefunctions have been calculated as well as giving an explanation of hybridisation and anti-crossing effects.

In order to extend the method to strained systems it will be shown how strain can be incorporated into the model by simple empirical fits of calculated bulk properties to experiment. This method will be used to model two particular Si/Ge structures: a $Ge_{0.25}Si_{0.75}/Si/Ge_{0.25}Si_{0.75}$ quantum well and a $(Si)_4(Ge)_4$ superlattice. To allow a better comparison with experiment for the superlattice a description is given of a method for calculating optical matrix elements between superlattice states; and the results of such calculations are discussed.

DECLARATION.

I hereby declare that the work reported in this thesis has not previously been submitted for any degree and is not being currently submitted in candidature for any other degree.

The work reported in this thesis was carried out by the candidate.

PRONUNCIAMENTO.

Many of the results in this thesis have been obtained from computer calculations. In the whole these programs have been written by myself. However, the original bulk complex bandstructure program which forms the core of one of my programs was obtained from Dr. S. Brand.

Some of the following thesis has appeared elsewhere as refereed papers. In particular a large proportion of chapter 4 has been published (Brand and Hughes, 1987). Chapter 6 has appeared in published form in two papers (Hughes and Brand, 1987 and Hughes and Brand 1989). Much of chapter 5 has appeared as a privately circulated report (Hughes, 1987).

Figure (2.1) has been taken from the literature (Brand et al, 1987) as have figures (3.11.b) and (3.12.b) (Gell et al, 1986) which have been used for comparison.

The cause of all things is neither soul nor intellect; nor has it imagination, opinion, or reason, or intelligence; nor is it reason or intelligence; nor is it spoken or thought. It is neither number nor order, nor magnitude, nor littleness, nor equality, nor inequality, nor similarity, nor dissimilarity. It neither stands, nor moves, nor rests......

Pseudo-Dionysius.

....it's worse than that: it's physics, Jim.

Star Trekkin'
The Firm.

Acknowledgements.

CONTENTS

Chapter 5. The Complex Bandstructure Method and its Application to Strained Materials.

Chapter 6. Two Particular Examples of SiGe Structures.

CHAPTER ONE

INTRODUCTION

In this thesis we shall deal, in some detail, with two distinct low dimensional structures: the quantum well and the superlattice.

The quantum well has long been treated as a simple physical entity for undergraduate problems and as an abstraction for various real processes such as modelling the atomic nucleus or electrons confined to metals. The synthesis of a real quantum well, i.e. a structure in which one physical dimension is reduced to the order of a wavelength of an electron within that structure, had to wait for the advent of molecular beam epitaxy (M.B.E.) (Arthur, 1968) and metal organic chemical vapour deposition (M.O.C.V.D.) (Manasevit, 1968). The technological impetus of this leap forward was the realisation that if quantum wells could be produced the advantages for laser technology were enormous. In particular the double heterostructure solid state laser could be expected to play a part in many opto-electronic devices.

From an optical viewpoint the advantage of low dimensional structures is a direct consequence of the modified two-dimensional density of states which is sharply peaked at frequencies corresponding to the separation of electron and hole sub-bands, rather than the broad density of states of the

bulk – which varies as $(Energy)^{0.5}$. The electronic advantages of creating two-dimensional structures are manifold with the possibility of creating selectively doped regions which form two dimensional gases with mobilities in excess of $2x10^6 cm^2/VS$ (Weimann and Schlapp, 1985) or structures which exhibit real space charge transfer.

Superlattices, *per se*, however, were not mooted as an idea until 1970 when Esaki and Tsu proposed that by alternating thin layers of different semiconductors it was possible to produce a new 'material' with an extended unit cell which could be varied whilst retaining translational symmetry hence allowing the electronic bandstructure properties of the superlattice to be 'engineered'.

In a sense the idea of alternating energy barriers – which is one way to see the superlattice – had been investigated before by the Kronig-Penney model, and it was in fact the Kronig-Penney model which Esaki used to make the first theoretical comparison with experiment when investigating the negative differential resistance of such structures (Esaki and Chang, 1974).

Soon afterwards a calculation was carried out using a Kronig-Penney model extended to incorporate realistic bandstructure by including a non-parabolicity term in the calculation (Mukherji and Nag, 1975). This calculation was able to show that even this simplistic approach to realistic bandstructure produced results significantly in variance with the simple constant effective mass Kronig-Penney calculation.

Many methods followed which utilised various techniques learnt from

bulk bandstructure calculations; these included a tight-binding complex band-structure method (Schulman and McGill, 1981), a plane wave pseudopotential **k.p** complex bandstructure method (Mailhiot et al, 1984), an envelope function method (Bastard, 1981) and numerous other approaches incorporating various approximations, simplifications and inaccuracies. A small section of the work which has been carried out on AlAs/GaAs superlattices will be discussed in chapter 3 where the range of results for the theoretical calculations will show that it is impossible to claim that one outstanding method exists which can model all cases and circumstances. This thesis will attempt to show how some of the shortcomings of the other methods can be overcome by using a new method of calculation. We shall also indicate how the versatility of our method allows new and interesting physical phenomena to be investigated.

Thesis Plan.

In chapter 2 we shall give a detailed explanation of our complex bandstructure matching technique (CBMT) and how complex bandstructure can be folded down to a two dimensional representation which incorporates all the information necessary to match wavefunctions at interfaces. This simplified form will allow us to solve the Schroedinger equation for any 'two-dimensional' structure. We shall concentrate on two cases

(i) the ABA type superlattice,

(ii) the bound states of a quantum well.

Although the description of our complex bandstructure matching

technique will be rather abstract and mathematical, reference will be given to the appropriate appendices for details of practical computational procedures.

Chapter 3, as has been mentioned, will give an overview of the results for various theoretical and experimental investigations of GaAs/AlAs superlattices. A comparison will also be given of these various results and the results obtained by the CBMT of chapter 2. It will be shown that the CBMT, although relatively simple to implement and powerful in its applicability to many situations, gives results in good agreement with many other larger calculations.

Chapter 4 will deal with two sets of structures: AlAs/GaAs/AlAs and $Al_{0.3}Ga_{0.7}As/GaAs/Al_{0.3}Ga_{0.7}As$ quantum wells. As well as giving a detailed comparison with effective mass calculations – showing the limitations of such methods – the physics of anti-crossing and hybridisation are explored and are shown to have significant effects on the charge density distributions and on optical spectra.

In chapter 5 we shall turn our attention to Si/Ge technology and shall introduce a method by which the effects of strain can be introduced into low dimensional structure calculations. A detailed exposition of the results of our method for Si, Ge and various alloys will be given for both hydrostatic and uniaxial pressure effects and comparisons made between our theoretical results and the results of hydrostatic pressure experiments, and between the results of a deformation potential calculation and our results for the uniaxial regime. The quality of the fits over a wide range of alloy

composition and pressures allows us a certain confidence in going on to model a couple of interesting real structures.

Chapter 6 investigates the bound states of a Si/Ge quantum well and shows how the realistic bandstructure of silicon can play an important role in the determination of these states. Also a $(Si)_4(Ge)_4$ superlattice, which has received much interest lately, is investigated theoretically.

CHAPTER TWO

THE COMPLEX BANDSTRUCTURE MATCHING TECHNIQUE

A THEORETICAL INVESTIGATION

In this chapter we shall give a detailed account of how the electronic states of general low dimensional structures can be investigated by means of a complex bandstructure matching technique (CBMT). Particular emphasis will be laid on the way in which complex bandstructure can be folded down onto a two dimensional representation. The method will be applied to both quantum wells and superlattices in some depth.

Complex Bandstructure.

The concept of complex bandstructure has been long known (Tamm, 1932), and well investigated as an abstract mathematical object of topological, as well as physical, interest (Heine, 1963). The physical basis is simple to understand: when the periodicity of a crystal is removed over a short range, by a defect or interface, the usual concept of Bloch functions which are periodic through all space is also removed. This lack of periodicity allows localised states to exist which can have energies which correspond to energies within the usual bulk-crystal bandgap.

At first sight the idea of states actually existing within the bandgap

seems contrary to one of the bases of solid state physics. To understand this paradox it is necessary to consider the form of these complex states. A general state with energy 'E' can be written as:

$$\phi_E = exp(i\mathbf{k.r})U_{\mathbf{k}}(\mathbf{r}).\qquad\qquad 2.1$$

where $U_{\mathbf{k}}$ is the usual periodic description of the underlying crystal structure, but where the wavevector can now take complex values. So from equation (2.1), in one dimension we can write

$$\phi_E(x + a) = exp(ika)\phi_E(x).\qquad\qquad 2.2$$

which means that the solution, for a wavevector with non-real k, will decay as it progresses through the crystal. In a bulk crystal it is necessary to impose the boundary conditions that the wavefunction should remain finite as we approach infinity. Therefore only the real and decaying solutions need be considered as physically meaningful, and the growing solutions can be discarded. We shall see later that this is **not** the case for low dimensional structures.

Various indirect methods have been employed to investigate the nature of these complex states and how they contribute to the overall bandstructure. Perhaps the most convincing were carried out in the 1960's by investigating the tunnelling current through a thin sample of semiconductor whilst varying the applied voltage in such a way that the impinging electrons had an energy corresponding to energies in the bandgap of the material under

investigation. One such experiment carried out on InAs (Parker and Mead, 1968) showed that the wavevector in a forbidden gap – at least for a small bandgap material – could be accurately calculated by a symmetrical two band expression of the form:

$$E = \left(\frac{E_g^2}{4} + \frac{h^2 k^2 E_g}{8\pi^2 m^*}\right)^{\frac{1}{2}} - \frac{E_g}{2}.$$

where E_g is the bandgap of the sample and other symbols have their usual meaning.

Generating Complex Bandstructure.

The experiment of Parker and Mead, which shows that the complex parts of a bandstructure can be modelled accurately by a simple model leads us to the conclusion that an accurate representation of the evanescent states of a material can be generated if the real, propagating, states are faithfully represented. Consequently it should be possible to produce 'realistic' complex bandstructure by any means which allows the calculation of ordinary bandstructure (such as tightbinding, k.p or pseudopotential methods). A description of the various processes required to produce complex bandstructure from these methods is available in the literature (Chung Chang and Schulman, 1984).

Choice of Method for Producing Bandstructure.

The method actually chosen for all the bandstructure production in the following work is a plane-wave basis, pseudopotential calculation. This important choice was made because of several demands imposed by the

proposed calculations. (a) It was important to have an accurate description of both the valence and conduction bands since both were to be investigated. Also both fits were required since they were needed for calculations of matrix elements between valence and conduction band states. (In this context 'accurate description' is taken to mean a fitting to experimental data which gives the main direct and indirect bandgaps accurately, as well as the effective masses of the main participating bands.) Pseudopotentials are particularly useful in this context since they allow a simple means of varying various physical parameters by altering the pseudopotential formfactors. (b) It was necessary to include the effects of spin and strain in a straightforward manner. This will be shown to be the case for pseudopotentials (Appendix A and Chapter 5 respectively). (c) A wealth of literature, including sets of pseudopotential formfactors, already exists and although they may not adequately describe the properties of the bandstructure which are of interest they can be used as a starting point.

Perhaps it is worth noting at this juncture a couple of drawbacks of the pseudopotential method. Most importantly a numerical problem exists because of the finite number of planewaves used as basis states. Since a 'complete' description necessitates an infinite number of plane-waves certain areas of the bandstructure may be considered not to have converged. In practice this can introduce errors at certain points such as the zone edge. The other main problem that pseudopotentials may introduce is due to the fact that we are not including atomic states. This may have an effect on
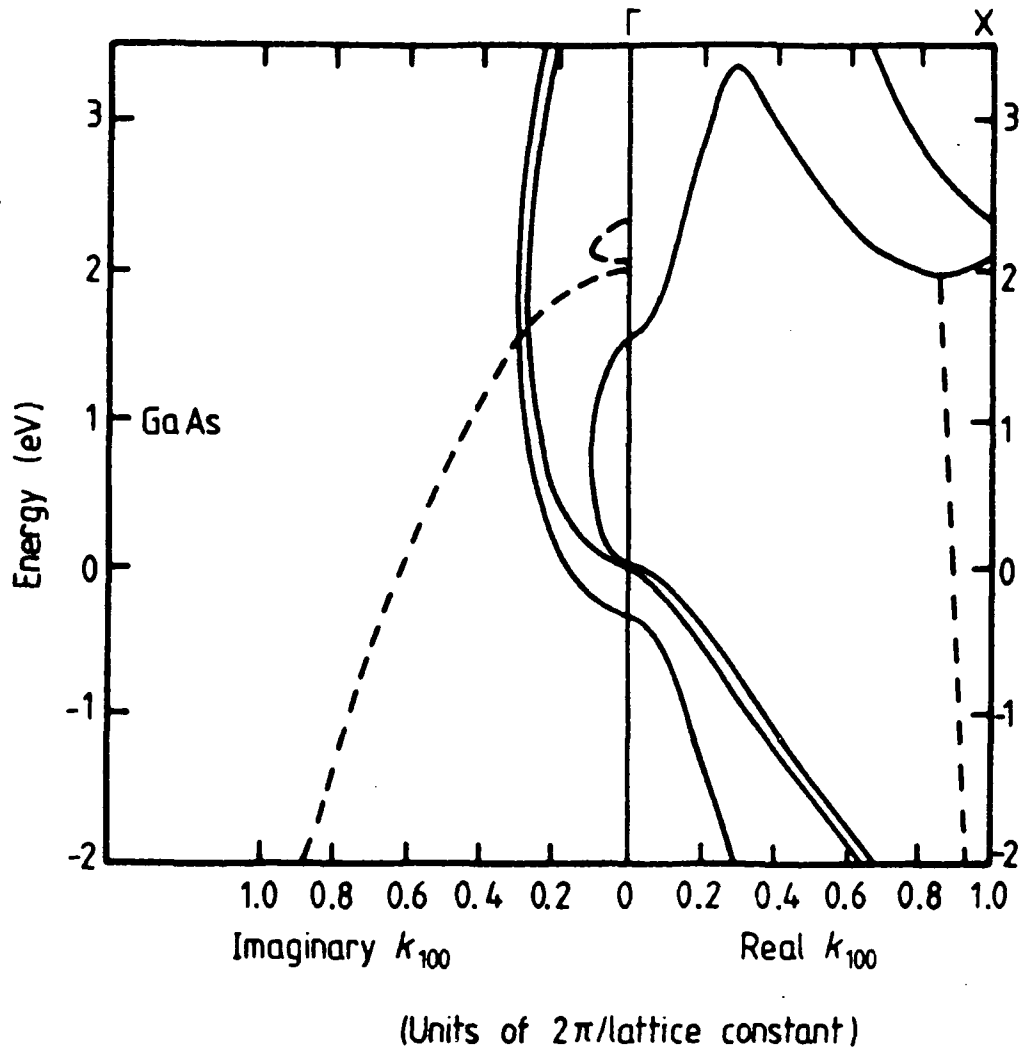
Figure (2.1) Part of the complex bandstructure for a
direct gap cubic material with spin included. Solid
lines indicate real and imaginary solutions, dotted
lines represent complex solutions.

calculations of matrix elements and wavefunctions and it will be important to bear this fact in mind when such calculations are carried out.

Complex Bandstructure: appearance and conventions.

It will be necessary later in this work to consider the complex bandstructure of various materials and so it may be helpful at this point to discuss the general appearance of complex bandstructure and the conventions which will be employed.

Figure (2.1) shows the complex bandstructure of a direct–gap cubic material with spin included. Real and purely imaginary solutions are represented by solid lines in the right and left portions of the diagram respectively. Complex solutions are shown by dotted lines in both sections such that the imaginary component is in the left section and the real component appears in the right. The complex solutions are at least eightfold degenerate (with spin) in the (100) direction for GaAs since if a state k exists so do the states $k^*, -k, -k^*$.

The Matching Technique.

Assuming that the bulk bandstructure has been calculated we wish to use the energy eigenfunctions obtained to solve low–dimensional problems. Our general approach, which will be explained in detail in this section will consist of setting up test energy eigenfunctions of the low–dimensional structure and calculating whether the state can exist as a solution to the appropriate Hamiltonian when the appropriate matching and boundary conditions have been imposed. By varying the energy of the test function

over a range of energies it is possible to find the physically realisable energy eigenfunctions of the structure.

To begin with we consider the two interface problem. Figure (2.2) shows a diagram of the setup which we wish to investigate. It is important to notice that figure (2.2) is completely general, this means that it may represent three different materials and either valence or conduction band offsets. It can be thought of as a building block from which we will be able to construct all other structures. For convenience – and to be consistent with the quantum well calculation – we define the outer regions to be barrier regions and the inner region to be the well region.

At the outset it is important to define a few terms; *in-plane* will mean perpendicular to the direction of growth of any structure. All structures will be assumed to be grown in the 'x' (100) direction. We shall assume that at a particular energy 'E' we know the values of k (complex, real and imaginary) and the eigenfunctions corresponding to these k's for the three materials (Appendix A). Each of the energy eigenfunctions can be written as:

$$\phi_E = \sum_{\mathbf{g}} a_{\mathbf{g}} e^{i(\mathbf{k}+\mathbf{g}) \cdot \mathbf{r}} \qquad\qquad 2.3$$

consistent with our planewave basis set. The sum is taken over all reciprocal lattice vectors and is also assumed to include a summation over spin variables to simplify notation. It is functions of this form that we shall use to build up our test wavefunctions at the particular energy 'E'. For region I we can
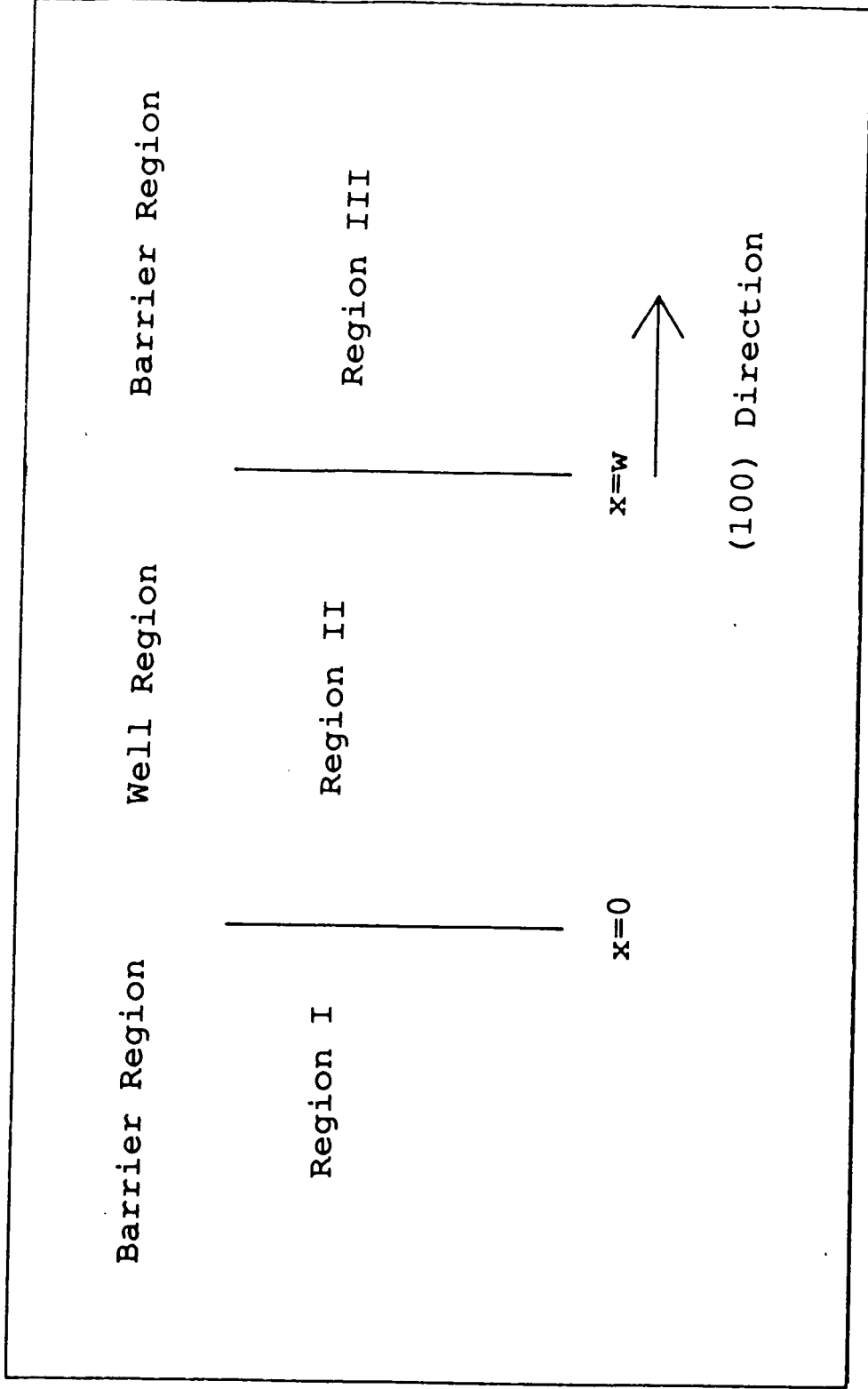
Figure (2.2)   Diagram for the two interface problem indicating the notation used in the text.

assume an overall wavefunction of the form:

$$\Phi_{B^I} = \sum_j B_j^I \phi_E.$$

This, when written explicitly gives:

$$\Phi_{B^I} = \sum_j B_j^I \sum_g a_g^{B_j^I} e^{i(k_j + g) \cdot r}. \qquad 2.4$$

Where we have expanded the test wavefunction in terms of the Bloch functions such that B_j^I is the coefficient of the Bloch function with wavevector k_j and $a_g^{B_j^I}$ is the Bloch expansion coefficient for the bulk eigenfunction with wavevector k_j. The sum over j, here and throughout the general theoretical formulation, will be assumed to be infinite – but consideration will be given as to the best method of truncation later. The 'zero of energy' of the calculation can, of course be chosen arbitrarily for one material but in the expansions for region II and III the zero of energy will be imposed in order to give the correct offsets.

Similarly for region II;

$$\Phi_W = \sum_{j'} W_{j'} \sum_{g'} a_{g'}^{W_{j'}} e^{i(k_{j'} + g') \cdot r} \qquad 2.5$$

with W_j representing the expansion coefficients for the well region. It is easy to see that the set of k_j's needs to include the growing solutions as well as the decaying and real solutions (if they exist). This is because the width of the well region is assumed to be small and so the growing solutions can be included without them 'blowing up' or becoming unphysical. This may also

12

be true for the barrier regions which may also be thin (in a superlattice for instance).

For region III we have:

$$\Phi_{B^{II}} = \sum_{j'} B_{j'}^{II} \sum_{g''} a_{g''}^{B_{j'}^{II}} e^{i(k_{j'}+g'')\cdot r}.$$

2.6

From elementary quantum mechanics, since the interface potentials are piecewise continuous, the wavefunctions and their derivatives must match at all points. Specifically, for this calculation, at $x = 0$ and $x = w$. At $x = 0$:

$$\Phi_{B^I}(x = 0) = \Phi_W(x = 0)$$

2.7

This, when written explicitly using equations (2.4) and (2.5) gives

$$\sum_{g} \sum_{j} B_j^I a_g^{B_j^I} e^{i(k_2+g_2)\cdot r_2} = \sum_{g'} \sum_{j'} W_{j'} a_{g'}^{W_{j'}} e^{i(k_2'+g_2')\cdot r_2}$$

2.8

where we have defined

$$g_2 = (g_y, g_z)$$

$$k_2 = (k_y, k_z)$$

$$r_2 = (y, z)$$

and for later use

$$k_j = (q_j, k_2)$$

But k_2 is a constant of the motion for this problem – equivalent to stating that the Hamiltonian is infinitely periodic in the y and z directions. Consequently the factor $e^{ik_2\cdot r_2}$ can be cancelled throughout. In fact

information about $\mathbf{k_2}$ is retained since the calculation of $\mathbf{k} = (k_x, \mathbf{k_2})$ at a particular energy is eqivalent to calculating k_x at a particular energy and $\mathbf{k_2}$. Equation (8) becomes

$$\sum_{\mathbf{g}} \sum_{j} B_j^I a_{\mathbf{g}}^{B_j^I} e^{i\mathbf{g_2} \cdot \mathbf{r_2}} = \sum_{\mathbf{g}'} \sum_{j'} W_{j'} a_{\mathbf{g}'}^{W_{j'}} e^{i\mathbf{g_2}' \cdot \mathbf{r_2}}. \qquad 2.9$$

Multiplying through by $e^{i(\mathbf{g}''' \cdot \mathbf{r_2})}$ and integrating over the interface, $x = 0$, gives

$$\sum_{\mathbf{g}} \sum_{j} B_j^I a_{\mathbf{g}}^{B_j^I} \delta_{\mathbf{g_2}, \mathbf{g_2}'''} = \sum_{\mathbf{g}'} \sum_{j'} W_{j'} a_{\mathbf{g}'}^{W_{j'}} \delta_{\mathbf{g_2}', \mathbf{g_2}'''} \qquad 2.10$$

But $\mathbf{g_2}'''$ is an arbitrary member of the set of two dimensional reciprocal lattice vectors, and since the sets of $\mathbf{g_2}$'s and $\mathbf{g_2}'$'s are identical (corresponding to the two dimensional projections of the zinc-blende or diamond reciprocal lattice vectors), we can write for all $\mathbf{g_2}$

$$\sum_{j} B_j^I P_{\mathbf{g_2}}^{B_j^I} = \sum_{j'} W_{j'} P_{\mathbf{g_2}'}^{W_{j'}} \qquad 2.11$$

where the

$$P_{\mathbf{g_2}} \equiv \sum_{\mathbf{g}'} a_{\mathbf{g}'} \delta_{\mathbf{g_2}', \mathbf{g_2}} \qquad 2.12$$

can be considered as a two dimensional projection of the $a_{\mathbf{g}}$'s. To clarify this we consider a definite example:.

$$P_{(0,0)}^j = a_{(0,0,0)}^j + a_{(2,0,0)}^j + a_{(\bar{2},0,0)}^j + a_{(4,0,0)}^j + \dots$$

It is worth considering what the physical meaning of the steps which take us from equations (2.8) to (2.12) is. The introduction of $\mathbf{g_2}'''$ is actually a mathematical indication that the wavefunction has been matched at all

14

points in the $x = 0$ plane. In the simpler effective mass models (Schiff, 1949) this would still be the case but all points in the $x = 0$ plane would be considered as equivalent – i.e. the crystal structure in the y and z directions would be ignored.

Next we employ the matching condition:

$$\frac{\partial \Phi_{B^I}}{\partial x}(x = 0) = \frac{\partial \Phi_W}{\partial x}(x = 0) \qquad 2.13$$

It is important to note that this expression does not include the effective masses as part of the matching condition. The effective masses can be considered to be included implicitly in the periodic parts of the Bloch functions. (In fact part of the strength of this method lies in the fact that non-parabolicity and hence varying effective masses are included easily).

Using equations (2.13), (2.4) and (2.5) we obtain, after some simplification and cancellation:

$$\sum_{g}\sum_{j} B_j^I a_g^{B_j^I}(q_j + g_x)\delta_{g_2,g_2'''} = \sum_{g'}\sum_{j'} W_{j'} a_{g'}^{W_{j'}}(q_{j'} + g_x')\delta_{g_2',g_2'''} \qquad 2.14$$

giving for all g_2:

$$\sum_{j} B_j^I Q_{g_2}^{B_j^I} = \sum_{j'} W_{j'} Q_{g_2}^{W_{j'}} \qquad 2.15$$

where

$$Q_{g_2} \equiv \sum_{g'} a_{g'}(q_j + g_x)\delta_{g_2',g_2} \qquad 2.16$$

It is now necessary to consider the equivalent equations at $x = w$. We begin with

$$\Phi_{B^{II}}(x = w) = \Phi_W(x = w) \qquad 2.17$$

15

We can, without loss of generality, take the 'origin' for the bandstructure of the second barrier to be at $x = w$. This simplifies the mathematical manipulation involved and also allows the method to be directly used for strained materials in which the lattice constants in the growth direction will be different. It is, however, the nature of strained low dimensional structures that the in-plane lattice constant must be the same for both materials.

Employing the same procedure as discussed above the matching condition becomes for any reciprocal lattice vector of the crystal 'g''''

$$\sum_{j'} \sum_{g''} B_{j'}^{II} a_{g''}^{B_{j'}^{II}} exp(i(g'' + q_{j''})\delta)\delta_{g_2'',g_2'''} = \sum_{j'} W_{j'} exp(iq_{j'}w) \sum_{g'} a_{g'}^{W_{j'}} e^{ig_x'w}\delta_{g_2',g_2'''} \qquad 2.18$$

Where $exp(i(g'' + q_{j''})\delta)$ is a phase factor which displaces the origin at which the bandstructure is calculated for non-integer values of well width.

To simplify this expression further it is necessary to consider the nature of the reciprocal lattice vectors for zinc-blende and diamond structures. All the reciprocal lattice vectors of these materials will have totally odd components such as $(1,1,-1)$, $(3,1,5)$ *etc* or totally even $(0,0,0)$, $(4,2,0)$ etc. This means that $e^{ig_x w} = 1$ if w is an even number of monolayers or if g_x is even and $e^{ig_x w} = -1$ if we have an odd number of monolayers and g_x is odd. We get, therefore, for all g_2 :

$$\sum_{j'} B_{j'}^{II} P_{g_2}^{B_{j'}^{II}} exp(iq_{j'}w) = \sum_{j'} W_{j'} P_{g_2}^{W_{j'}} exp(iq_{j'}w) \qquad 2.19$$

Where the P's have been defined in equation (2.12). For simplification it is useful to make the substitution

$$B_{j'}^{II} e^{iq_{j''}w} \to B_{j'}^{II} \qquad 2.20$$

16
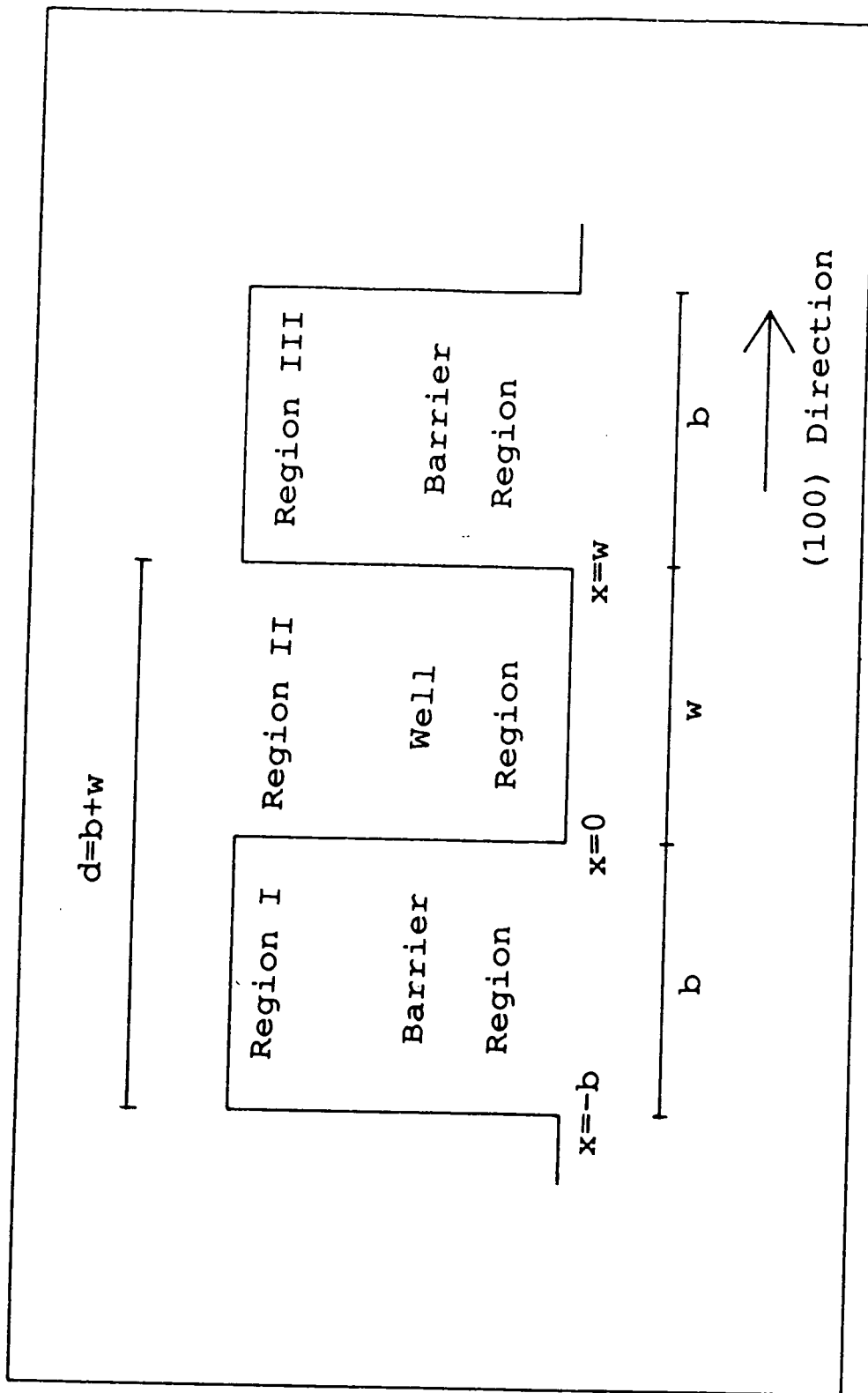
Figure (2.3) Schematic diagram of a superlattice indicating the notation used in the text.

to give

$$\sum_{j'} B_{j'}^{II} P_{g_2''}^{B_{j'}^{II}} = \sum_{j'} W_{j'} P_{g_2}^{W_{j'}} exp(iq_{j'}w)$$ 2.21.

This leaves the last matching condition:

$$\frac{\partial \Phi_{B^I}}{\partial x}(x = w) = \frac{\partial \Phi_W}{\partial x}(x = w)$$ 2.22

which using the above methods gives, for all g_2 :

$$\sum_{j'} B_{j'}^{II} Q_{g_2''}^{B_{j'}^{II}} = \sum_{j'} W_{j'} Q_{g_2}^{W_{j'}} exp(iq_{j'}w)$$ 2.23

The four equations (2.11), (2.15), (2.21) and (2.23) contain a full description of the matching conditions for the two–interface problem. To proceed with the investigation it is necessary to consider specific cases. We begin with a superlattice.

Energy States of a Superlattice.

Figure (2.3) shows a schematic diagram of a superlattice. It is similar to figure (2.2) except that we now have a definite, assumed small, dimension for the barrier region. It will be assumed for the superlattice that region III consists of the same material as region I.

Since the superlattice has infinite periodicity in the (100) direction there must be a 'superlattice Bloch condition' which describes the superlattice wavefunction and is of the form

$$\Phi_{B^I}(-b) = \Phi_{B^{II}}(w)e^{-iK_{sl}d}$$ 2.24

where K_{sl} is the superlattice wavevector at the energy E. Equation (2.24)

can be written for all $\mathbf{g_2}$:

$$\sum_j B_j^I P_{\mathbf{g_2}}^{B_j^I} e^{-ig_x b} exp(-iq_j b) = e^{-iK_s d} \sum_{j'} B_{j'}^{II} P_{\mathbf{g_2}}^{B_{j'}^{II}} e^{ig_x \delta} \qquad 2.25$$

with δ defined as for equation (2.18) or

$$\sum_j B_j^I P_{\mathbf{g_2}}^{B_j^I} exp(-iq_j b) = e^{-iK_s d} \sum_{j'} B_{j'}^{II} P_{\mathbf{g_2''}}^{B_{j'}^{II}} e^{ig_x d} \qquad 2.26$$

(where we have again used the fact that $\mathbf{g}$ is even or odd). The superlattice Bloch condition also necessitates:

$$\frac{\partial \Phi_{B^I}}{\partial x}(x = -b) = e^{-iK_s d} \frac{\partial \Phi_{B^{II}}}{\partial x}(x = w) \qquad 2.27$$

which can, for all $\mathbf{g_2}$, be shown to reduce to,

$$\sum_j B_j^I Q_{\mathbf{g_2}}^{B_j^I} exp(-iq_j b) = e^{-iK_s d} \sum_{j'} B_{j'}^{II} Q_{\mathbf{g_2}}^{B_{j'}^{II}} e^{ig_x d}. \qquad 2.28$$

The equations (2.11), (2.15), (2.21), (2.23), (2.26) and (2.28) define the superlattice problem completely. It is now necessary to consider how they can be solved numerically.

Mathematical Formulation for Superlattice.

Inspection of equations (2.11) and (2.15) allows us to write a matrix equation:

$$\mathbf{M_W W} = \mathbf{M_{B^I} B^I} \qquad 2.29$$

where $\mathbf{W}$ and $\mathbf{B^I}$ are column vectors containing the expansion coefficients $W_1, W_2...$ and $B^I_1, B^I_2, ...$ respectively. $\mathbf{M_W}$ and $\mathbf{M_{B^I}}$ are square matrices;

18

written explicitly

$$
\mathbf{M_W} =
\begin{pmatrix}
P_{00}^{j'=1} & P_{00}^{j'=2} & \cdot & \cdot & \cdot & \cdot & \cdot & \cdot \\
P_{11}^{j'=1} & \cdot & \cdot & \cdot & \cdot & \cdot & \cdot & \cdot \\
\cdot & \cdot & \cdot & \cdot & \cdot & \cdot & \cdot & \cdot \\
Q_{00}^{j'=1} & Q_{00}^{j'=2} & \cdot & \cdot & \cdot & \cdot & \cdot & \cdot \\
Q_{11}^{j'=1} & \cdot & \cdot & \cdot & \cdot & \cdot & \cdot & \cdot \\
\cdot & \cdot & \cdot & \cdot & \cdot & \cdot & \cdot & \cdot \\
\cdot & \cdot & \cdot & \cdot & \cdot & \cdot & \cdot & \cdot
\end{pmatrix}
\qquad 2.30
$$

where all the elements of the matrix are calculated for the well region. A similar representation holds for the matrix $\mathbf{M_{B^I}}$. With similar notation equations (2.21) and (2.23) can be written as:

$$
\mathbf{M_W D_W W} = \mathbf{M_{B^I} B^{II}} \qquad 2.31
$$

where $\mathbf{D_W}$ is the diagonal matrix such that

$$
\mathbf{D_W} =
\begin{pmatrix}
e^{iq_1 w} & 0 & \cdots & \cdots \\
0 & e^{iq_2 w} & \cdots & \cdots \\
\cdots & \cdots & \ddots & \cdots \\
\cdots & \cdots & \cdots & e^{iq_n w}
\end{pmatrix}
= diag\{e^{iq_1 w}, e^{iq_2 w}, \ldots, e^{iq_n w}\} \qquad 2.32
$$

Equations (2.26) and (2.28) can similarly be transformed into matrix representation as

$$
\mathbf{M_{B^I} D_B B^I} = e^{-iK_{s^I d}} \mathbf{D_g M_{B^{II}} B^{II}} \qquad 2.33
$$

Where $\mathbf{D_g}$ is diagonal and of the form

$$
\mathbf{D_g} = \begin{pmatrix} \Lambda_1 & 0 \\ 0 & \Lambda_1 \end{pmatrix}
$$

with,

$$
\Lambda_1 = diag\{e^{ig_n d}\}
$$

such that g_n is the value of g_x for the nth reciprocal lattice vector. It is worth noting that if the period of the superlattice is an integral number of

Region I   Region II   Region III

Barrier Region   Well Region   Barrier Region

Only solutions   All Solutions   Only Solutions
Decaying To The   Included.   Decaying To The
Left.   Right.

                          x=0   x=a

                          (100) Direction
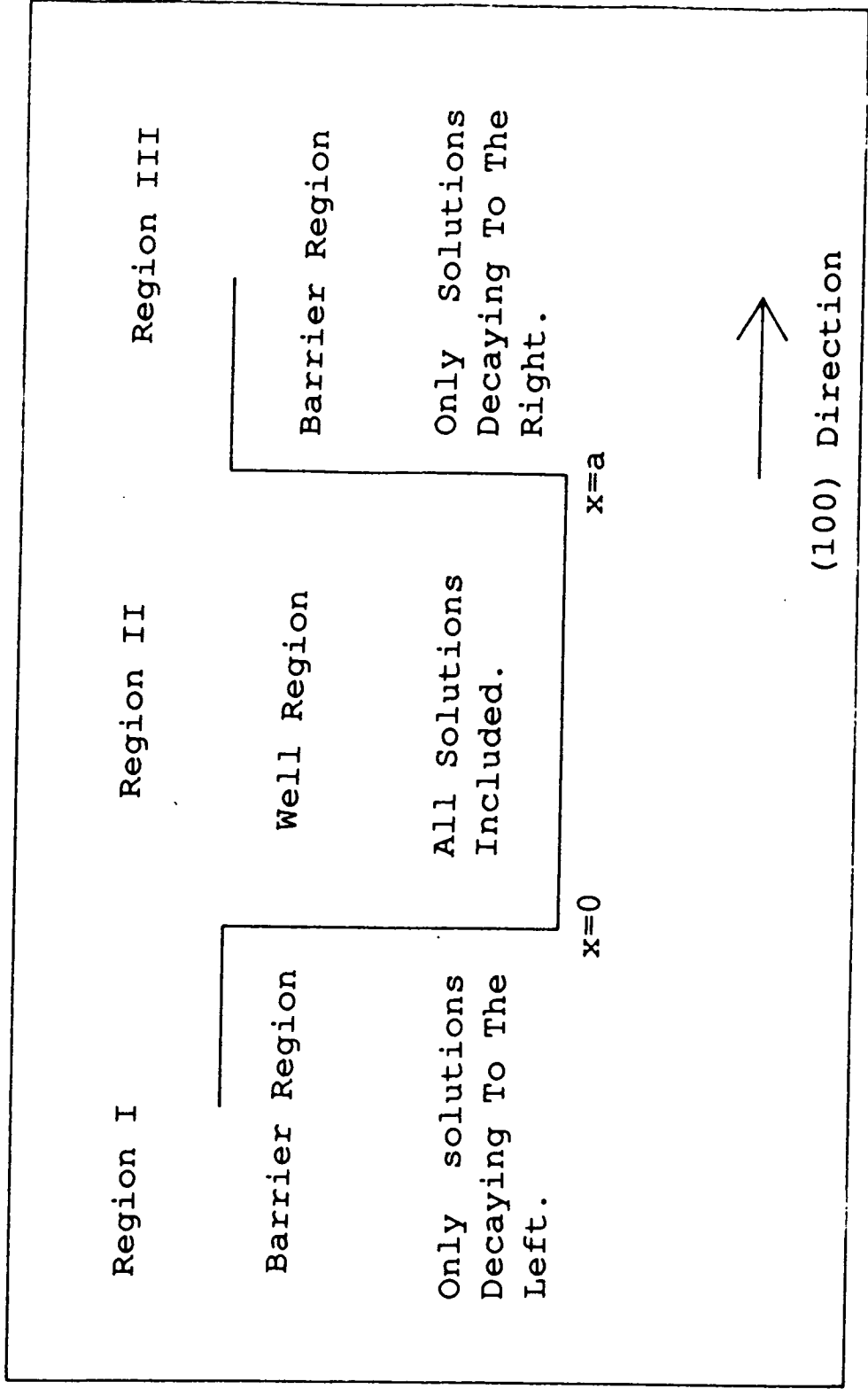
Figure (2.4) Diagram of quantum well indicating
notation used in the text.

unit cells then the matrix $\mathbf{D_g}$ is an identity matrix and does not contribute to the calculation.

It is now an elementary matter to combine equations (2.33), (2.31) and (2.29) to give:

$$\mathbf{M_{B^{II}}^{-1}D_g^{-1}M_{B'}D_BM_{B'}^{-1}M_WD_W^{-1}M_W^{-1}M_{B^{II}}B^{II}} = e^{-iK_sd}\mathbf{B^{II}} \qquad 2.34$$

This equation can be considered to represent an eigenvalue problem with eigenvectors $\mathbf{B^{II}}$. This involves finding the eigenvalues of the matrix $\mathbf{S}$

$$\mathbf{S = M_{B^{II}}^{-1}D_g^{-1}M_{B'}D_BM_{B'}^{-1}M_WD_W^{-1}M_W^{-1}M_{B^{II}}}$$

and if any of the eigenvalues have a magnitude of 1 we have found a solution at the energy E with a superlattice wavevector e^{-iK_sd}. (We note in passing that the matrix $\mathbf{S}$ has a determinant of 1). Alternatively one may select a superlattice wavevector 'Q', say, and study the behavior of

$$determinant\{\mathbf{S} - e^{-iQd}\}$$

as we vary the energy E. This will be zero for energies at which the matching equations have a solution for superlattice wavevector equal to Q. In practice it is actually a matter of calculating the determinant over a range of energies and observing when it changes sign or has a minimum.

Mathematical Formulation for Quantum Well.

The formulation of the quantum well problem, although starting with the same matching conditions as the superlattice, requires a rather

different formulation. The central, well–region still contains real, imaginary and complex solutions but the boundary conditions in regions I and III – as defined by figure (2.4) – must be that the wavefunction goes to zero at infinity. Expressed mathematically these boundary conditions become:

$$\lim_{x \to -\infty} \Phi_{B^I}(x) = 0$$

and

$$\lim_{x \to \infty} \Phi_{B^{II}}(x) = 0$$

and in the following work it will be assumed that the wavefunction in regions I and III are composed only of complex and imaginary solutions – i.e. we only deal with bound solutions. For the boundary conditions to be satisfied only values of wavevector q must be included such that

$$\Im mag(q) \geq 0, x > a$$

$$\Im mag(q) \leq 0, x < 0$$

These conditions mean that half of the expansion coefficients in equations (2.11) and (2.21) must be set to zero. When these two equations are combined we arrive at

$$\mathbf{P_B B} = \mathbf{P_w W} \qquad\qquad 2.35$$

Where $\mathbf{P_w}$ and $\mathbf{W}$ have been defined above, $\mathbf{B}$ is a column vector comprising elements from regions I and III.

$$\mathbf{B} = \begin{pmatrix} B_1^I \\ B_2^I \\ \vdots \\ B_1^{II} \\ \vdots \end{pmatrix}$$

21

$\mathbf{P_B}$ also contains information on both barrier and well regions.

$$\mathbf{P_B} = \begin{pmatrix} \mathbf{P_{B^I}} & \mathbf{0} \\ \mathbf{0} & \mathbf{P_{B^{II}}} \end{pmatrix}$$

where $\mathbf{P_{B^I}}, \mathbf{P_{B^{II}}}$ and $\mathbf{0}$ are square matrices and $\mathbf{P_{B^I}}$ is defined as

$$\mathbf{P_{B^I}} = \begin{pmatrix} P_{00}^{j'=1} & P_{00}^{j'=2} & \cdots & P_{00}^{j'=n} \\ P_{11}^{j'=1} & \cdots & \cdots & \cdots \\ \vdots & \vdots & \vdots & \vdots \end{pmatrix}$$

where all the matrix elements have been defined for region I. There is of course an analogous definition for $P_{B^{II}}$

$$\mathbf{P_W} = \begin{pmatrix} \hat{\mathbf{P}}_W \\ \mathbf{D_W} \hat{\mathbf{P}}_W \end{pmatrix}$$

where $\hat{\mathbf{P}}_W$ is a rectangular matrix defined in a similar manner to $\mathbf{P_{B^I}}$ and $\mathbf{P_{B^{II}}}$. $\mathbf{D_W}$ is a square matrix of the form

$$diag\{exp(iq_1 a), exp(iq_2 a), exp(iq_3 a).......\}.$$

A combination of equations (2.15) and (2.23) give an equation relating the derivatives of the wavefunction in a similar form:

$$\mathbf{Q_B B} = \mathbf{Q_W W} \qquad\qquad 2.36$$

So if an energy solution exists within the quantum well – i.e. if all matching conditions can be satisfied – equations (2.35) and (2.36) will give

$$(\mathbf{P_W^{-1} P_B Q_B^{-1} Q_W} - \mathbf{I})\mathbf{W} = 0 \qquad\qquad 2.37$$

or equivalently

$$determinant\{\mathbf{P_W^{-1} P_B Q_B^{-1} Q_W} - \mathbf{I}\} = 0. \qquad\qquad 2.38$$

To find the energies at which this expression can be satisfied the procedure described in the previous section can be employed: by scanning through a range of energies with a subsequent investigation of the behavior of the determinant.

Truncation of States.

Until now it has been assumed that the summation over wavevectors ($\sum_j$ *etc*) has included an infinite number of k's and the summation over reciprocal lattice vectors ($\sum_g$ *etc*) has been over all g's (also an infinite set). While this approach is valid from a purely theoretical viewpoint it is necessary to consider how these summations can be truncated to make them solvable by computational means. The most straightforward consideration is the truncation of the set of reciprocal lattice vectors. This is a well understood procedure (Cohen and Heine, 1970) where, by using a finite set of reciprocal lattice vectors, a good description of the bulk bandstructures can still be obtained. Assuming we have N reciprocal lattice vectors (N=27, 65, 89, 113 *etc.*) these can be projected down to N_2 g_2's. For example with N=27, N_2=13 consisting

of $g_2 = \{(0,0),(1,1),(1,-1),(-1,1),(-1,-1),(0,2),(2,0),(0,-2),(-2,0),$

$(2,2),(-2,2),(2,-2),(-2,-2)\}.$

The method used for calculating the wavevectors gives 2N wavevectors at a particular energy (Appendix A). For the superlattice we take $2N_2$ of these solutions ($2N_2<2N$) in each of the three regions. This means we have $6N_2$ unknowns corresponding to the W_j, B_j^I and $B_{j'}^{II}$'s. But we have N_2 equations for each of the six matching conditions given by equations (2.11),

(2.15), (2.21), (2.23), (2.26) and (2.28). Therefore we have 6N$_2$ equations and 6N$_2$ unknowns and so the problem is well defined and is compatible with the 'square matrix' analysis used above. In the quantum well, on the other hand, we only have 4N$_2$ matching equations but now only have 4N$_2$ unknowns (N$_2$ in each of the barriers and 2N$_2$ in the well region) and so this problem is equally well defined.

Extraction of Wavefunction.

In the previous sections we have shown how it is possible, by fairly simple means, to calculate energy levels of quantum wells and bandstructure of superlattices. Once a solution has been found at a particular energy it is likely that some other physical properties, such as matrix elements, will be required. The first step towards calculating any matrix element is to have a mathematical representation of the wavefunction in the various regions. To do this it is a simple matter to return to equations (2.34) and (2.37) to obtain the eigenvectors of these equations which give the expansion coefficients of the wavefunctions as expressed in equations (2.4), (2.5) and (2.6) at a particular energy.

If we write the wavefunction in the form

$$\Phi = \sum_{j} \sum_{g} a_g A_j e^{i(k_j + g) \cdot r} \qquad 2.39$$

where the $A_j (= B_j$ or $W_j)$ have been calculated as stated above. It is often interesting to consider how the charge density of a particular state appears when averaged over the y-z plane, rather than, say, a plot along the (100)

direction for a fixed r_2. Here, for completeness, we give an expression for the charge density averaged over a plane.

$$|\widetilde{\Phi(x)}|^2 = \int_y \int_z \sum_j \sum_{j'} \sum_g \sum_{g'} a_g^j a_{g'}^{j'*} A_j A_{j'}^* \exp(i(\mathbf{k}_j - \mathbf{k}_{j'}^* + \mathbf{g} - \mathbf{g}')\mathbf{r}) dz dy \quad 2.40$$

which after some simplification becomes

$$|\widetilde{\Phi(x)}|^2 = \sum_j \sum_{j'} \sum_g \sum_{g'} a_g^j a_{g'}^{j'*} A_j A_{j'}^* \exp(i(q_j - q_{j'}^* + g_x - g'_x)x)\delta_{g_2,g'_2} \quad 2.41$$

Further consideration of such averages and how they relate to matrix elements will be given in appendix D.

Extension of Theory to Other Structures.

Two particular cases, the superlattice and the quantum well, have been shown to be analysable by means of a CBMT. But the equations (2.11), (2.15), (2.21) and (2.23) which describe the general quantum mechanical matching conditions must be generally true for all structures. Consequently using these equations and the appropriate boundary conditions (corresponding to superlattice periodicity and wavefunctions vanishing at infinity for the two cases considered) it is possible to extend the method to any general 'two-dimensional' structure. The method for more complicated cases, such as multiple quantum wells or graded superlattices although being more involved require a treatment very similar to that given above. The formulation of more complicated problems has been treated by means of a complex bandstructure transmission matrix (Marsh and Inkson, 1986) and a scattering matrix (Ko and Inkson, 1988).

Similarly we can consider transmission and reflection through a quantum barrier by relaxing the condition that we have no propagating solutions in the 'barrier regions' *i.e.* travelling solutions in all regions or just in the outer regions allowing tunnelling to be investigated (Monaghan and Brand, 1988).

Summary.

This chapter has given a theoretical exposition of the CBMT and its application to various real structures. Some of the computational techniques necessary to carry out these calculations will be given in Appendix E. It will be useful, however, at this point, to mention some of the practicalities of such calculations. The main components of any calculation will be the wavevectors and the two-dimensional projections of the bandstructure (the P's and Q's) of the constituent materials. It is important to notice that these factors are totally independent of the details of the structure to be investigated. Details such as the widths of barriers and wells are only introduced when the matching equations are set up. This means that data, over a range of energies, need only be calculated once per material and stored. This allows a rapid investigation of width related effects as compared to, say, a supercell calculation.

Perhaps more importantly the calculation includes a full description of the bandstructure of the constituent materials without resorting to approximations (as for an envelope function approximation). Consequently it is possible to investigate direct and indirect materials in a similar manner

whilst retaining any effects due to non-parabolicity of a constituent material's bandstructure and any effects due to symmetry. In the next two chapters we shall show how these considerations allow detailed and accurate investigations to be made of III-V low dimensional structures.

CHAPTER THREE

THE BANDSTRUCTURE OF GaAs/AlAs SUPERLATTICES

In the previous chapter a general, in the sense of being material independent, discussion was given of a method of determining energy states and wavefunctions for superlattices and quantum wells. In this chapter we shall apply the method to a particular real physical system and compare the results with various other theoretical techniques and experimental results.

The physical system which we shall consider will be a set of AlAs/GaAs superlattices. This choice is a particularly good one for investigation and comparison for the following reasons: a) there are extensive results in the literature for this particular kind of superlattice using various theoretical techniques. b) The materials are very nearly lattice matched: with a lattice constant of 5.65Å for the GaAs compared with 5.66Å for AlAs and so we avoid the complication of including strain in the calculation (Chapter 5). c) These may be expected to exhibit interesting properties when forming a superlattice since AlAs is indirect and GaAs is direct. A more general investigation including both GaAs/AlAs and alloy stuctures will be carried out in chapter 4 for quantum wells.

Since the complex bandstructure matching technique requires the

states (real and evanescent) of the bulk materials to be accurately represented in order that the calculation gives a realistic description of low dimensional states it is necessary to begin by considering the nature of the bulk bandstructure of the two materials. In the work that follows in this chapter we shall use pseudopotential parameters taken from the literature (Gell et al, 1986). A description of the nature and quality of the fit is given in the reference but the results are rather confusing since spin is not included in the determination of the bandgaps. Consequently we shall give here a more consistent account of the bandgaps of the two materials using the parameters in appendix B. We shall compare the results of a pseudopotential calculation with that of bandgaps obtained from experiment. Since the theoretical and experimental results of others for the superlattices will cover a large temperature range the experimental 'bulk results' that we consider will all be appropriate to an 'average temperature' of approximately 100K.

Bandgaps of GaAs.

	Calculated	Experiment
$\Gamma - \Gamma$	1.42	$1.51^{(a)}$
$\Gamma - X$	1.90	$1.98^{(b)}$
$\Gamma - L$	1.74	$1.81^{(b)}$
SSO	0.334	$0.33^{(c)}$
$X_c - X_c$	0.30	$0.40^{(d)}$
$X_v - X_v$	0.07	$0.07^{(d)}$

(a) Sturge, 1962.

(b) Aspnes et al., 1976.
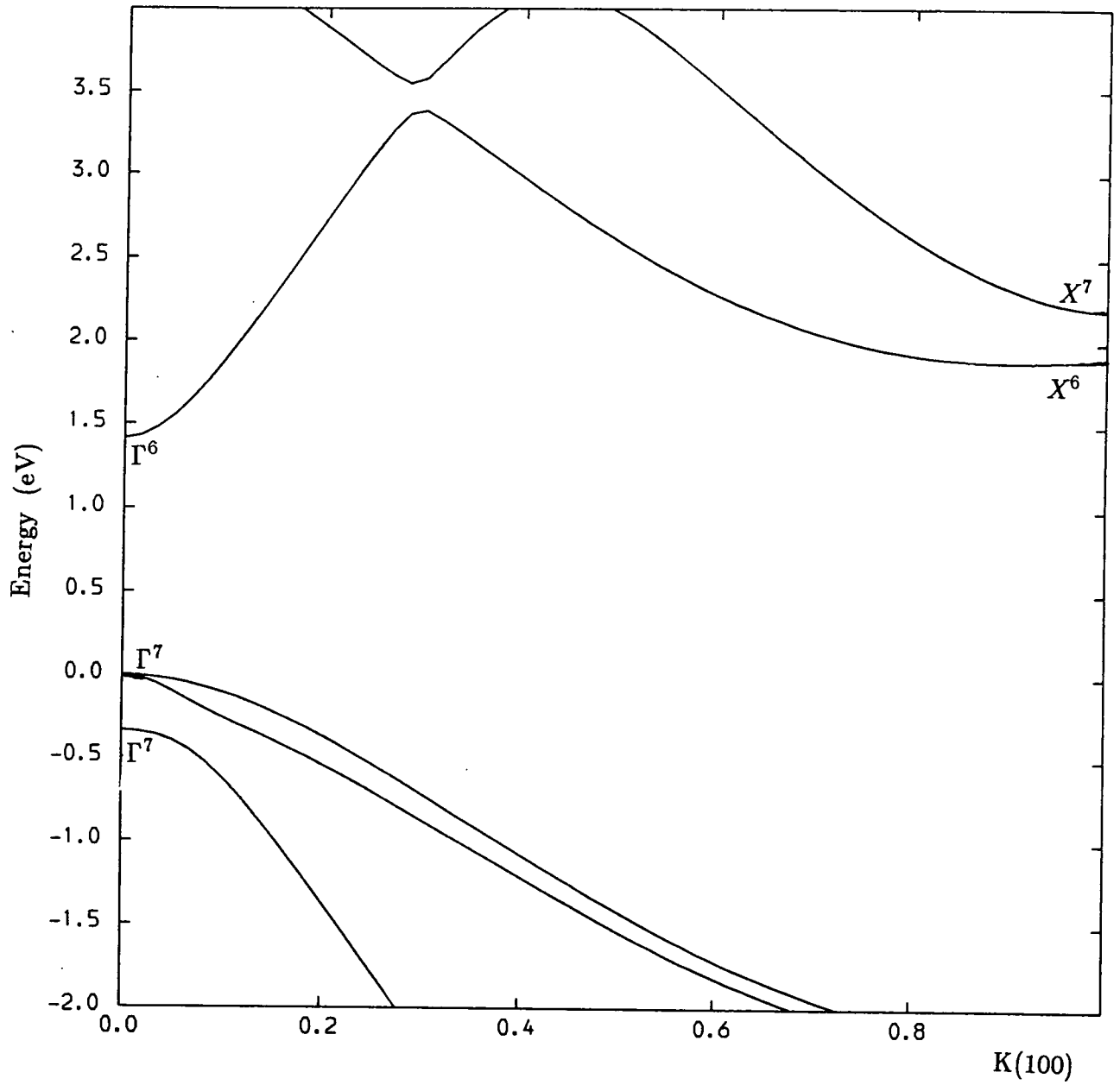
Figure (3.1) Bulk bandstructure of GaAs using the pseudopotential form factors given in appendix B.
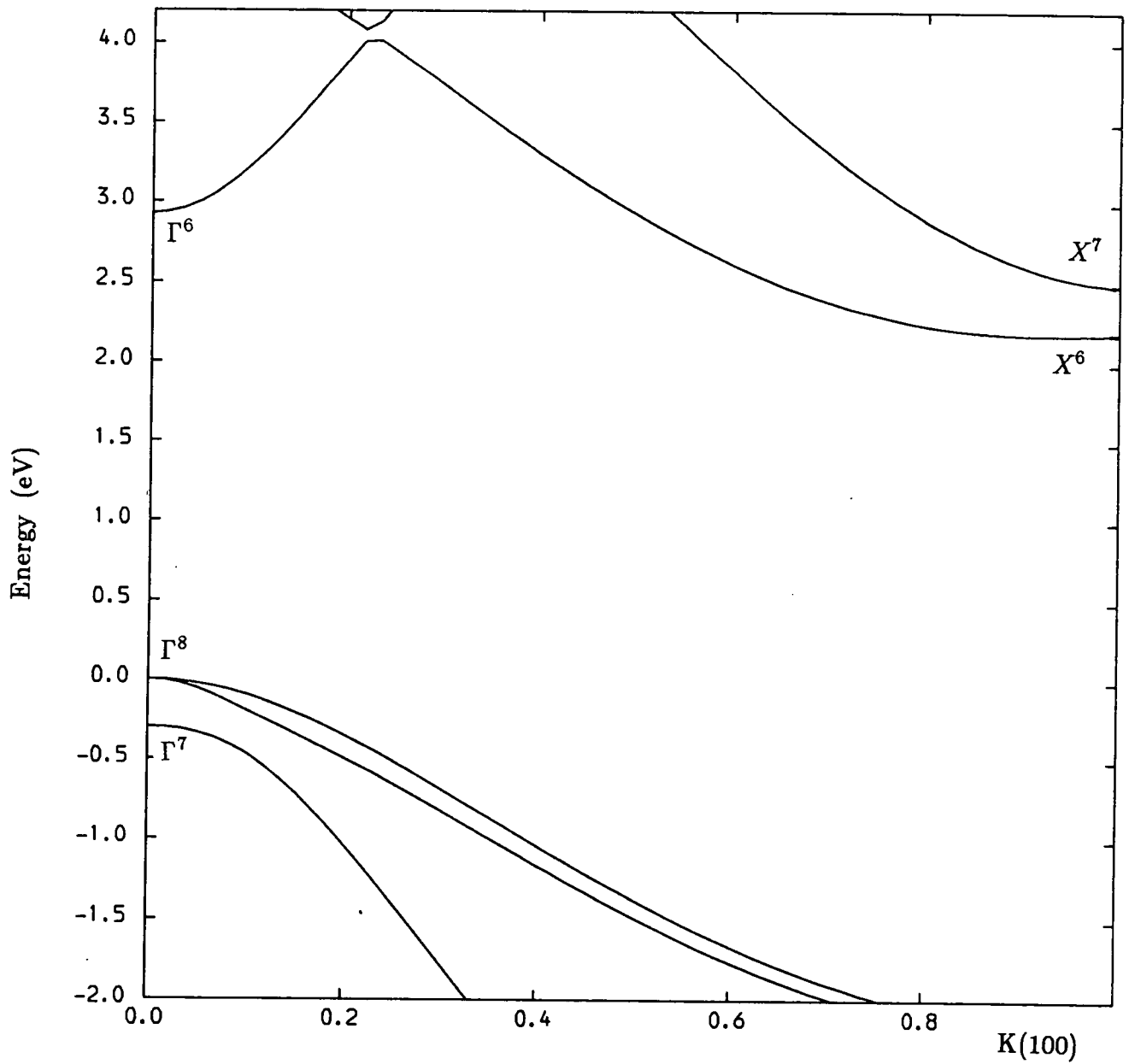
Figure (3.2) Bulk bandstructure of AlAs using the pseudopotential form factors given in appendix B.

(c) Braunstein R. and Kane E.O., 1962.

(d) Aspnes and Studna, 1973.

Bandgaps of AlAs.

	Calculated	Experiment
$\Gamma - \Gamma$	2.92	3.03[a]
$\Gamma - X$	2.18	2.22[a]
SSO	0.29	0.28[b]
$X_c - X_c$	0.30	0.20[c]

(a) Monemar, 1973.

(b) Onton, 1970.

(c) Dumke et al., 1972.

The overall results for both GaAs and AlAs can be seen to be fairly good with the largest error being about 0.15eV for the zone edge spin splittings. In particular the major direct and indirect bandgaps are all accurate to better than 10% or an absolute error of less than 0.1eV.

Using the same parameters we have calculated the bandstructures for GaAs (figure 3.1) and AlAs (figure 3.2) in the (100) direction and included some of their more important symmetry designations.

Superlattice Calculations.

Once we have obtained the bulk bandstructures it is necessary to consider how the materials should be brought together to form a low dimensional structure – in this case a superlattice – or specifically what conduction and valence band offsets should be used for AlAs/GaAs systems? Although a certain amount of uncertainty remains concerning offsets, a
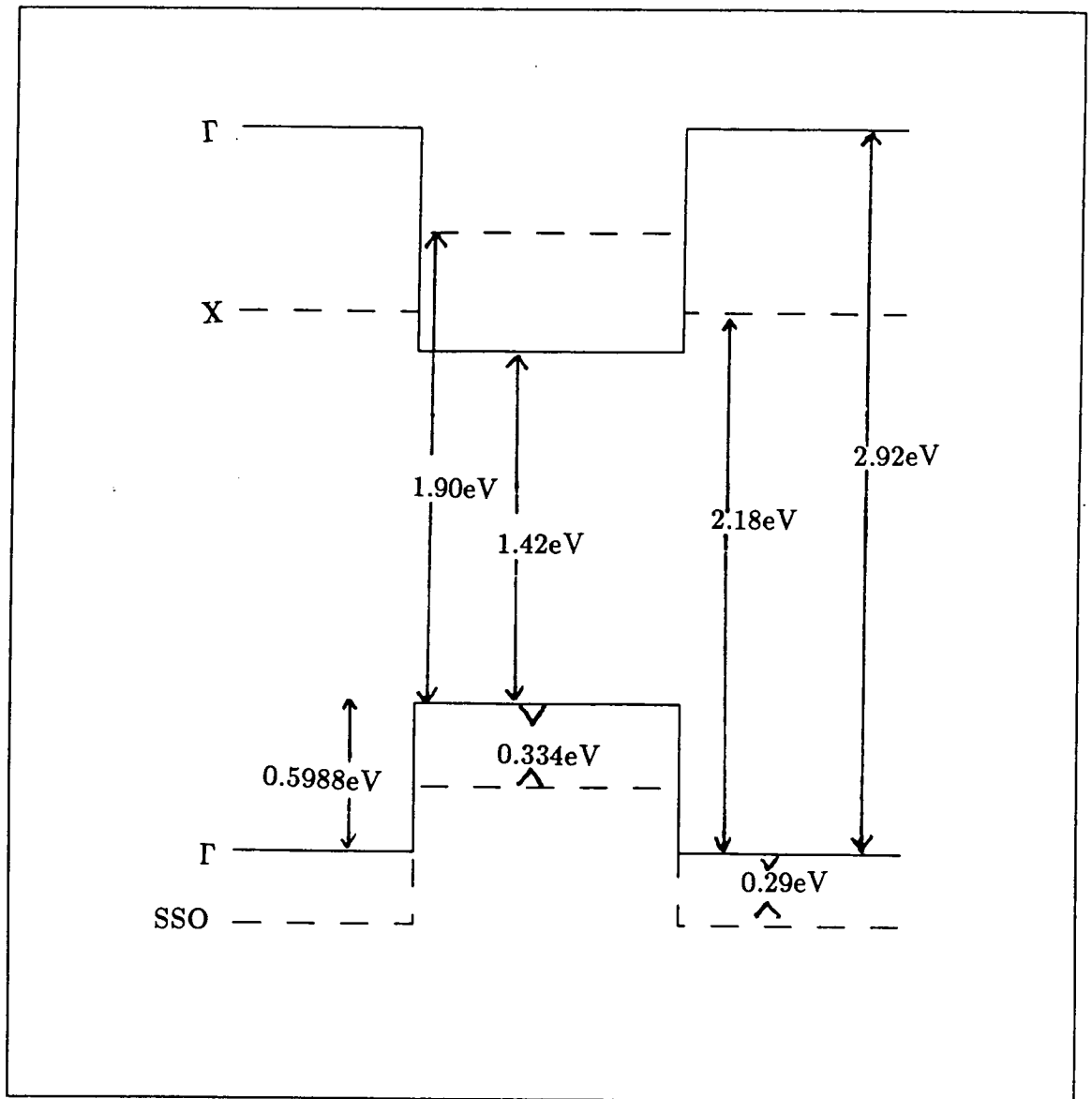
Figure (3.3) Diagram of valence and conduction band offsets used in this chapter. The solid line indicates Γ like offsets and the dotted lines indicates the X-like states in the conduction band and the spin-split-off states in the valence band.

generally accepted method of calculating offsets for $Al_{1-x}Ga_xAs$ on GaAs is to take the valence band offset to be $0.55x$ eV (Batey and Wright, 1985). This is the value which will be used in the next chapter but in order to make the best comparison with the work of Gell et al we have taken a valence band offset of 0.5988eV. This information combined with the knowledge of the bandgaps of the two materials allows us to obtain the offsets shown in figure (3.3). It is important to notice that in the conduction band the X-like electrons experience an AlAs well whereas the Γ-like electrons experience a GaAs like well. This will be seen to have interesting consequences for the low dimensional states which are considered later.

We now have all the information required to carry out a calculation on a superlattice. The first calculation carried out using our bandstructure matching technique (Brand et al, 1987) did not use the parameters given in appendix B and dealt with alloy superlattices. Nevertheless the calculation allowed a comparison with a simple effective mass theory in the valence band for a wide range of superlattice widths. The calculation showed that whereas the effective mass theory gave a fair description of many superlattice states it failed in two regions:

(a)   It could not describe the effects of non-parabolicity for the bulk states, which may have large effects in the valence band.

(b)   The effective mass theory could not predict the effects of symmetry. In particular at points of anti-crossing the effective mass theory would indicate crossing.
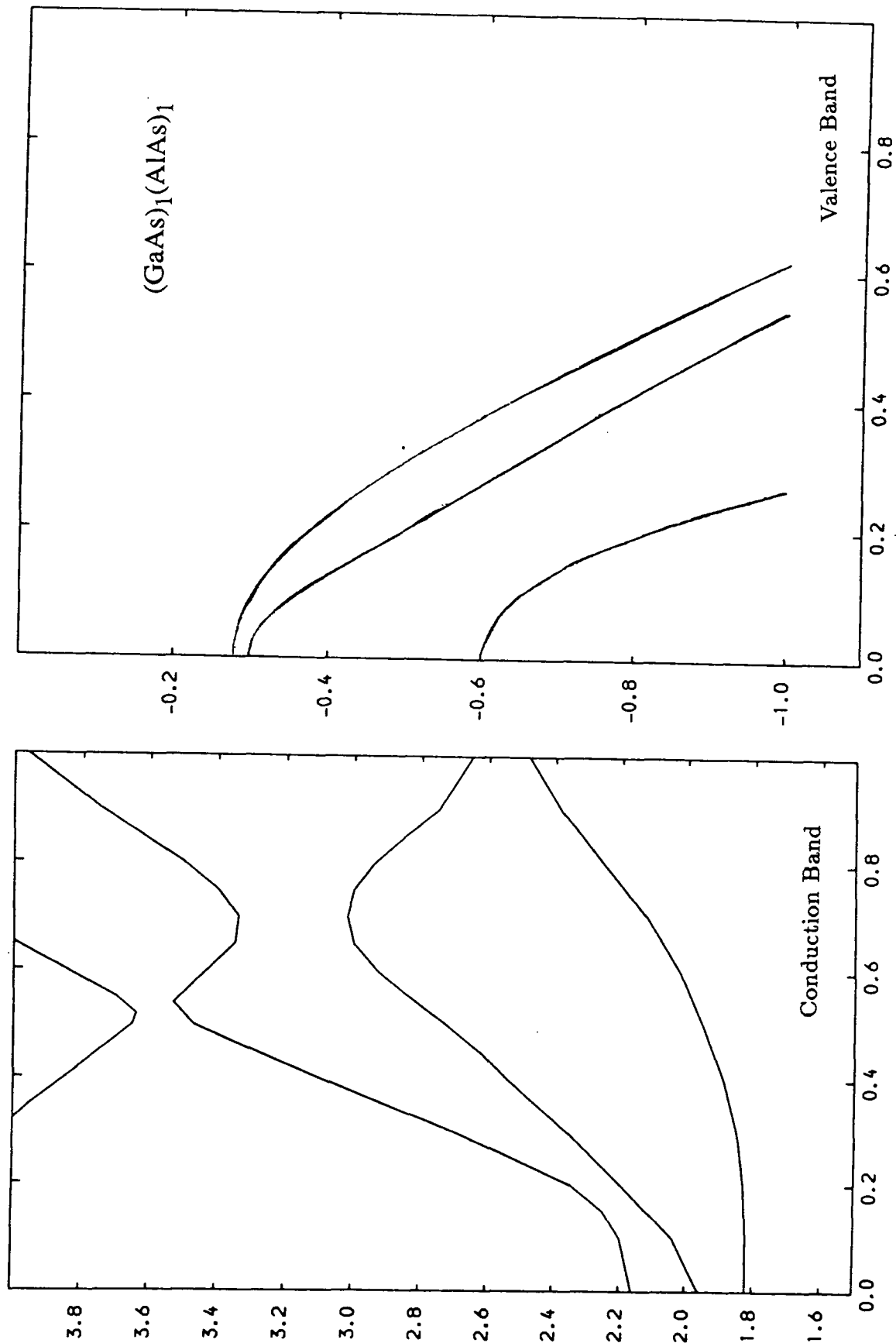
Figure (3.4) The calculated bandstructure of $(GaAs)_1(AlAs)_1$.
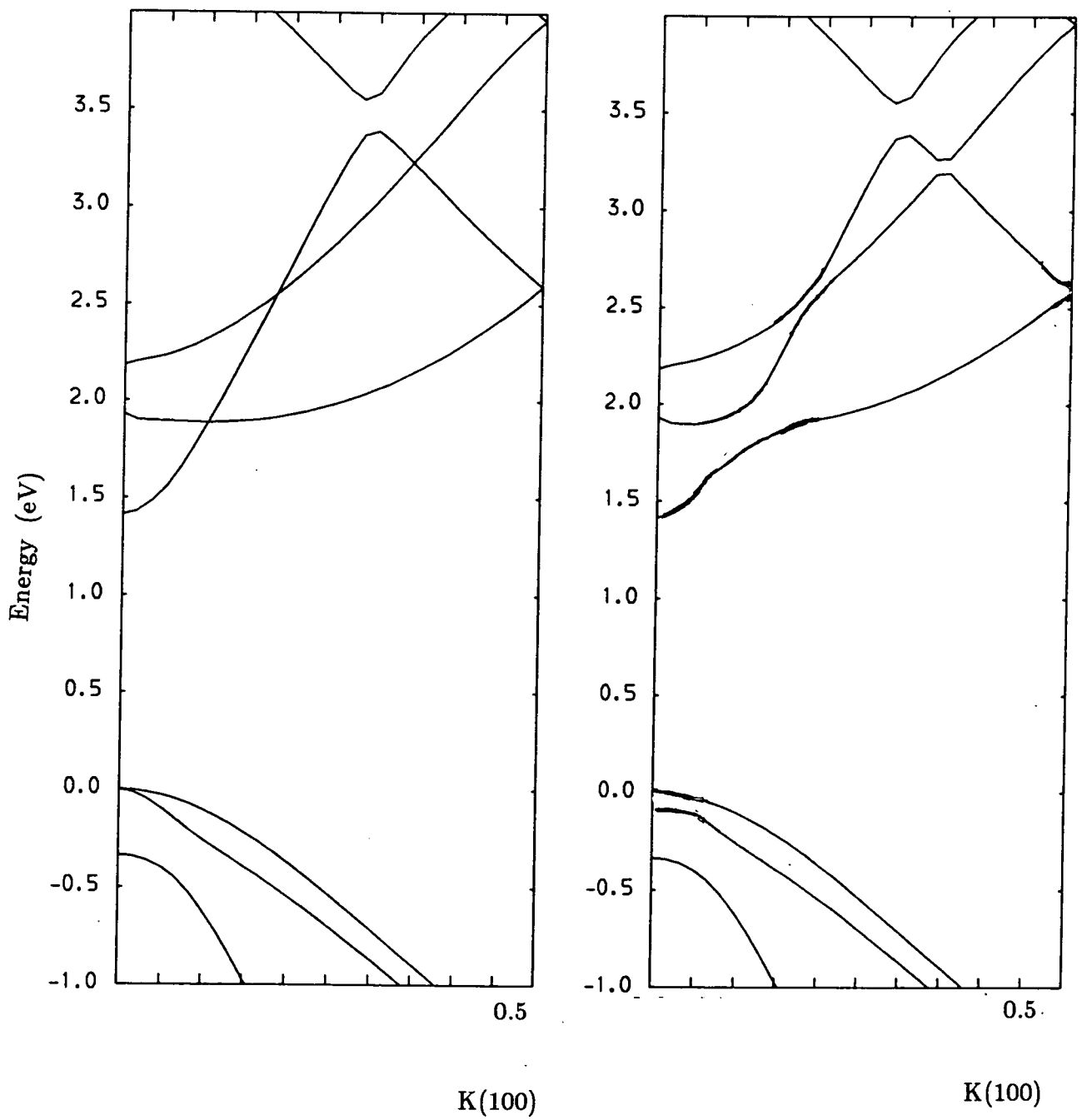
Figure (3.5) (a) Shows the bandstructure of (3.1) folded about k=0.5.
(b) Shows (a) with crossings transformed to anticrossings and
degenerate points at X split.

Mention of this work has been included for completeness. A more detailed description of a comparison between effective mass theory and a complex bandstructure matching technique will be given in relation to a quantum well in chapter 4; where a full description of anti-crossing and hybridisation effects will be found.

Figures (3.4) and (3.6)-(3.9) show the bandstructure of various short period $(GaAs)_m(AlAs)_m(100)$ superlattices. For all the diagrams the zero of energy is taken to be the top of the bulk GaAs valence band. Considering figure (3.4) we may ask how the bandstructure relates to a zonefolding approach as applied to the bandstructure of GaAs?

Starting with figure (3.1) we employ the technique of zonefolding. This entails, for a superlattice of unit cell equal to twice the unit cell of the bulk material, halving the length of the Brillouin zone in the direction of growth – (100) in this case – and folding back the states which lie outside the zone. This gives the situation depicted in figure 3.5(a). When we split the bands at crossing points we obtain the bandstructure of figure 3.5(b). It can be seen that the result is very similar to the calculated bandstructure of figure (3.4) for the $(GaAs)_1(AlAs)_1$ superlattice. In fact it is found to be generally true that zonefolding works well for $(GaAs)_m(AlAs)_m$ superlattices over a wide range of values of m and energies.

Calculations have been carried out on the $(GaAs)_1(AlAs)_1$ superlattice by other workers. A slightly different complex bandstructure matching technique has been used (Taylor, 1987) with the same pseudopotential

form factors to investigate ultrathin superlattices and found the same overall conduction bandstructure as has been shown here, but due to the limitations of the method – treating the x, y and z directions in different manners causes an artificial splitting at the top of the valence band – it was impossible to model the valence band. Others (Gell et al, 1986) have used the same parameters and offsets to model the conduction band of the $(GaAs)_1(AlAs)_1$ superlattice but find a totally different shape for the three lowest bands which they find increase monotonically from the Γ to X points. A tight binding method has been used (Nara, 1987) to calculate the overall bandstructure of this particular superlattice using various offsets and it gave the same general shape as was found in figure (3.4) whether a 85:15 (Dingle et al, 1974) or 60:40 offset (Kroemer et al, 1980) was used. From a more quantitative viewpoint it is important to consider the size of the smallest direct bandgap of the structure, and a more general discussion of bandgap variation with superlattice period will be given later.

From figure (3.4) we see that, at least when considering bandstructure in the (100) direction, the superlattice is direct with a bandgap of 2.09eV. Experimentally it has been found, by means of a photoluminescence method, that the bandgap is 2.10eV at room temperature (Ishibashi et al, 1985). Other experimentalists (Cardona et al, 1987) using a resonant Raman scattering technique have found a superlattice bandgap of 1.91eV. It is important to notice that these calculations have not included exciton effects, but these are expected to be small, even in the two-dimensional case, and

certainly affecting the size of the bandgaps by less than 20meV (Miller and Kleinman, 1985).

All the theoretical work mentioned above is of a non self-consistent nature. Yet the effects of charge transfer and relaxation may be expected to be of great importance when dealing with a superlattice with a period with a length of that of one unit cell of the bulk materials (one monolayer of AlAs followed by one of GaAs). A self-consistent pseudopotential calculation (Gilbert and Gurman, 1987) has shown that the charge transfer between layers, from AlAs to GaAs, was rather small but may be significant enough to change the offsets for small period superlattices and hence their energy levels. Nevertheless, the bandstructure of this self-consistent calculation is found to have the same form as that given in figure (3.4) and gives a direct gap of 2.07eV (compared with 2.09eV in our calculation).

Figure (3.6) shows the conduction and valence bandstructure for a $(GaAs)_2(AlAs)_2$ superlattice. It has been shown (Taylor, 1987) that the concept of zonefolding can be used to convert the $(GaAs)_1(AlAs)_1$ bandstructure to that of the $(GaAs)_2(AlAs)_2$ superlattice – which is equivalent to folding the bandstructure twice. Others (Gell et al, 1986) have also calculated the conduction bandstructure for this superlattice but here they find good agreement with our overall results, in contrast to the $(GaAs)_1(AlAs)_1$ results. Other theoretical calculations (Kamimura and Nakayama, 1987 and Nara, 1987) are also in very good agreement with the overall shape of our bands.

Figures (3.7), (3.8) and (3.9) show the valence and conduction bands for $(GaAs)_3(AlAs)_3$, $(GaAs)_4(AlAs)_4$ and $(GaAs)_6(AlAs)_6$ superlattices respectively. Rather than giving a detailed comparison with other works for these three superlattices we shall simply note a couple of trends of aspects of the bandstructure. We notice that the lowest conduction band and highest valence bands become progressively flatter. This may be viewed in two ways. Firstly as a direct consequence of continued zonefolding which in the limit will give completely flat (dispersionless) bands or as a consequence of the fact that the well regions – formed by the GaAs – will contain a greater percentage of the wavefunction as the barrier gets wider so that the carriers become more confined producing dispersionless bands.

The heavy and light-hole splitting at the top of the valence band increases with increasing superlattice period. Increasing from 20meV for the $(GaAs)_1(AlAs)_1$ superlattice to 60meV for $(GaAs)_6(AlAs)_6$ superlattice.

This effect can be seen as being caused by two conflicting physical processes. For the 1x1 superlattice we have a material which we may expect to have similar properties to a similarly constituted alloy. Since we know that for the alloy there is no splitting at the top of the valence band we may expect the splitting caused by the imposition of a 'superlattice' potential to be smallest for the short period superlattice. From a symmetry standpoint the overall symmetry of the alloy, T_d, is transformed to one of a lower symmetry: D_{2d}. As the barrier region becomes progressively wider the wells begin to decouple and the structure soon has the properties of a multiple
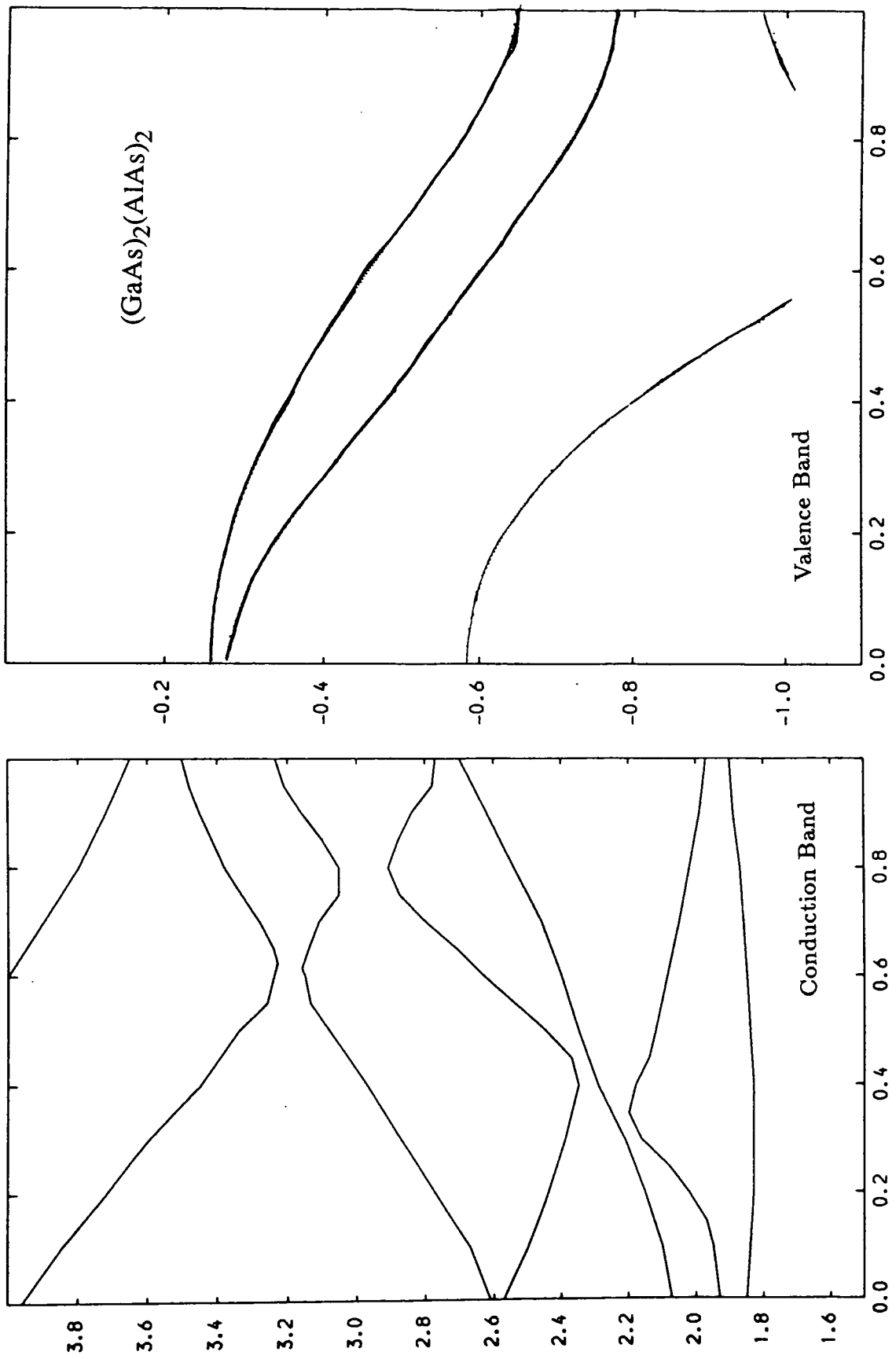
Figure (3.6) The calculated bandstructure of $(GaAs)_2(AlAs)_2$.
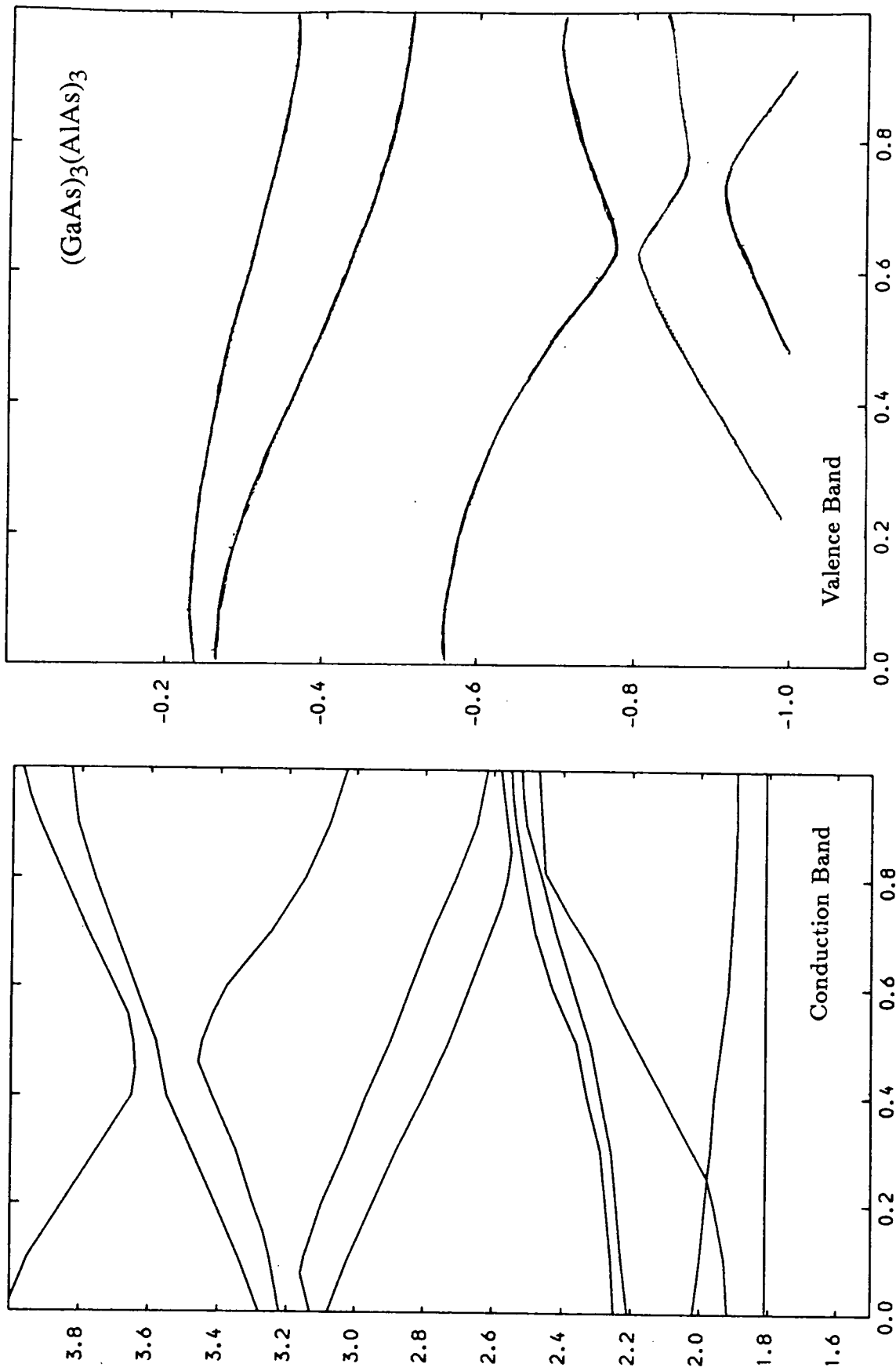
Figure (3.7) The calculated bandstructure of (GaAs)$_3$(AlAs)$_3$.
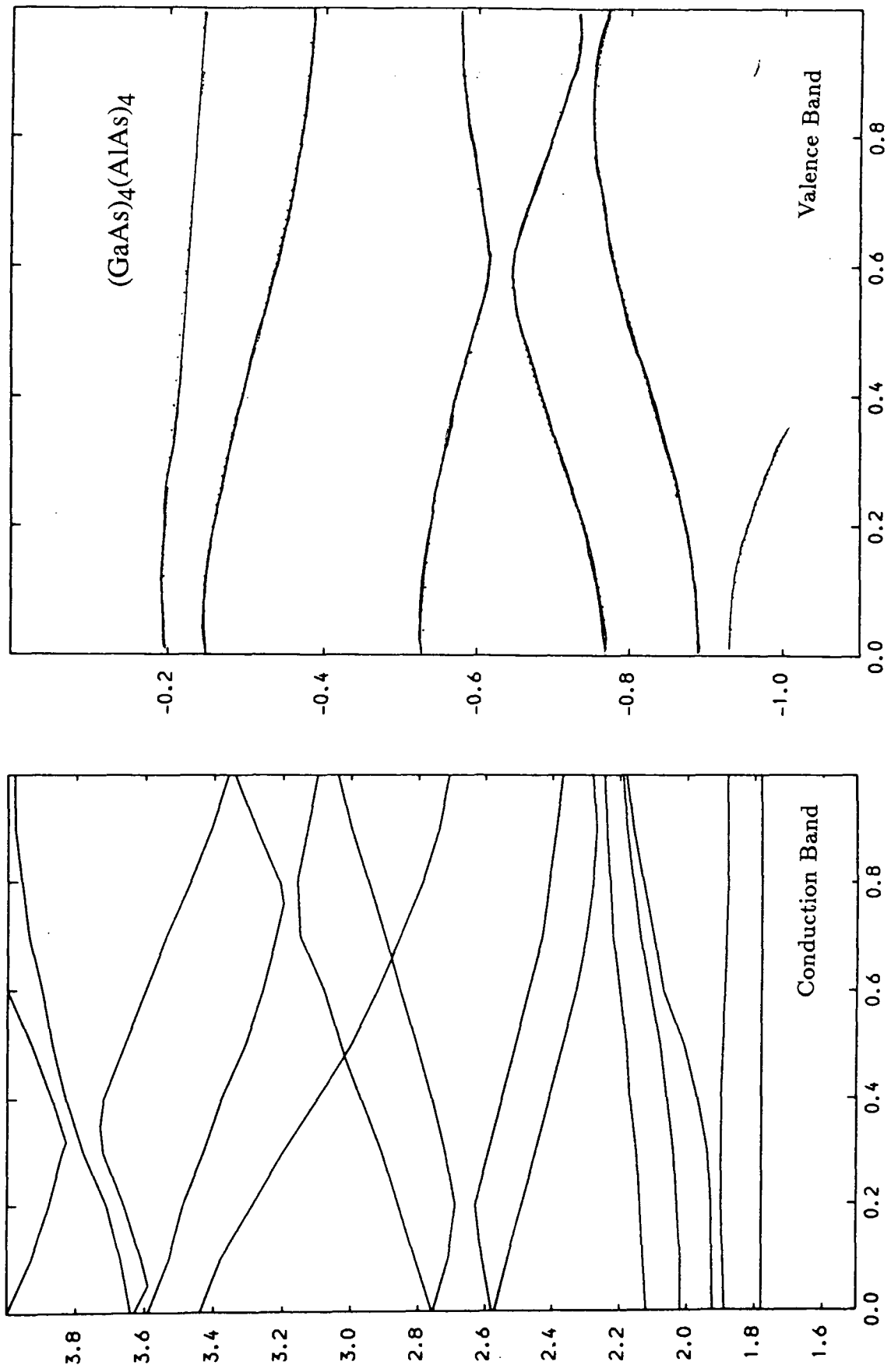
Figure (3.8) The calculated bandstructure of $(GaAs)_4(AlAs)_4$.
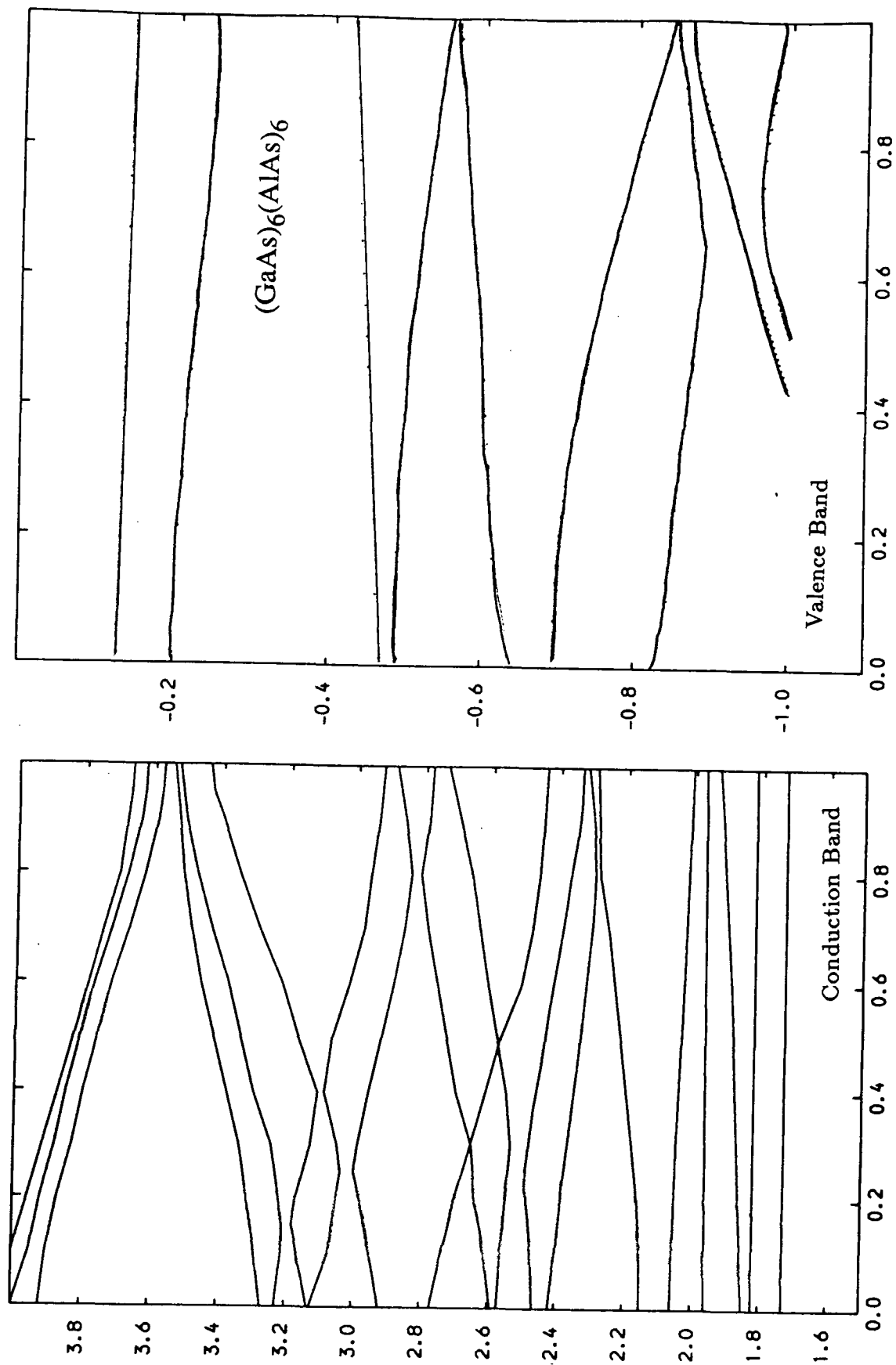
Figure (3.9) The calculated bandstructure of $(GaAs)_6(AlAs)_6$.

quantum well (we shall see later in this chapter that this happens for a superlattice of very short period). We expect, then, that as the wells get wider that the two states will approach each other as both drop down the well with increasing width.

Perhaps the most important feature of these superlattices is the variation of the bandgaps with superlattice period. Various workers have made a great deal of the indirect and direct nature of the superlattices but have come to no definite conclusion. The contention centres around the change from a smallest valence band–R transition (where R represents the zonefolded L-point for a 1x1 superlattice, although the nomenclature is not standardised) to a smallest direct transition for larger periods. Although this discussion is interesting and may have important technological consequences, it seems, for the moment, to be virtually impossible, due to the large effects of small causes such as different offsets, to reconcile the differences. Consequently, we shall only consider the (100) direction and the smallest valence-conduction bandgap and how it varies with superlattice period.

Superlattice	Calculated Direct Bandgap
1x1	2.09eV
2x2	2.10eV
3x3	2.03eV
4x4	1.96eV
5x5	1.90eV
6x6	1.86eV
7x7	1.82eV
8x8	1.78eV

Figure (3.10) shows the variation of the Γ–Γ and Γ–X bandgaps with m for a $(GaAs)_m(AlAs)_m$ superlattice. The overall trend, as we would expect is a general reduction in the size of the bandgap with increasing m. The exception to this is for the $(GaAs)_1(AlAs)_1$ superlattice which has a smaller bandgap than the $(GaAs)_2(AlAs)_2$ superlattice. The smaller bandgap for the 1x1 superlattice may be considered to be an effect of strong well to well coupling. This can be seen as allowing the superlattice wavefunction a greater extension in real space allowing it to take up a lower energy configuration. By the time the superlattice period has become equal to two unit cells of the bulk materials the decoupling has reduced markedly and so the energy levels, to a certain extent, take on the nature of those which would be found in single quantum wells. More quantitatively for an mxm superlattice of barrier width b and decay constant q (assumed large) in the barrier region there is an energy contribution which can be approximated by the uncertainty principle of order

$$E_{kinetic} = \frac{h^2}{8\pi^2 m(b + 2/q)^2}$$

and an interaction term which is set by the overlap in the barrier region of order

$$E_{interaction} \propto be^{-bq}.$$

The exact nature of these competing terms is of a complex form preventing a simple analytical solution.

As noted earlier the dispersion, given by the Γ–X separation de-
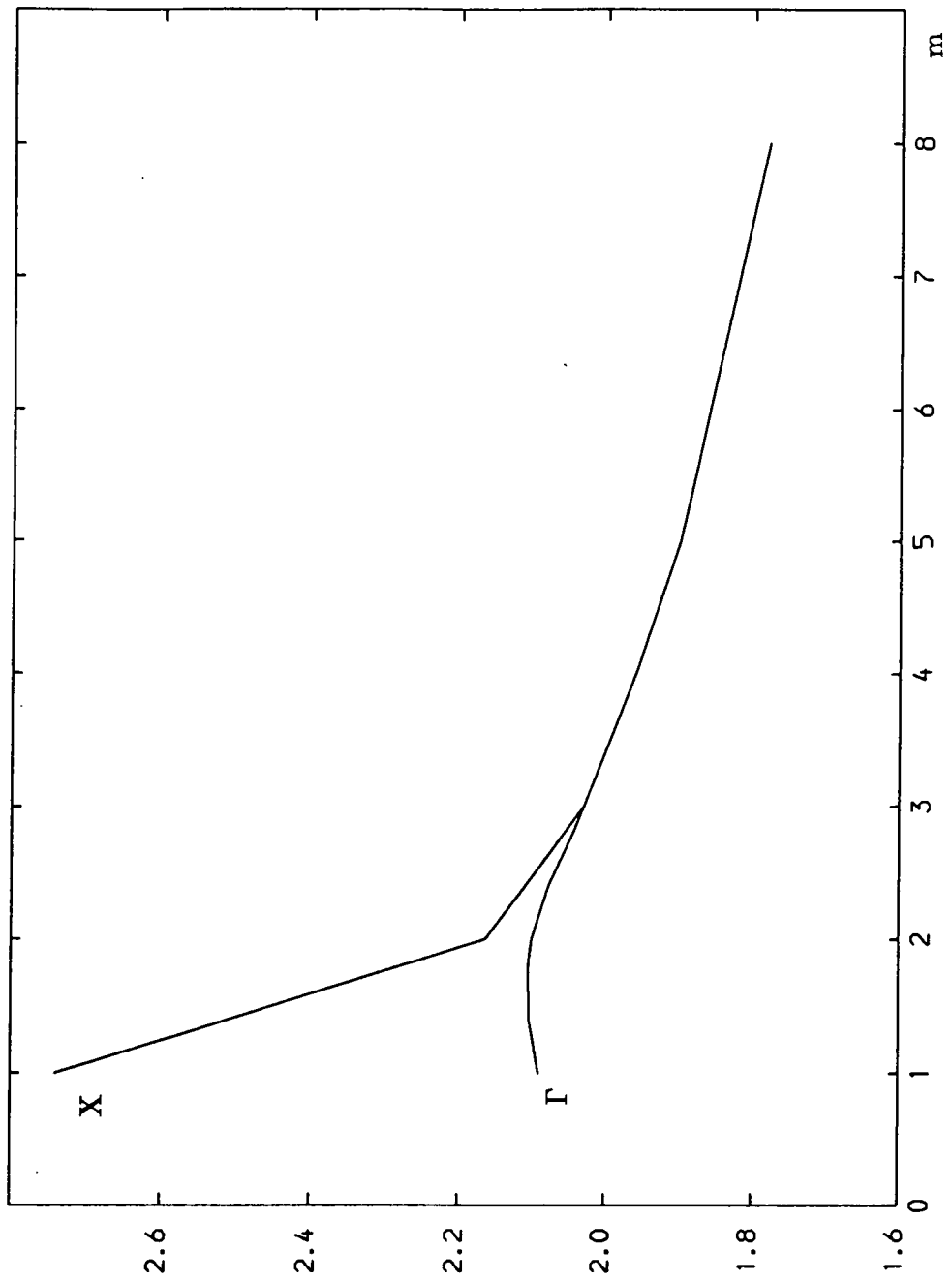
Figure (3.10) Variation of superlattice X and Gamma points in the (100) direction with m for $(GaAs)_m(AlAs)_m$ superlattices. The dispersion is unobservable for superlattices with m greater than 3.

creases rapidly with width. In fact for the $(GaAs)_3(AlAs)_3$ superlattice the separation is less than 3.0meV. It is important to notice that the Γ and X points have been chosen as 'representative' of the bandstructure since, as can be seen for figure (3.5) the lowest conduction band state in the (100) direction lies approximately 30% of the way to the zone boundary.

An experimental investigation of the variation of bandgap with superlattice period was carried out using photoluminescence measurements (Ishibashi et al, 1985). This work, until recently, has been taken to be the standard experimental yardstick against which theoretical results are measured. The experiment was carried out on a superlattice grown by MOCVD at temperatures of 300K and 4.2K. For the measurements at room temperature the variation of the direct bandgap with period is similar to that given in figure (3.10) with the gap varying between 2.1eV and 1.8eV (compared with 2.09 and 1.78eV for our work) for superlattices in the range 1×1 to 8×8.

More recently an experimental and theoretical investigation of the $m\times m$ superlattices has been carried out (Moore et al, 1988). These workers find that a k.p method can be used to model the smallest bandgaps for $m >6$. By using various photoluminescence techniques they were able to show the same overall trends as in figure (3.10) with a bandgap of about 2.0eV for m=5 at a temperature of 5K (compared with 1.90eV for our calculation at 100K).

In passing we note that a self consistent local pseudopotential method

Figure (3.11) The valence band structure for $(GaAs)_m(AlAs)_n$ with
$m+n=12$. (a) Shows the results of our complex bandstructure
technique for the superlattice Γ states. (b) Shows the same regime
using a non-matching pseudopotential method (see text for details).

has been carried out for (AlAs)(GaAs)(110) superlattices (Ferraz and Srivastava, 1986) and found a similar variation in bandgap with superlattice period but with a considerably smaller bandgap – although any real comparison is difficult since the superlattice is of a different orientation and with a smaller valence band offset of 0.25eV.

A detailed comparison with the calculations of Gell (Gell et al, 1986) will now be given. We shall, as stated above, be using the same models for the bulk bandstructure. As well as the results for the ultrathin superlattices already discussed, these workers have carried out an investigation of a set of $(GaAs)_m(AlAs)_n$ superlattices for $m + n = 12$. This seemingly odd choice is brought about as a consequence of the method used which unfortunately does not allow a simple investigation of trends in $m \times m$ superlattices etc. Figure (3.11) gives a direct comparison of the Γ-related states for some of the valence band states of such systems. On the right and left sides of figures (3.11a) and (3.11b) the points corresponding to the zonefolded bandstructures of GaAs and AlAs have been marked. The similarity between the sets of results is quite striking. In fact the only notable difference is for the $n = 11$ superlattice 4th and 5th states which in the Gell calculation seem to be displaying an interaction whereas in our calculation the state seems to be unaffected by the presence of other bands.

There are two possible explanations for this, very small, effect. For this particular superlattice we are dealing with a few monolayers of GaAs which, from a computational view point, as discussed above, is open to

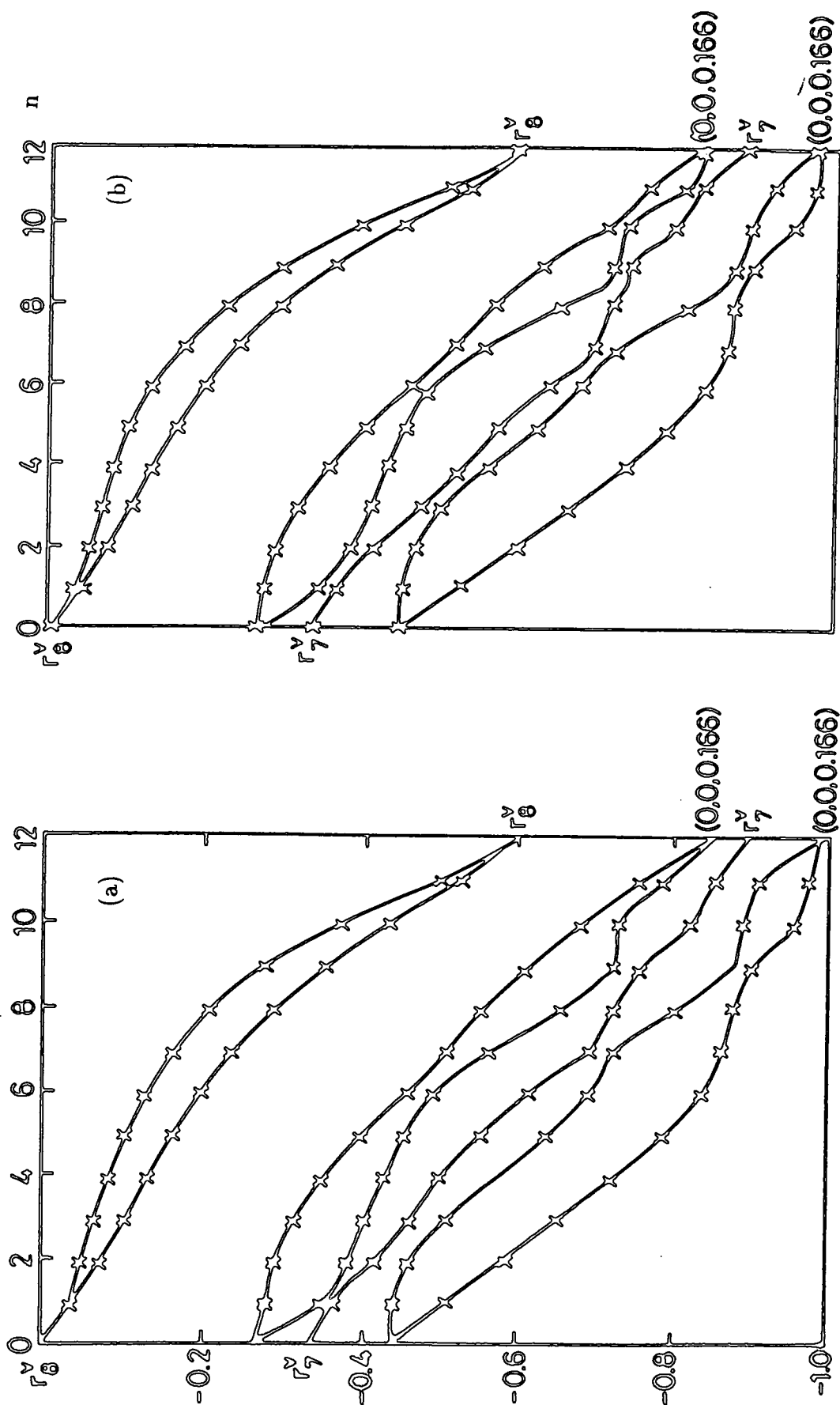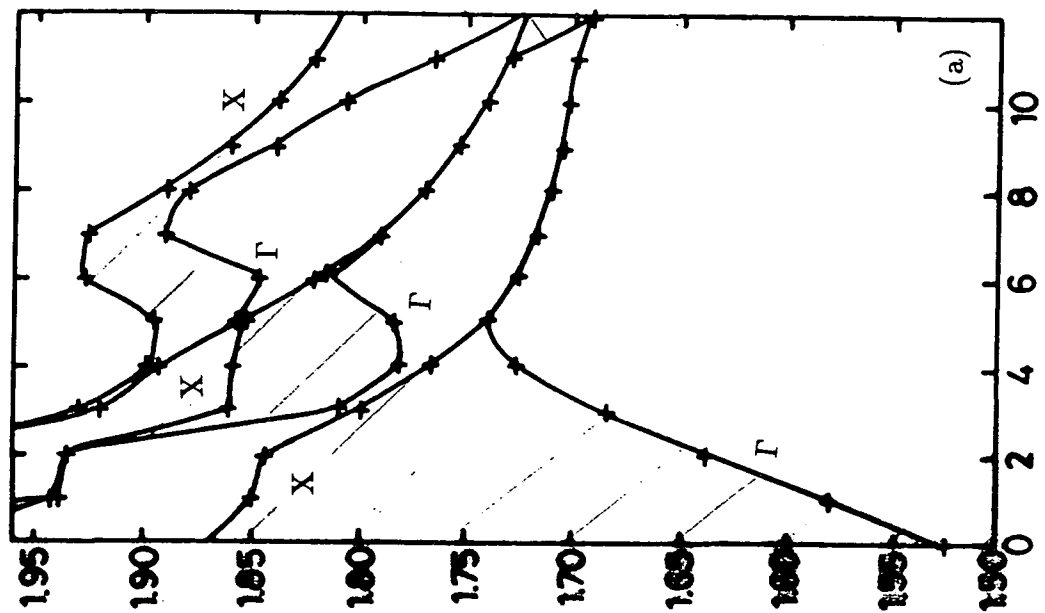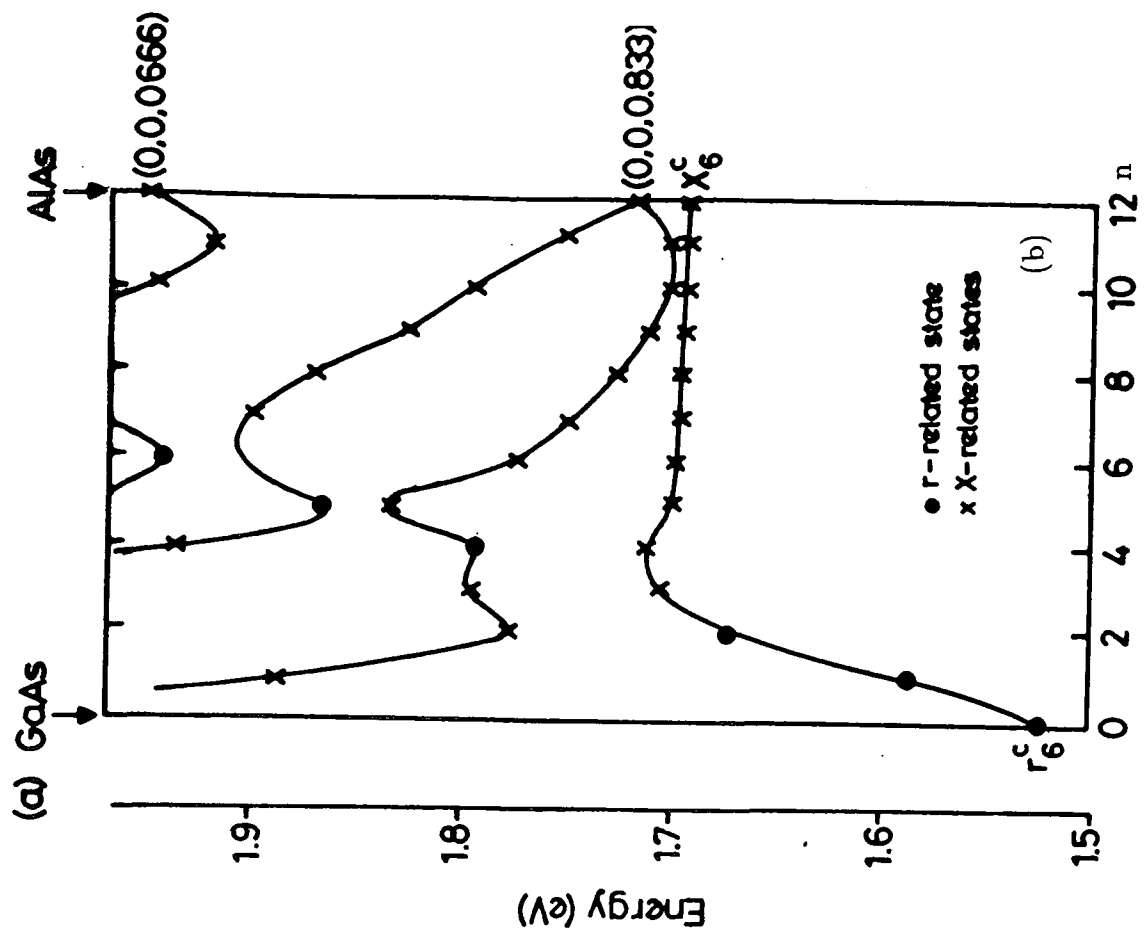Figure (3.12)   The conduction bandstructure for $(GaAs)_m(AlAs)_n$ with m+n=12.   (a)   Shows the results of our complex bandstructure technique for the superlattice Γ and X states.   (b)   Shows a similar regime but only for the Γ states using a non-matching pseudopotential method (see text for details).

a certain amount of doubt due to charge transfer and relaxation effects. These phenomena are 'ignored equally' by the two methods but the different calculations may be considered to be using different convergence criteria which will be important for the narrowest structures. In particular it is interesting to note that the only discrepancy between the work of Gell et al and this work for the 1x1 and 2x2 superlattices is for the smaller structure. Alternatively the effect may be a direct consequence of the different calculational procedure used – of which more will be said now with reference to the conduction band.

Figure (3.12) gives a similar comparison for the conduction band states of the superlattice. Figure (3.12a) also gives the superlattice X-states and consequently gives an indication of the dispersion in the (100) direction.

The overall behaviour is rather as one might expect with two sets of interacting bands, one of which is determined by the width of the GaAs wells and the effective masses of the Γ-like electrons and one set which is dependent on the width of the AlAs barriers and the effective masses of the X-like electrons. In figures (3.12a) and (3.12b) the comparison is seen to be not as close as for the valence bands of figure (3.11). The most notable difference is for the N=10, 11, 12 region of the second Γ-like band. In the Gell calculations we notice an extreme camel's back structure whereas in our calculation the band flattens off towards $N = 12$ in a straightforward monotonic manner. An associated effect seems to be influencing the lowest conduction band which in the Gell calculation appears flat for $5 < N < 12$

but in our calculation the band follows the general trend of the X-related electrons.

This must be a direct consequence of the difference in the methods used. Whereas our complex bandstructure matching technique takes all states at a particular energy to make up the overall wavefunction, the method used by Gell et al forms the superlattice wavefunction from a few bands incorporating a range of energies. This may have consequences for the interaction of X and Γ states. Also the exact nature of the differences of the methods when calculating the bandstructure at points of interaction may be affected by the exact form of the bulk bandstructures. This is especially true around the X-point of AlAs where experiments on electron-hole liquids have shown a pronounced camel's back (Bimburg et al, 1981).

Summary.

We have given a detailed comparison of the results of our complex bandstructure matching technique and described how they compare with other calculations and with experiment. Overall agreement is very good with any discrepancies between this work and others being no worse than the spread in results of the other work taken as a whole.

This leads us to believe that the complex bandstructure matching technique does give – within the limits of the accuracy of the bulk band-structure – a correct representation of low dimensional bandstructure whilst retaining the symmetry and non-parabolicities which would be left out of simpler calculations. Also it allows a rapid investigation, when compared to

a supercell calculation, of variation with well and barrier width and variation of superlattice wavevector.

In the next chapter we shall consider some properties of low dimensional structures, such as hybridisation, with reference to quantum wells.

CHAPTER FOUR

BOUND STATES OF AlGaAs QUANTUM WELLS

Introduction.

In the previous chapter we saw how the complex bandstructure matching technique gave good agreement with many other calculations including full scale self-consistent calculations.

In comparison to superlattices aperiodic structures have not received the same intensive theoretical study and full scale calculations have been few. One particular exception is the study of barrier structures (Marsh and Inkson, 1986 based on earlier work by Burt and Inkson, 1976).

In this chapter we shall consider two 'sets' of quantum well structures; one of the form AlAs/GaAs/AlAs and the other formed with alloy barriers of the type $Al_{0.3}Ga_{0.7}As/GaAs/Al_{0.3}Ga_{0.7}As$.

We shall confine ourselves to considering work on the neglected valence band states of these structures, and shall show that these states are rich in structure and physical interest.

Calculation.

Throughout the following calculations the in-plane wavevector will be taken to be zero. Twenty seven plane waves (per spin orientation) have
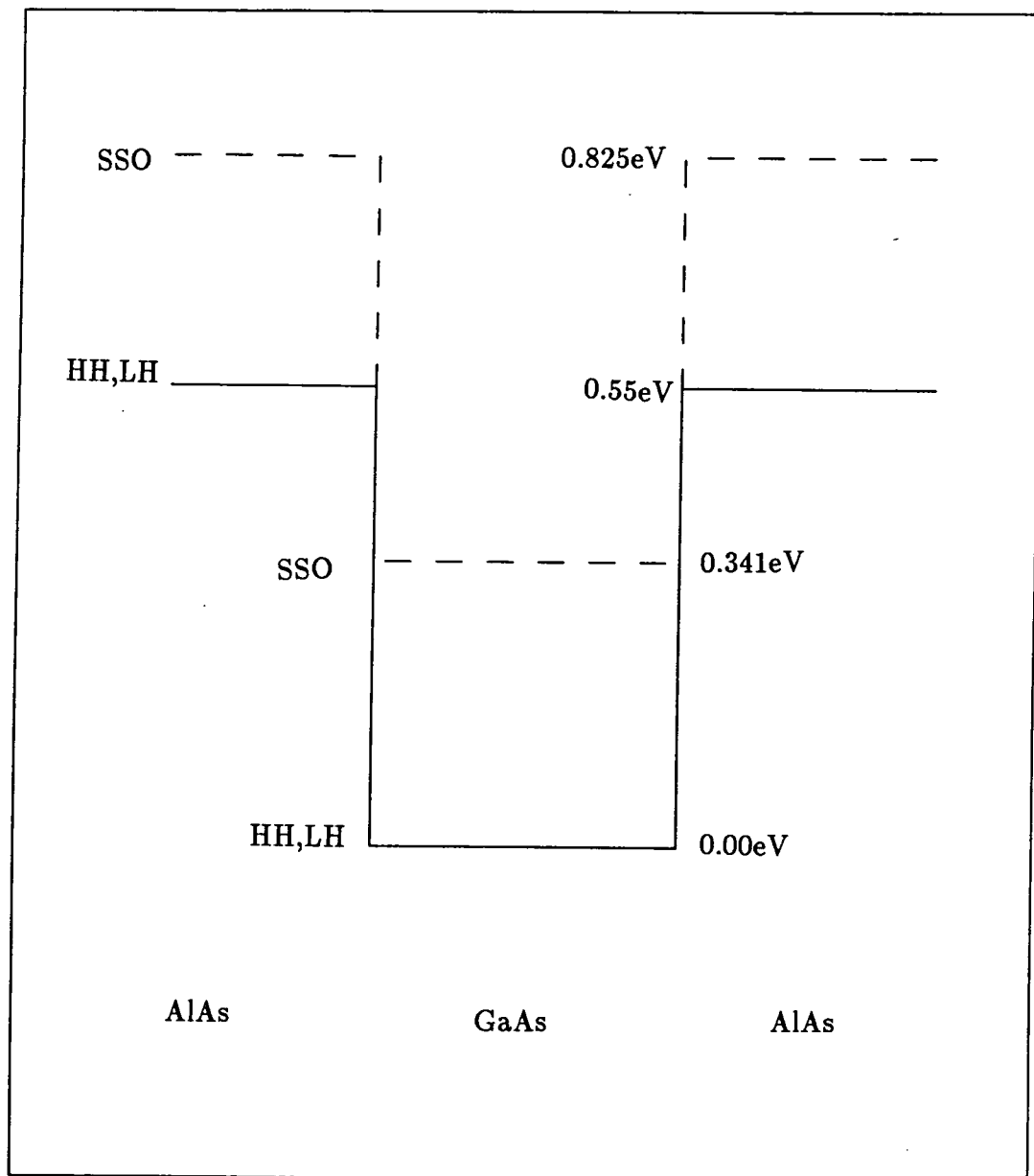
Figure (4.1)   Band Offsets for AlAs/GaAs/AlAs quantum well. Solid lines represent well appropriate to heavy and light hole states whilst the dashed indicate the extent of the spin-split-off quantum well.

been used in the calculation of the complex bandstructure. The inclusion of additional plane waves has little effect on the final solutions of the quantum well problem but does have the significant effect of incurring substantial computational penalties.

The pseudopotentials used (Szydlik, 1986) are chosen such that the bandgap, spin-orbit splitting at Γ and the positions of the secondary minima are in good agreement with experiment when 27 plane waves are used. Using these parameters we find that increasing the number of plane waves from 27 to 65 results in a change in effective masses of less than 3%.

The AlAs/GaAs/AlAs Quantum Well.

For the non-alloy quantum well the valence band offset is taken to be 0.55eV consistent with the '0.55x' rule as found in the literature (Batey and Wright, 1985). Combined with the values for spin-split-off and the form of the bandstructures as obtained from a pseudopotential calculation we obtain the offsets of figure (4.1). For completeness we show how the valence band offset aligns the overall bandstructure in figure (4.2) which also includes the conduction band states.

Using the method discussed in chapter 2 we have investigated various properties of the bound-state energy levels of the quantum well for widths ranging from one monolayer (≈ 2.7Å) to 80Å.

Figure (4.3) shows how the various energy states vary with quantum well width. The overall trend of any particular state is to fall down the valence band well (using the energy convention implicit in figure (4.1)) and
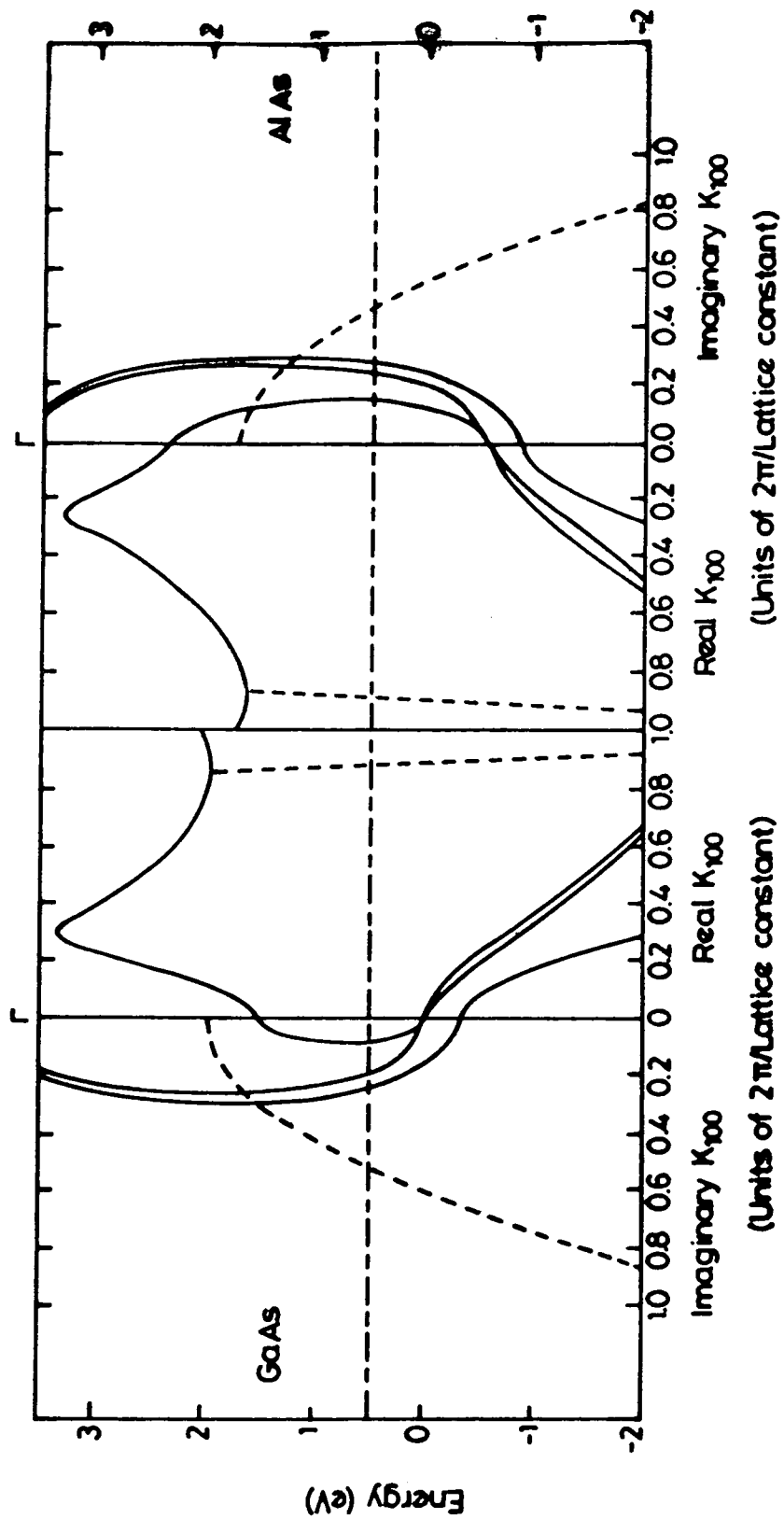
Figure (4.2)   Bandstructure of GaAs and AlAs indicating the offsets used in the chapter. The dashed lines show the real and imaginary solutions to a general complex state.

tend asymptotically towards the zero of energy for large widths. It is obvious, however, that other physical processes are at work. In particular there appear to be many points where anti-crossing phenomena are occurring such as the interaction between the lines labelled LH3 and HH4 around a quantum well width of 50Å. It is also fairly clear that many of these interactions seem to be occurring around an energy of about 0.35eV.

The reasons for these two effects are simple to understand. The interaction between bands can be seen as a consequence of the fact that the quantum well heavy hole, light hole and spin-split-off states all have the same symmetry and hence cannot cross (Cornwell, 1969). Reference to figure (4.1) shows why there is so much activity around about 0.35eV. If only the spin-split-off states are considered with their offsets we see that rather than experiencing a well of depth 0.55eV the spin-split-off holes 'see' a well of depth 0.484eV or eqivalently the bottom of the spin-split-off well is 0.341eV above the bottom of the heavy and light hole well.

Consequently the spin-split-off states are 'bottoming out' at an energy of 0.341eV. In an effective mass picture of this situation we would expect the more rapidly falling heavy and light hole states to cross these spin-split-off states; but, as has already been stated, the lines cannot cross and so many anti-crossings occur around 0.341eV. It is important, however to notice that anti-crossings can and do occur between light and heavy hole states as indicated by the arrowed lines in figure (4.3). More will be said of these states later.
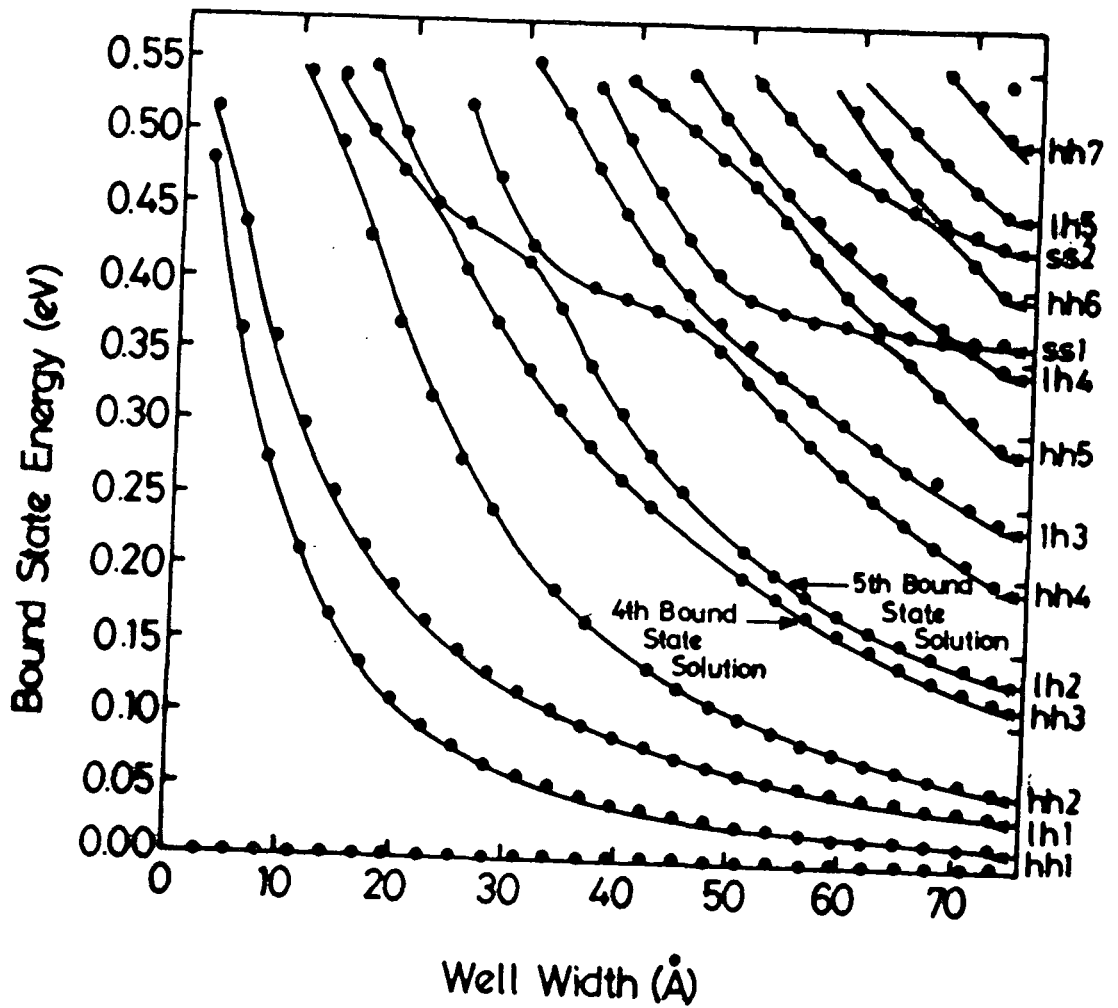
Figure (4.3) The bound state energies for the AlAs/GaAs/AlAs quantum well as a function of width. The energies are measured downwards from the GaAs valence band edge. The full circles show the calculated energies and the continuous curves have been added to clarify the anti-crossing behaviour. The full circles on the width axis indicate the integer number of monolayers. '4' and '5' indicate the fourth and fifth-bound state solutions.

Figure (4.4) shows the (pseudo-) charge densities corresponding to the three lowest solutions for the 26 monolayer width quantum well (73.5Å) in the direction perpendicular to the interface planes and through the bond centres. The large width and large barrier height makes all three states very localised in the well. They can be seen to have the characteristic envelope structure that we might expect from these states. One slight difference between what might be expected from an envelope function approach and the present calculation is the slight asymmetry in the peak structure for the HH2 state. This is due to a small LH-like admixture. All the states shown in figure (4.4) have a quantum well wavefunction contribution from the dominant band which is greater than 90% which has been determined by evaluating the expansion coefficients of the superlattice wavefunction. It is obvious that even a small mixing with other bands can have significant effects on the wavefunctions and hence on the charge densities.

Some more extreme examples of mixing and its effect on the wavefunction will be given when the alloy superlattice is discussed later but here we shall explain the mechanism which can produce what seems to be an asymmetry in a symmetrical quantum well.

In effect the first part of the solution is given by figure (4.5). We shall, for simplicity, consider an infinite quantum well by using an envelope function approximation for the two states which we wish to discuss. The appropriate forms for the wavefunctions of LH1 and HH2 are shown in figure (4.5.1.a) and (4.5.3.a) with LH1 representing a nodeless ground state and
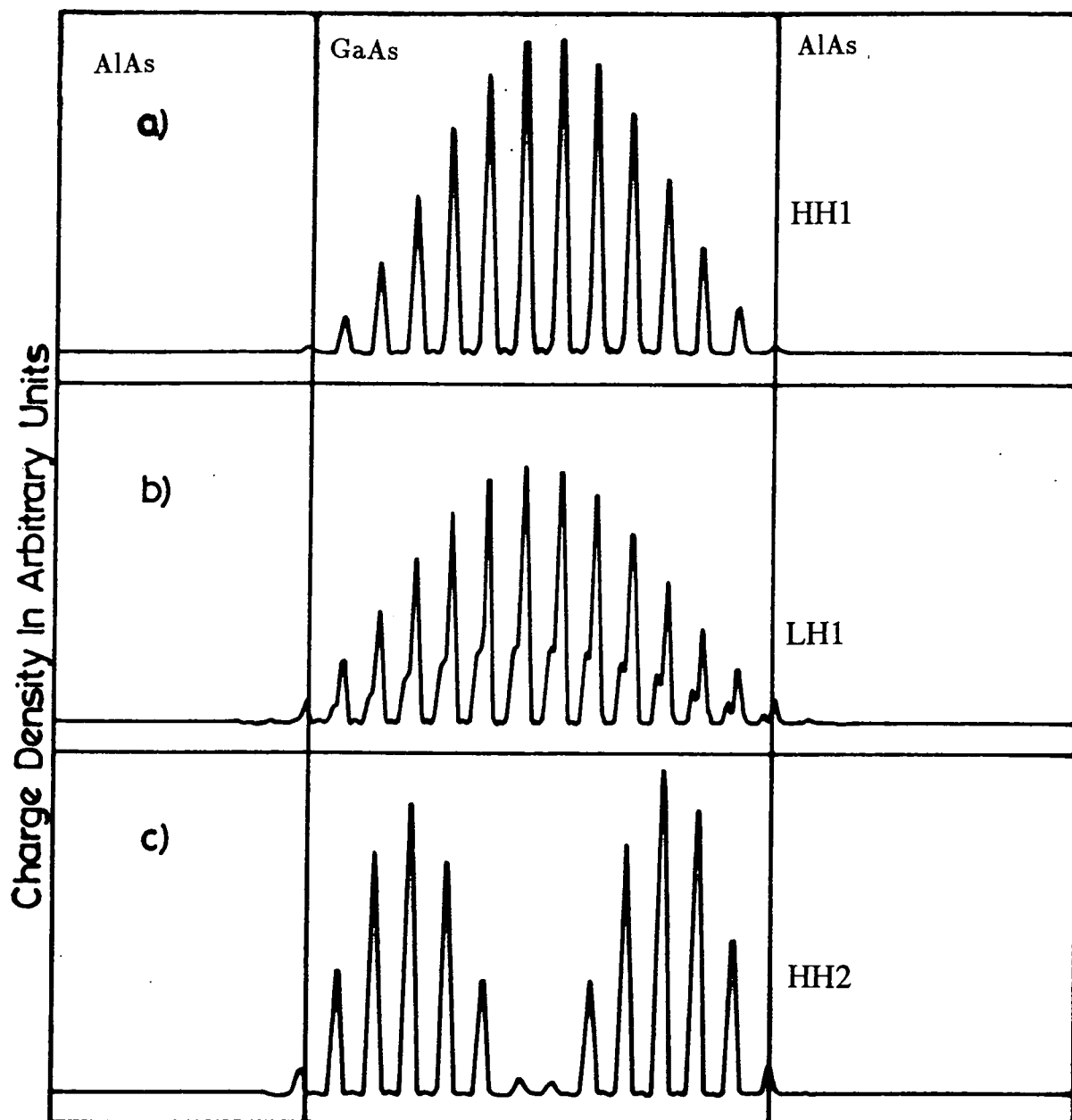
Figure (4.4)   The charge density of the first three bound states through bond
centres and through a line perpendicular to the interface   planes .
(a) HH1, E=0.013eV;   (b) LH1, E=0.035eV;   (c) HH2; E=0.052eV. The well
width is 73.5Å   which corresponds to 26 monolayers of GaAs.

Ψ Ψ^2

LH1

1.a   1.b

HH2

2.a   2.b

$HH2 + 10\%LH1$

3.a   3.b
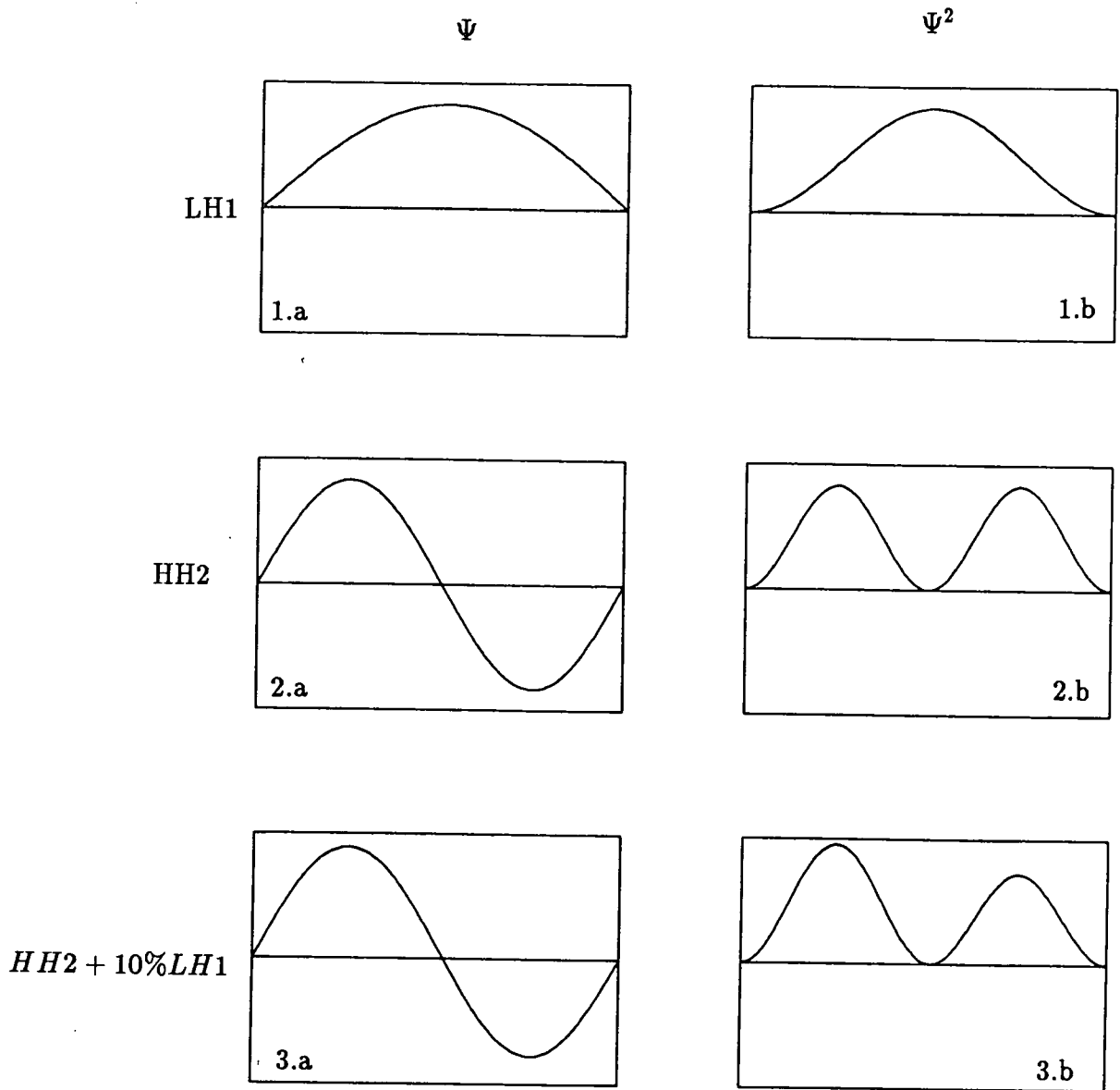
Figure (4.5) Schematic diagram of 'envelope function' mixing as explained
      in the text.

HH2 representing the first excited state with a single node. If there is only a 10% admixture of LH1 with the HH2 wavefunction we obtain the skewed wavefunction of figure (4.5.3.a) which when squared up gives the asymmetric charge density of (4.5.3.b).

So we see that mixing can form an asymmetric wavefunction even in a symmetric well. Nevertheless, the above argument could just as easily be carried out for states in which we mix the light hole with the negative of the HH2 state (which must be an eigenfunction of any Hamiltonian for which the positive HH2 state is a solution). This would also give an asymmetric charge density but with the larger peak on the right of figure (4.5.3.b). So it seems that the asymmetry is undetermined in some sense. Returning to the full pseudopotential method, it is found that the charge density is reversed in the manner just described if it is plotted along a line displaced by A/4 (where A is the bulk lattice constant) in a direction perpendicular to the direction of growth and in a plane of the bulk unit cell, i.e. if figure (4.4.c) is plotted along the line $(x,0,0)$ we now plot along the line $(x,\frac{1}{4}A,0)$. This leads us to suspect that the wavefunction averaged over an interface may not exhibit any asymmetry. This is found to be the case, and in figure (4.6) the planar averaged charge density, as defined in chapter 2, is plotted for the state denoted as HH2. Clearly the asymmetry has been averaged out as predicted.

We shall now return to the arrowed states of figure (4.3). On the extreme right hand side of this figure the states have been labelled in

terms of their dominant band contribution for quantum wells of width 27 monolayers. It will be instructive, however, to consider how the composition of the fourth state varies with well width.

Figure (4.7) shows the contributions for the light, heavy and spin-split-off bands in the well region for the fourth-bound state solution as a function of well width. It is important to notice that contributions from other bands are negligible. The behaviour of the three contributions is complicated but is worth considering in some detail.

For a width of approximately 20Å we find that the fourth-bound state solution is mainly spin-split-off with approximately 15% LH and a very small amount of heavy hole mixed in. Above 20Å the spin-split-off contribution falls rapidly with a complementary rise in the light hole contribution. So that at 25Å the spin-split-off contribution is around 10% while the light hole contribution is above 80% – the heavy hole remains unaffected over this range. This same process can be observed in figure (4.3) where the band in question obviously experiences a very strong interaction in the 20Å-25Å range where a light and spin-split-off anti-crossing occurs.

The next prominent feature is at about 32Å where there is a large peak in the spin-split-off contribution and a marked decrease in the light hole and heavy hole components. This width corresponds to the fourth bound state passing through an energy of 0.341eV; which represents the spin-split-off band edge of GaAs. This effect can be envisaged as a 'squeezing out' of the spin-split-off part of the wavefunction as it passes through the band
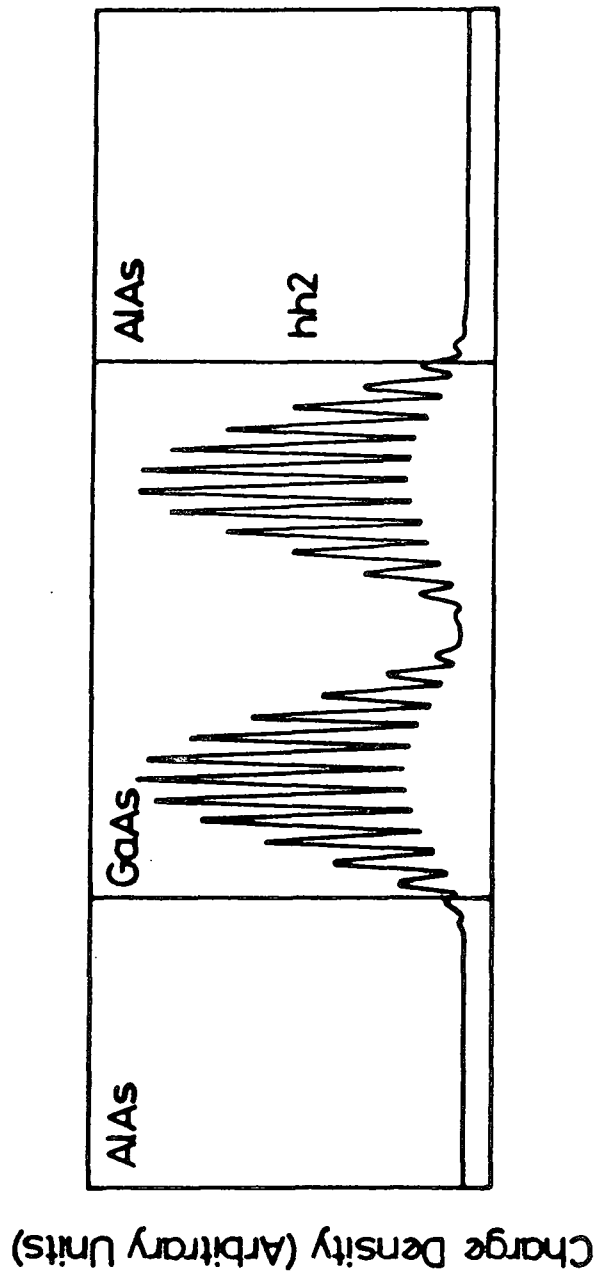
Figure (4.6) The charge density associated with the state shown in figure (4.4.c) averaged over planes parallel to the quantum well interfaces.

edge and has been predicted by others using an extended envelope function approximation (Taylor and Burt, 1987).

For larger widths the spin-split-off states actually correspond to imaginary evanescent solutions of the Hamiltonian and their contribution falls rapidly with increasing width. As the well width increases beyond 40Å the heavy hole contribution increases rapidly until at about 57Å the light and heavy hole contributions are equal. This anti-crossing effect, however, cannot be unambiguously inferred from figure (4.3) where bands 4 and 5 seem to be experiencing no, or very little, interaction.

The $Al_{0.3}Ga_{0.7}As$ Quantum Well.

For this quantum well with alloy barriers it is necessary to calculate the bandstructure of $Al_{0.3}Ga_{0.7}As$. This was done by means of a virtual crystal approximation assuming a linear interpolation between the pseudopotential form factors of GaAs and AlAs. So that, for instance, the alloy symmetric pseudopotential formfactor for $G^2 = 3$, V_3^{alloy}, is obtained from

$$V_3^{alloy} = 0.3V_3^{AlAs} + 0.7V_3^{GaAs}.$$

where V_3^{GaAs} and V_3^{AlAs} are the formfactors for $G^2 = 3$ for the two non-alloy materials. The valence band offset in the following calculations is taken to be 0.16eV, corresponding to a 60:40 ratio for the conduction:valence band offset. In this case the spin-split-off band exists above the top of the shallower well and consequently plays only a minor role in determining the energy states within the well.
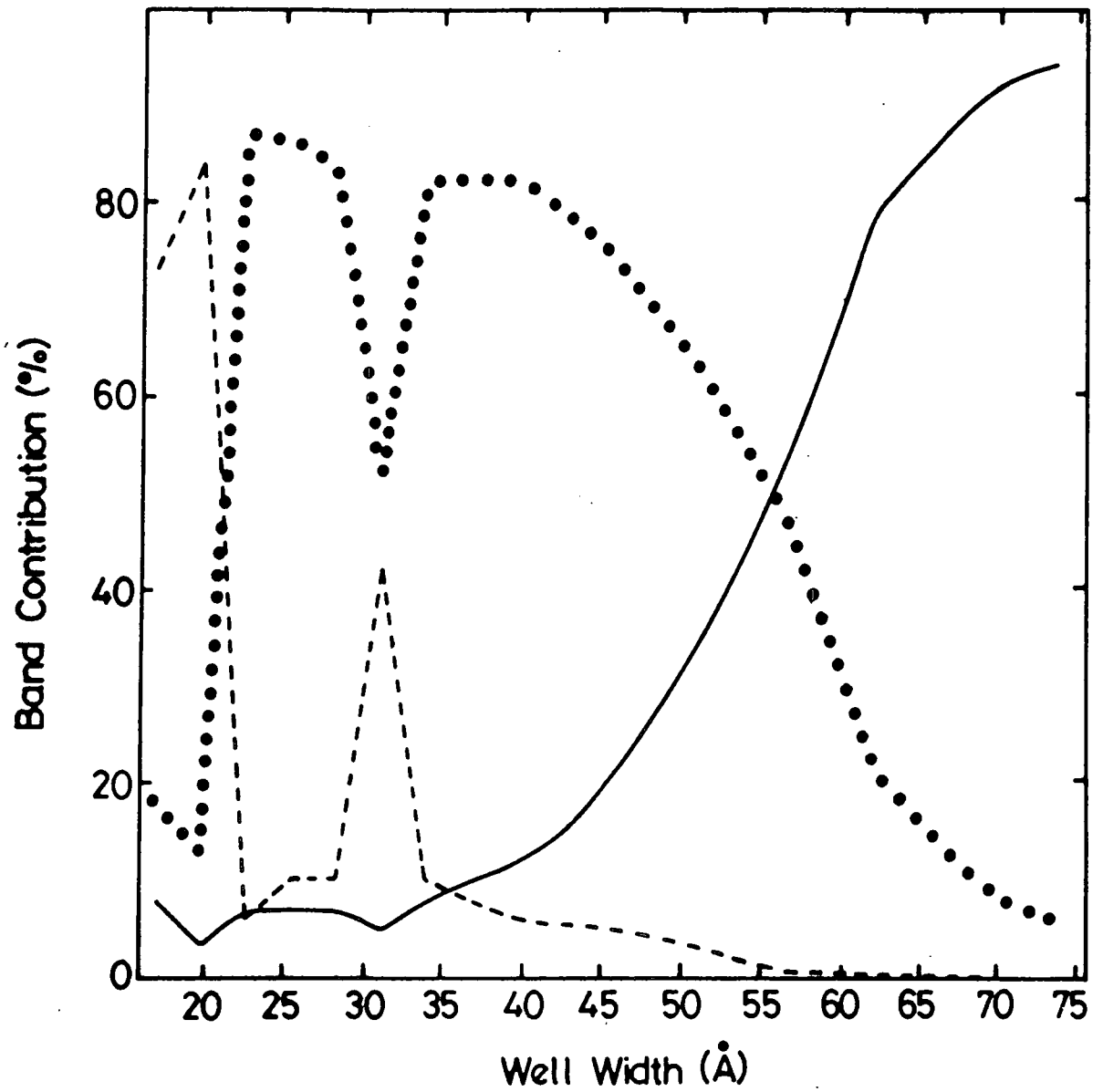
Figure (4.7) The percentage contributions for the heavy (full curve), light (dotted curve) and spin-split-off (broken curve) bands in the well region for the fourth-bound-state solution as a function of well width for the AlAs/GaAs/AlAs quantum well.

Figure (4.8) shows the variation in bound state energies over a wide range of well widths – as indicated by the full circles. Also shown, for comparison, are the continuous lines obtained using a simple position dependent effective mass model (Brand and Abram, 1983). The effective mass lines are labelled with their type designation. Four effective masses are necessary for such a calculation and are obtained from the bulk bandstructures for regions near to the Γ-point. For completeness we give the effective masses here:

	GaAs	AlAs
HH	0.428	0.428
LH	0.118	0.145

where, of course, GaAs is the well material and AlAs forms the barrier.

Figure (4.8) shows that for the first and third states the agreement between an effective mass calculation and the full pseudopotential calculation is excellent. Whereas for the second state, labelled LH1, the agreement is less good there is still a strong correlation between the two calculations. To understand why the second state is not as well described by the simpler calculation as the heavy hole states it is necessary to return to the bulk bandstructure and to consider the variation of the heavy and light holes with energy. It is found from calculations on the bulk that the heavy hole band is parabolic and can be well described by one parameter – the effective mass – in a given direction. The light hole, on the other hand, should be
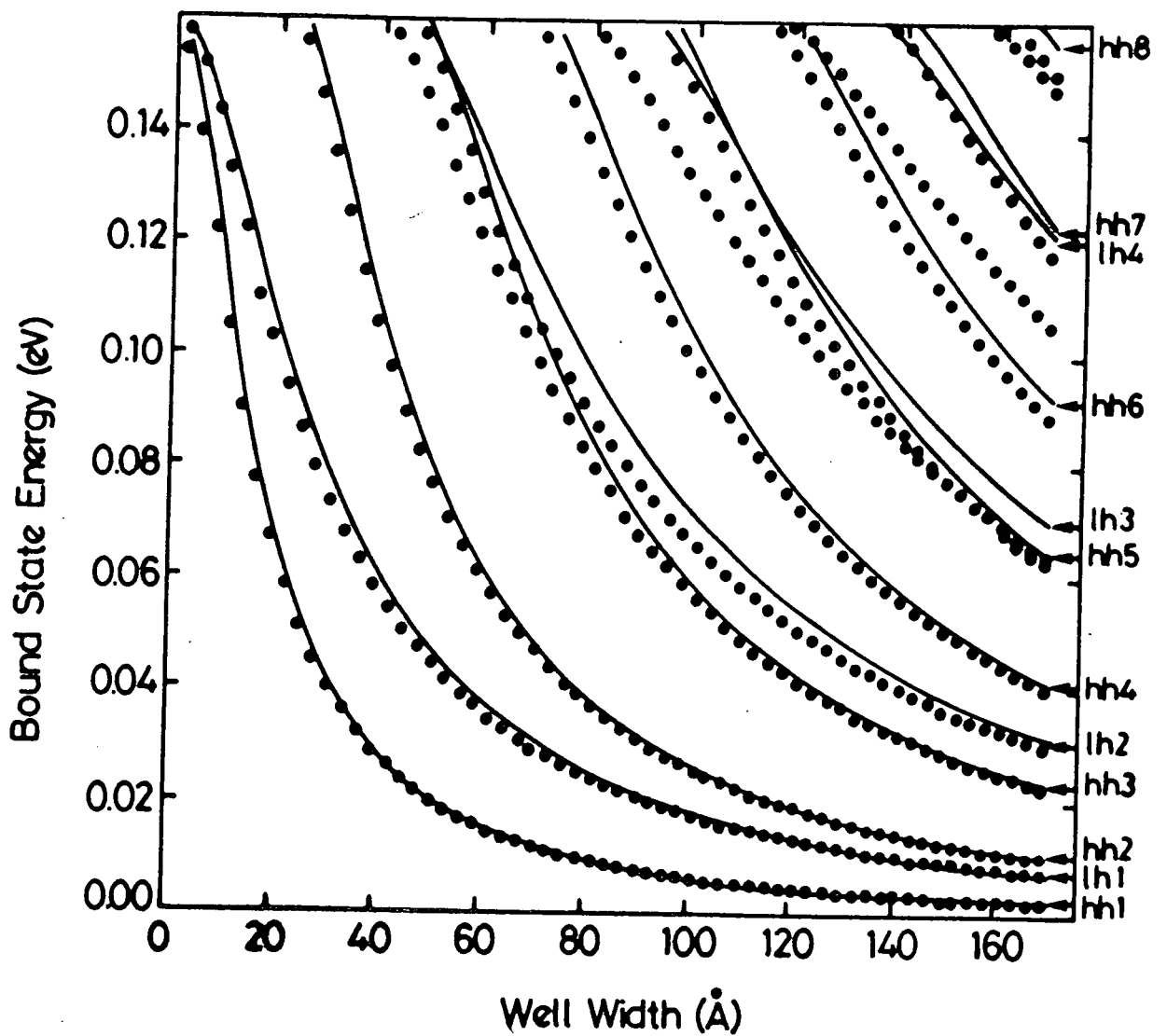
Figure (4.8)   Full circles: the calculated bound-state energies of the $Al_{0.3}Ga_{0.7}As/GaAs/Al_{0.3}Ga_{0.7}As$ quantum well using the pseudopotential complex-band-structure approach. Full curves: heavy- and light- results are calculated from a simple position-dependent effective-mass approach. The labelling on the right-hand side refers to the effective-mass results.
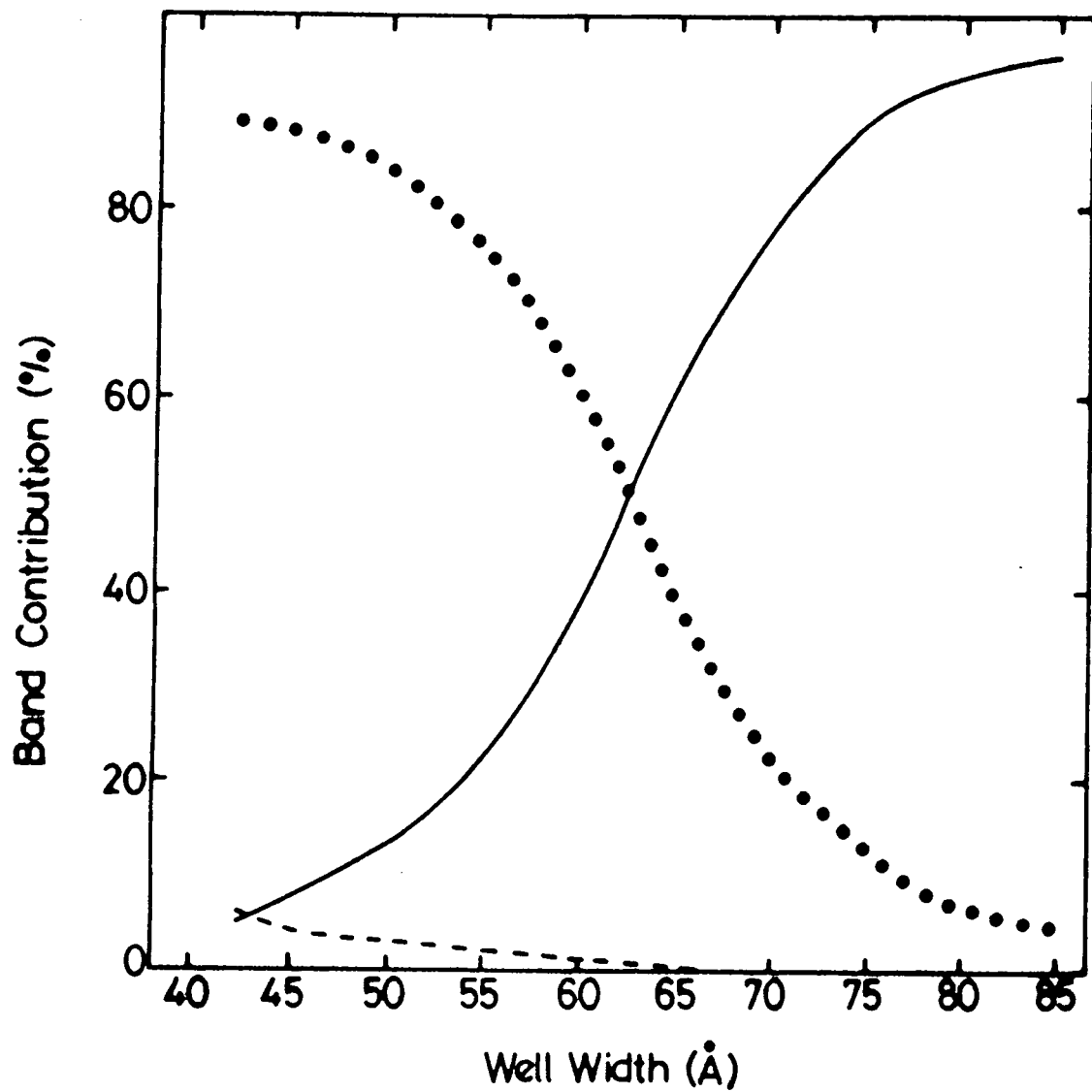
Figure (4.9)   The heavy (full curve), light (dotted curve) and spin-split-off
(broken curve) band contributions to the fourth-bound-state solution shown in
figure (4.7) .

thought of as having a varying effective mass which for energies away from the Γ-point approach that of the heavy hole. Consequently, for the lower heavy hole states – certainly up to HH4 – the agreement between the simple and full calculation is very good. For LH1, however, although there is a good fit for low energies, corresponding to the region of the bandstructure which is accurately modelled by the effective mass and for very small widths where **any** solution will be pushed towards the top of the well, the fit is less good between.

It has been shown (Inkson, 1986) for the conduction band that by using a non-parabolic effective mass theory (Bastard, 1985) that this problem can be improved upon to a certain extent. Nevertheless, the process necessary to effect this improvement is fairly complicated and still would not give a description of anti-crossing effects.

Anti-crossing effects can, in fact, be seen in figure (4.8). In particular we shall consider the interaction which can be seen between the fourth and fifth states – which are labelled as LH2 and HH3 in the effective mass notation. Results for the effective mass HH3 state agree well with the pseudopotential results above a quantum well width of 80Å for the fourth bound state but at smaller widths the agreement is better with the results of the fifth bound state.

This is due to a HH3-LH2 anti-crossing effect centred just above a width of 60Å. Figure (4.9) shows clearly the variation in heavy and light hole contributions from a width of about 40Å – the width at which the

fourth bound state appears in the well – and 85Å at which point the heavy

hole contribution has risen to more than 95%.

Below 60Å the solutions are clearly dominated by a light hole band

component for the fourth bound state. We have found that the fifth bound

state has a corresponding preponderance of heavy hole in this region which

falls rapidly at widths beyond 60Å where the light hole contribution increases.

This explains why the effective mass model works well for the fifth bound

state at smaller widths and for the fourth bound states at larger widths.

In figure (4.10) it is possible to see the development of the charge

density plotted along a line perpendicular to the interface planes and through

the bond centres for the fourth pseudopotential bound state as the well

width is altered. The three plots shown are for 30, 22 and 16 monolayers

corresponding to 84.8, 62.2 and 45.2Å of GaAs respectively. For a well width

of 84.8Å the HH3-like envelope structure is visible with two clearly observable

nodes with a slight asymmetry due to a small amount of LH2 mixing which

contributes about 5% to the wavefunction as can be seen from figure (4.9).

For the narrowest well, of figure (4.10.c) we have something which can be

recognised as a first excited state, corresponding to a wavefunction which is

dominated by a LH2-like component. However, the charge density is strongly

asymmetric due to a mixing of almost 10% from the HH3 component. We

also note that due to the proximity of the barrier edge and the narrowness

of the well there is quite considerable penetration of the wavefunction into

the barrier region. For the charge density plot corresponding to a width of
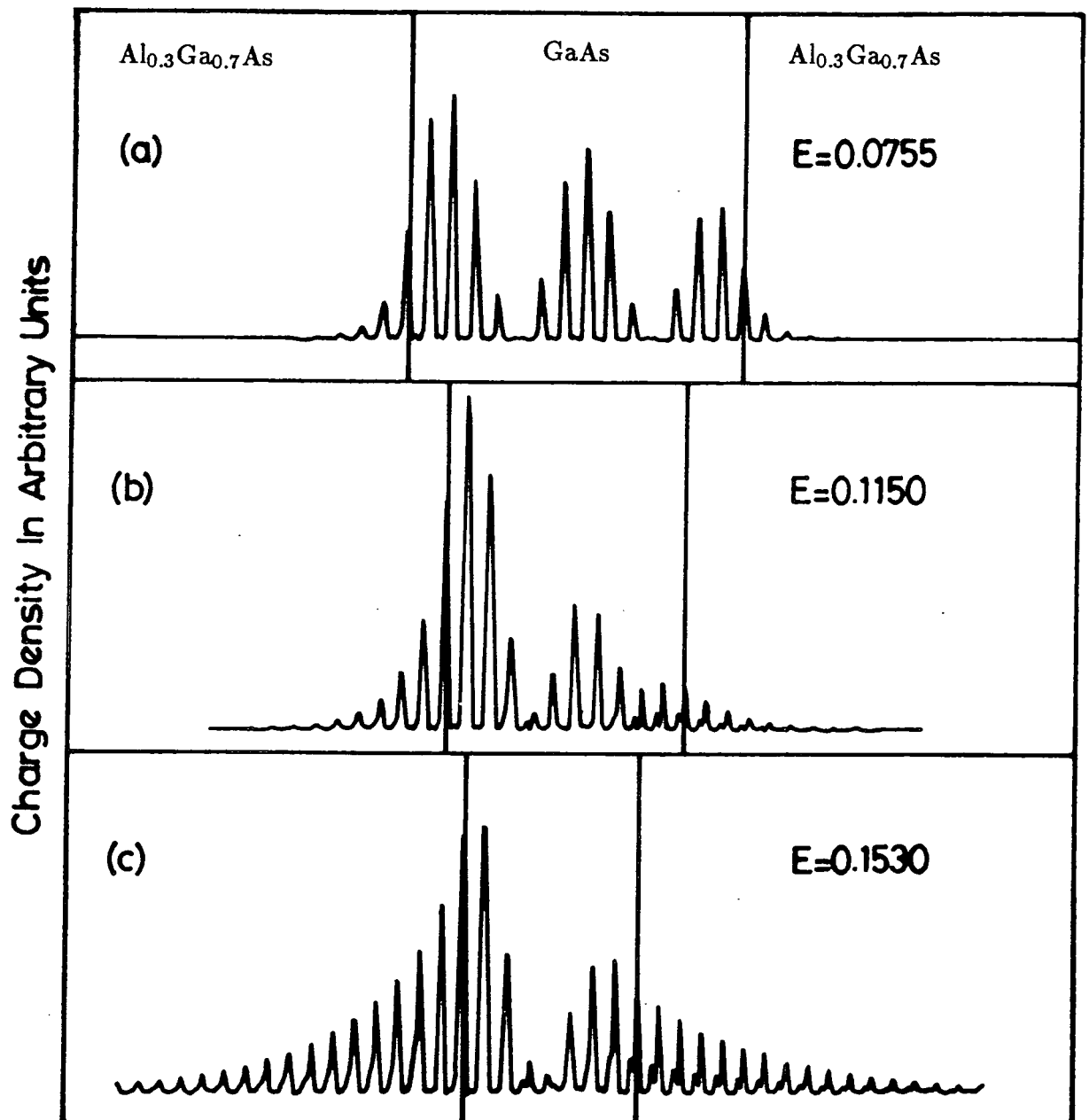
Figure (4.10) The charge density of the fourth-bound-state solution of the
$Al_{0.3}Ga_{0.7}As/GaAs/Al_{0.3}Ga_{0.7}As$ quantum well at widths of
(a) 84.8, (b) 62.2 and (c) 45.2 Å.   The charge density is plotted along a
line perpendicular to the interface planes passing through the bond centres.
E=(a) 0.0755, (b) 0.1150 and (c) 0.1530eV.

62.2Å in figure (4.10.b) we have almost equal amounts of LH2- and HH3-like contribution and the charge density does not have a distinct overall envelope.

Discussion.

The idea of finding hybridisation and anti-crossing effects in the (100) direction has been put forward before (Chung Chang and Schulman, 1985) for an alloy superlattice but using a 85:15 offset which tended to make the effects occur for relatively wide well regions, and these workers tended to concentrate their efforts on investigating in-plane bandstructure interactions and their effect on optical matrix elements. In-plane properties have also been studied by others (O'Reilly and Witchlow, 1987) with reference to the effects of strain and quantum confinement on effective masses.

The fact that mixing can occur even for states with no in-plane component of crystal momentum may have serious effects when one considers the tunnelling of holes through narrow barriers (Monaghan and Brand, 1988) where a heavy hole can be sent in to a device or low dimensional structure and emerge with a considerable percentage of light or spin-split-off component.

From an experimental viewpoint, however, a more direct implication of the existence of the mixing that occurs in the anti-crossing regions described above is that additional structure may occur for optical spectra of quantum wells. Normally allowed transitions are of the type HHn-En or LHn-En where E represents conduction band states. In addition, it is sometimes possible to observe other 'less favourable' transitions of the form HH3-E1 (Miller et al, 1982) for excitation spectra of multiquantum wells.

But for widths of about 62.2Å we have seen that both the fourth and fifth bound states have a considerable LH2 component, so that both may participate in transitions which involve LH2-E2 couplings. Since the separation between the fourth and fifth bound states at this width is of the order of 6meV this phenomenon should be observable with current experimental techniques. In fact these extra peaks have been put forward as an explanation (Ninno et al, 1986) of transition energies obtained in experiments on GaAs–AlGaAs quantum wells (Dawson et al, 1985).

This finishes our investigations of AlGaAs systems. We have shown that although these materials have received a great deal of theoretical and experimental investigation even for the most straightforward case of a quantum well with no in-plane crystal momentum unusual effects can occur. In particular the idea of wavefunctions which are asymmetric – rather than antisymmetric – even though the 'effective mass' Hamiltonian appears symmetric; and the possibility of optical doublets forming due to hybridisation are concepts which can be thought of as basic to any understanding of low dimensional structures.

In the following two chapters we shall move on to the investigation of silicon and germanium where the complications of strain will be encountered and solved but again consideration of simple cases will produce interesting physics.

CHAPTER FIVE

THE COMPLEX BANDSTRUCTURE MATCHING TECHNIQUE
AND ITS APPLICATION TO STRAINED MATERIALS

The preceding two chapters have dealt, in some detail, with energy states and wavefunctions of III–V quantum wells and superlattices. We now wish to consider similar physical properties of low dimensional structures composed of silicon and germanium. These elements seem, at first sight, to be rather simpler in nature than the III–V binaries. In the bulk silicon and germanium crystallise in the diamond structure. The main complication with these group IV materials is that they are both indirect (for the unstrained materials germanium has its minimum at (111) and that of silicon is in the (100) direction).

Since both materials are indirect it seems that it is impossible to produce optical components from Si/Ge technology. This is unfortunate since it is desirable to make Si/Ge optical components which are contiguous parts of larger opto-electronic devices. Also the fact that many years of intellectual work and a great deal of finance have been invested in Si/Ge growth has made researchers loath to give up the hope of producing direct Si/Ge type materials.
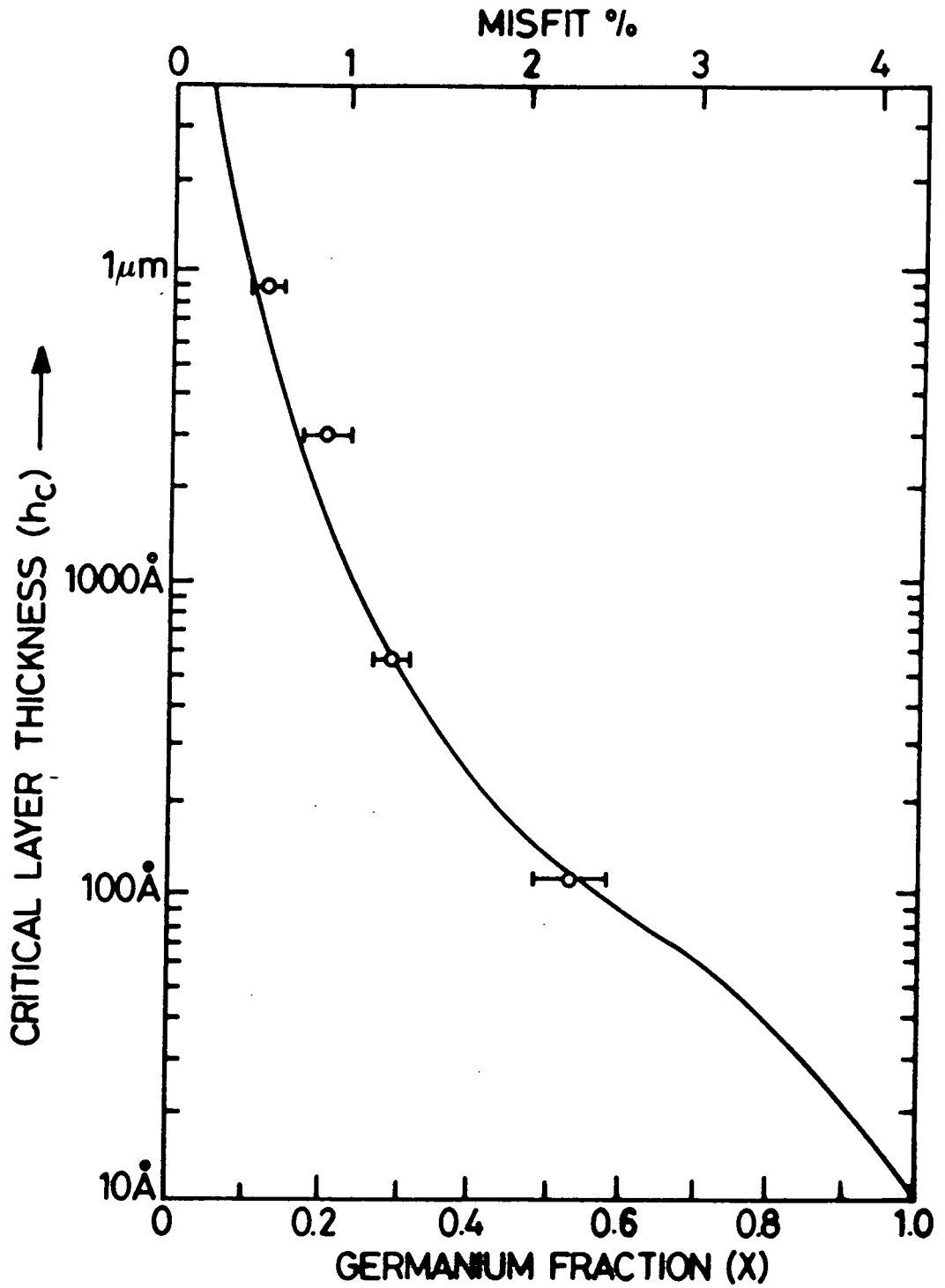
Figure (5.1)   Width of maximum epilayer for Ge_xSi_{1-x} alloy grown on Si(100) substrate.   The solid line shows the theoretical fit as given by equation (5.1).   The error bars are results obtained from experiment (Bean et al, 1984).

With the advent of low dimensional technology the possibility of producing superlattices by the processes of M.B.E. and M.O.C.V.D. meant that it might be possible to use the techniques of bandgap engineering and the effects of zone-folding to make a device with a direct principal gap. Initial progress was slow, however, since silicon and germanium have a large lattice mismatch (differing by about 4%). But eventually it became clear that it was possible to grow strained-layer superlattices which were, in effect, free of dislocations, in certain conditions – which we shall now discuss.

Critical Epilayer Size.

It is necessary to consider the limits of pseudomorphically grown low dimensional structures to find out what sort of constraints are imposed on practical device design. It is well known that if the misfit between a substrate and a growing epilayer is sufficiently small the first atomic layers which are deposited are strained so that the in-plane lattice constant of the grown layer matches that of the unstrained substrate lattice constant and hence a coherent interface is formed. Beyond a certain width, however, the quality of the interface is degraded with dislocations forming – it being energetically favourable over the increasing amount of strain-energy within the material. A great deal of theoretical work has been carried out to calculate what the maximum width of epilayer is for a Ge_xSi_{1-x} epilayer grown on a silicon substrate as a function of germanium content 'x' (People, 1986). The best calculations seem to indicate a variation in the critical

thickness of the form:

$$h_c \propto \frac{1}{f^2}$$

where f is the misfit between the substrate and the epilayer. Figure (5.1) shows the detailed variation which is described by the equation (People and Bean, 1985):

$$h_c = \left(\frac{1-\nu}{1+\nu}\right)\left(\frac{1}{20\pi\sqrt{2}}\right)\left[\frac{b^2}{a(x)}\right]\left[\frac{1}{f^2}ln\left(\frac{h_c}{b}\right)\right] \qquad 5.1$$

where ν is the Poisson ratio of the strained material, b is the magnitude of the Burger's vector and $a(x)$ is the mean bulk lattice constant of the Ge_xSi_{1-x}. We notice that the critical layer thickness, h_c, approaches infinity as the germanium content falls towards zero, as we would expect. It is also important to notice that in the most extreme case, of pure germanium on a silicon substrate, the largest supportable epilayer width is approximately 10Å.

Of course, if more complicated structures, such as superlattices and multiple quantum wells, are to be grown then the question arises: what happens when many different layers are grown on top of each other? It has been shown that equation (5.1) can still be used if the following method is employed: the critical thickness for a system of coherently strained multilayers is identical to the critical thickness for a single coherently strained layer of thickness equal to the total thickness of the multilayers and germanium content equal to the spacially averaged Ge content over a single period of the multilayers (Hull et al, 1986).
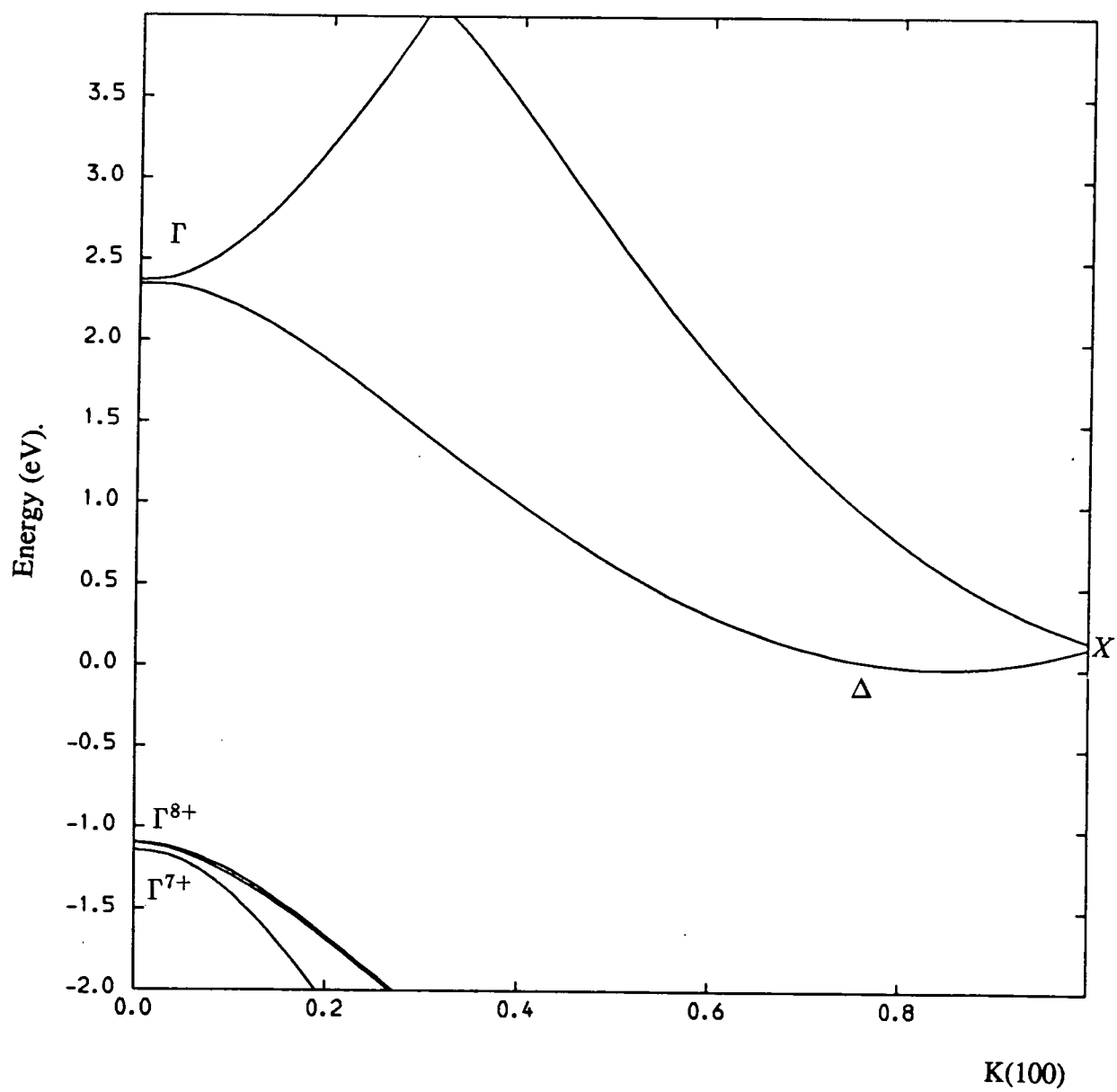
Figure (5.2)   Bandstructure of unstrained bulk silicon using the
pseudopotential formfactors given in the text.
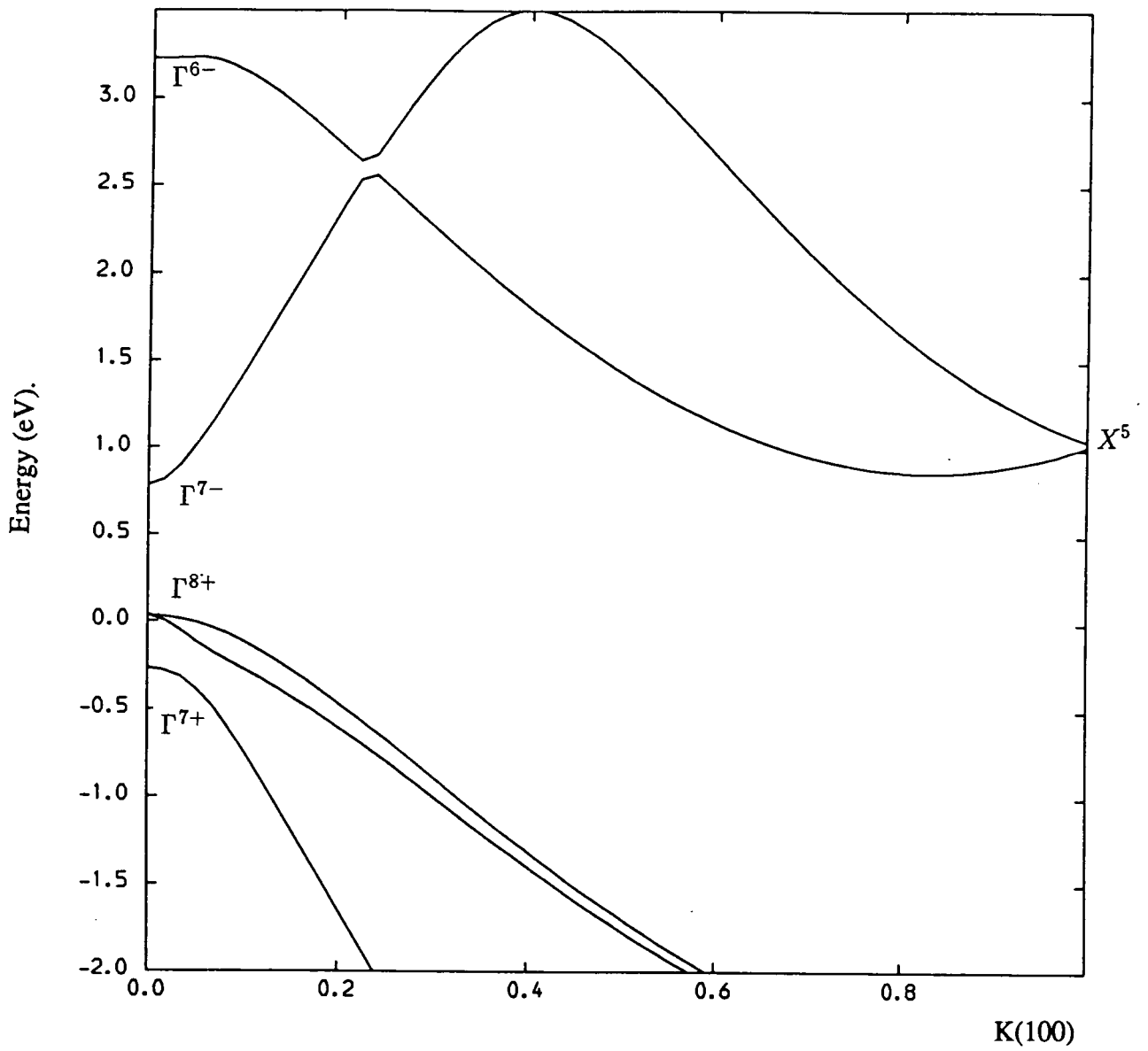
Figure (5.3) Bandstructure of unstrained bulk germanium using
the pseudopotential formfactors given in the text.

The Effects of Strain.

Before going on to consider how the effects of strain can be introduced into the complex bandstructure matching technique and the pseudopotential model which we use, it will be informative, as an introduction, to make a qualitative investigation of the effects of both uniaxial and hydrostatic pressure, as observed experimentally for a bulk group IV material. For simplicity we shall consider Si – although similar effects occur for germanium or $Ge_x Si_{1-x}$ alloys.

The bandstructure of silicon is shown in figure (5.2) (for completeness figure (5.3) shows germanium bandstructure with some of the symmetry designations appropriate to the investigation of germanium which occurs later). As has been mentioned silicon is indirect with a conduction band minimum in the (100) direction approximately 85% of the way to the zone edge. In the bulk material, therefore, silicon has six equivalent minima. On the application of hydrostatic pressure the lattice constant of the crystal decreases but the overall symmetry remains the same. Consequently any degenerate states remain degenerate on the application of hydrostatic pressure but the size of energy gaps may alter. For instance the principal, indirect, energy gap decreases – for reasons which will be given later – while in contrast the size of the large direct bandgap increases.

If, on the other hand, uniaxial strain is applied the case is very different. If silicon is grown on a material of a larger lattice constant (such as germanium), as has been indicated, up to a certain layer width the silicon

will take up the lattice constant determined by the Poisson ratio of the material such that:

$$\Delta a_\parallel = \Delta a_\perp \left[\frac{-2\nu}{1 - \nu} \right]$$

5.2

where

ν is the one dimensional Poisson ratio.

$\Delta a_\parallel$ is the change in lattice constant in growth direction.

$\Delta a_\perp$ is the change in lattice constant perpendicular to growth direction. i.e.

$\Delta a_\perp$ = (lattice constant of unstrained Si — lattice constant of substrate).

This effect does **not** retain the symmetry of the material as in the hydrostatic case, and consequently lifts certain degeneracies in the bandstructure. Only two of these lifted degeneracies will concern us here. The heavy-hole and light-hole degeneracy is lifted at $k = 0$ and will be discussed quantitatively later in this chapter. The sixfold degeneracy of the conduction band minima is also lifted. In the case of silicon being grown on a substrate of larger lattice constant the minima will split into a twofold degenerate state which **falls** in energy with respect to the top of the valence band and a fourfold degeneracy which **rises** in energy with respect to the top of the valence band.

Theory.

The approach to be taken in the modelling of strain in the present work is empirical in nature. Some early workers tried to model the effects

of strain by using a purely theoretical representation of the pseudopotential curve for silicon (Goroff and Kleinman, 1963) and for germanium (Bassani and Brust, 1963) but only met with partial success. The inclusion of strain effects for the plane-wave pseudopotential method which we use will be shown to be easy to carry out. The theoretical discussion which follows will ignore spin although this is easily included in the calculation – as has actually been done for the fits of bandstructure later in the chapter.

Although pseudopotentials have been used in previous chapters they have been treated as parameters obtained from fits to experiment. Since in the work that follows a certain amount of mathematical manipulation of pseudopotentials is carried out it is necessary to consider them in their more abstract form.

Beginning with the pseudopotential form of the one-electron Hamiltonian:

$$\mathbf{H} = \frac{p^2}{2m} + V_p(\mathbf{r}) \qquad\qquad 5.3$$

where $V_p(\mathbf{r})$ is the pseudopotential which has replaced the real potential of the crystal in such a way as to give the same eigenvalues as the real potential but has removed the deep core potentials which can cause convergence problems when calculating bandstructure. In the 'local' pseudopotential method we assume that $V_p(\mathbf{r})$ is only a function of position and here we further assume has spherical symmetry. It can be written as:

$$V_p(\mathbf{r}) = \sum_{\mathbf{G}} S(\mathbf{G}) V_p(\mathbf{G}) e^{i\mathbf{G}\cdot\mathbf{r}}$$

where the sum includes only a few values of **G**'s. For silicon and germanium the terms can be written as

$$V_p(\mathbf{G}) = V(\mathbf{G})/\Omega_0 \qquad\qquad 5.4$$

and

$$S(\mathbf{G}) = \sin \mathbf{G}.\tau \qquad\qquad 5.5$$

where $V(\mathbf{G})$ is the atomic pseudopotential form factor,

Ω_0 is the atomic volume,

$S(\mathbf{G})$ is the structure factor,

$\tau = \frac{a}{8}(1,1,1)$,

and a is the bulk lattice constant.

Hydrostatic pressure: Theory.

If we have an energy eigenstate of energy E for the Hamiltonian (5.3) it will be of the form

$$\psi_E = \sum_{\mathbf{G}} a_{\mathbf{G}} \exp i(\mathbf{k} + \mathbf{G}).\mathbf{r}. \qquad\qquad 5.6$$

But how will the energy of this state vary with the variation of the volume when hydrostatic pressure is applied? From elementary quantum mechanics:

$$\frac{\partial E}{\partial \Omega} = \frac{\partial \langle \psi_E | \mathbf{H} | \psi_E \rangle}{\partial \Omega} \qquad\qquad 5.7$$

which, after substituting (5.6), gives

$$\Omega \frac{\partial E}{\partial \Omega} = -\frac{2}{3} \sum_{\mathbf{G}} \frac{|\mathbf{k} + \mathbf{G}|^2}{2m} a_{\mathbf{G}}^* a_{\mathbf{G}} + \sum_{\mathbf{G}} \sum_{\mathbf{G}'} a_{\mathbf{G}}^* a_{\mathbf{G}+\mathbf{G}'} S(\mathbf{G}) \frac{\partial V_p(\mathbf{G})}{\partial \Omega} \Omega$$

or,

$$\Omega\frac{\partial E}{\partial\Omega} = -\frac{2}{3}(\text{`kinetic energy'}) + \sum_{\mathbf{G}} S(\mathbf{G})\rho(\mathbf{G})\frac{\partial V_p(\mathbf{G})}{\partial\Omega}\Omega$$

where $\rho(\mathbf{G})$ is the Fourier component of the charge density associated with the reciprocal lattice vector $\mathbf{G}$ and fundamental constants have been set to unity to simplify the form. From equation (5.4)

$$\frac{\partial V_p(\mathbf{G})}{\partial\Omega} = \frac{\partial}{\partial\Omega}\left(\frac{V(\mathbf{G})}{\Omega}\right)$$

or,

$$\frac{\partial V_p(\mathbf{G})}{\partial\Omega} = -\frac{V(\mathbf{G})}{\Omega^2} - \frac{|\mathbf{G}|}{3\Omega^2}\left(\frac{\partial V(\mathbf{G})}{\partial|\mathbf{G}|}\right) \qquad 5.8$$

So, the variation in the energy with volume can be broken into two parts, one due to the kinetic energy:

$$\Omega\frac{\partial E^{kin}}{\partial\Omega} = -\frac{2}{3}E^{kin}$$

and a term due to the variation in the (pseudo)potential:

$$\Omega^2\frac{\partial E^V}{\partial\Omega} = -\sum_{\mathbf{G}} S(\mathbf{G})\rho(\mathbf{G})\left(V + \frac{1}{3}|\mathbf{G}|\frac{\partial V}{\partial|\mathbf{G}|}\right).$$

In certain circumstances these terms may be of the same sign whilst at other times they may compete and consequently some gaps get bigger while others get smaller on the application of pressure. It has been shown in the literature (Martinez, 1980) that the s-levels have a stronger deformation potential than p-levels. Consequently we can expect the direct gap of silicon to increase with application of hydrostatic pressure. The indirect gap however involves two predominantly p-like states and this gap may be

expected to vary slowly with increasing pressure. The sign of the variation, however, cannot be predicted by simple analytic considerations and has been shown to be heavily influenced by d-states at high energies in the bandstructure (Lee et al, 1985).

Uniaxial Pressure.

The case for uniaxial pressure is complicated by the fact that the lattice constants of the cubic material are changed by different amounts in different directions. For this reason, and to give a more pragmatic example of the inclusion of strain, we shall limit ourselves to consideration of the Hamiltonian matrix as described in Appendix A. Without spin or strain:

$$\mathbf{H}_{\mathbf{G},\mathbf{G}'} = \left(\frac{(\mathbf{k}+\mathbf{G})^2}{2m} - E\right)\delta_{\mathbf{G},\mathbf{G}'} + V_p(|\mathbf{G}-\mathbf{G}'|)S(|\mathbf{G}-\mathbf{G}'|) \qquad 5.9$$

(Chelikowsky and Cohen, 1976). However, with the inclusion of strain, such that the lattice constants for the y and z directions are changed by equal amounts and the lattice constant in the x direction is altered in accordance with equation (5.2), equation (5.9) becomes

$$\mathbf{H}_{\mathbf{G},\mathbf{G}'} = \left(\frac{A^2}{b^2}\frac{(k+G)_x^2}{2m} + \frac{A^2}{a^2}\frac{(k+G)_y^2}{2m} + \frac{A^2}{a^2}\frac{(k+G)_z^2}{2m} - E\right)\delta_{\mathbf{G},\mathbf{G}'}$$

$$+ V_p(|\mathbf{G}-\mathbf{G}'|)S(|\mathbf{G}-\mathbf{G}'|)$$

where A is the unstrained lattice constant,

b is the new lattice constant in the x-direction,

a is the new lattice direction in the y and z-directions.
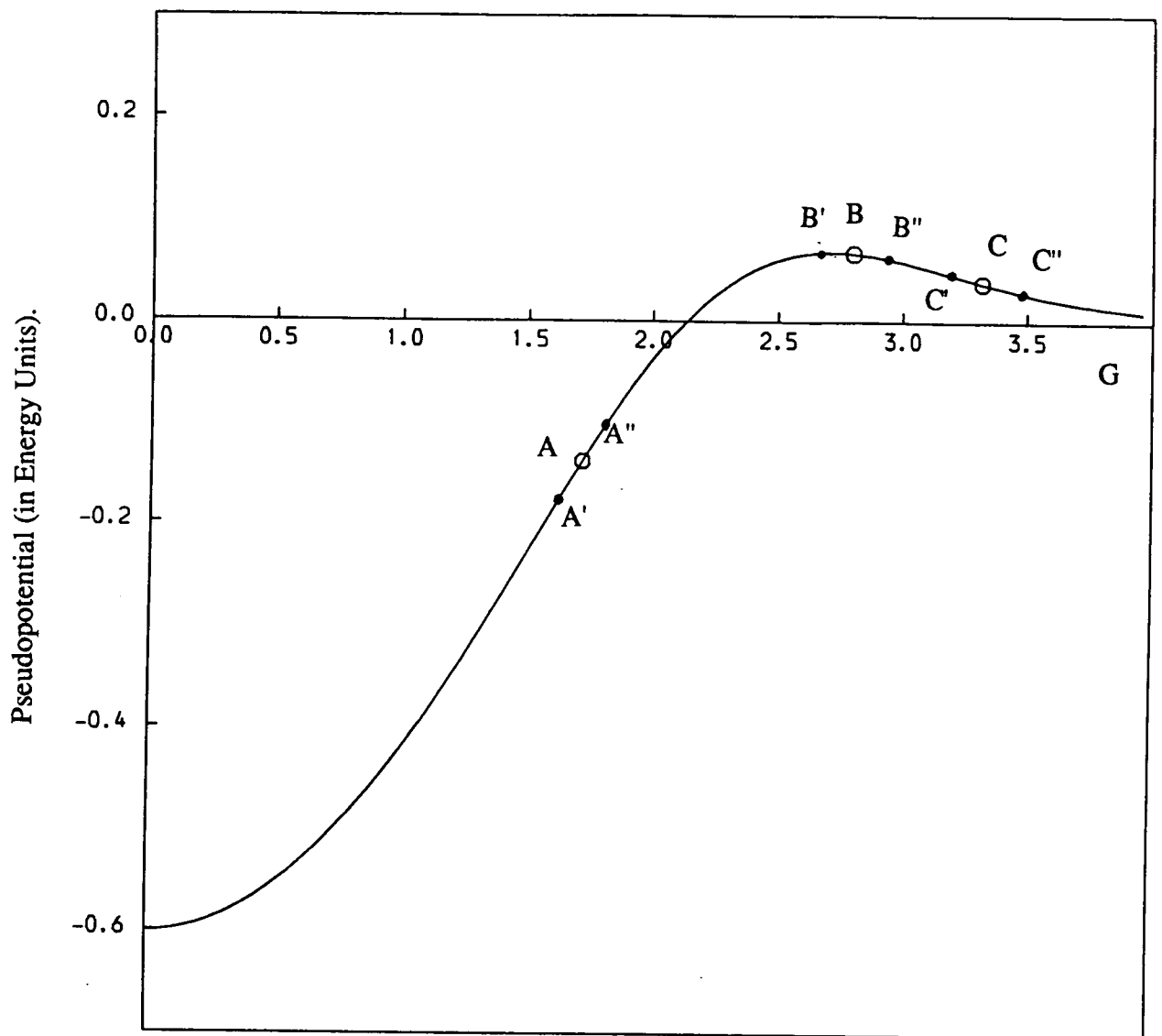
Figure (5.4)   A typical form for a pseudopotential curve
   describing the asymmetric pseudopotentials . The points
   A, B and C represent G^2 =3, 8 and 11. The points A, A'
   A", B', B",C' and C" represent values of G^2 relevant to
   strained materials, as explained in the text.

It is necessary to consider the variation of $V_p(|\mathbf{G} - \mathbf{G}'|)S(|\mathbf{G} - \mathbf{G}'|)$. with the application of uniaxial pressure where we have, from equation (5.4),

$$V_p(\mathbf{G})S(\mathbf{G}) = \frac{V(\mathbf{G})S(\mathbf{G})}{\Omega}$$

First we may consider the nature of the structure factor and how it varies. We have that

$$S(\mathbf{G}) = \sin \mathbf{G}.\tau.$$

When strained the reciprocal lattice vectors are of the form

$$\mathbf{G} = \frac{2\pi}{V}(a^2 h, bai, baj) \qquad 5.10$$

with h, i, j as integers such that all are even or odd.

V is the volume of the strained unit cell, and

$\tau = \frac{1}{8}(b, a, a)$

Therefore $\mathbf{G}.\tau = \frac{\pi}{4}(h+i+j)$ as for the unstrained case. Consequently the structure factor is invariant with respect to uniaxial pressure (and so with respect to hydrostatic pressure – a fact which was used earlier). The factor Ω is just $a^2 b$ since the material now has a tetragonally distorted unit cell.

But what adjustments must be made to $V(\mathbf{G})$? Equation (5.10) indicates that

$$|\mathbf{G}| = \frac{2\pi}{ab}(a^2 h^2 + b^2 i^2 + b^2 j^2)^{\frac{1}{2}} \qquad 5.11$$

which can be calculated for all values of i, j, h such that all are even or odd. Figure (5.4) shows a typical pseudopotential curve appropriate to

symmetric form factors. The points A, B, C represent the pseudopotential formfactors to be used for an unstrained material at $G^2 = 3, 8, 11$. A', A'', B', B'', C', and C'', show the points at which $V(G)$ must be calculated if strain is introduced.

Consequently in order to calculate the appropriate pseudopotential formfactor for the strained system it is necessary to calculate the new value of $|G|$ by using equation (5.11) and then reading the value of $V(G)$ from figure (5.4). In practice, of course, the exact form of the $V(G)$ curve is not known. To overcome this problem the curve is assumed to be linear around and close to the points A, B and C. This means that the pseudopotential curve for silicon and germanium can be described by six parameters each: three to describe the unstrained material's pseudopotential formfactors and three to describe the gradient at $G^2 = 3, 8, 11$. The justification for simplifying the curve to, in effect, three straight lines is that the variation in the size of the reciprocal lattice vectors will be small (<4%). Also, as will be seen later, the method gives good agreement with experiment over a wide range of physical conditions.

Fitting the Bandstructure.

As has been stated; in order to calculate the appropriate pseudopotential formfactors for the strained system it is necessary first to fit the bulk bandstructure to experimental results. The three gradients, on the other hand, are calculated by finding the best fits to experimental hydrostatic pressure results. Since it is hoped to calculate matrix elements between

conduction and valence band states it was decided to use the same number of plane waves in both sets of bands. To ensure good convergence in the conduction band a relatively large number of plane waves, actually 65, were used. And, although it introduced a considerable increase in computing time, the effects of spin orbit splitting were included in both the conduction and valence bands.

The fitting of the pseudopotentials must be carried out in such a way as to fulfil many constraints with respect to the overall bandstructure. Most calculations involving the bandstructure will be limited to the (100) symmetry directions and will deal with the lowest direct and secondary gaps. But the fitting has been made generally usable in a wide range of k-directions so that later work can concentrate on 'optical' and transport related phenomena. In the following fits for both materials all results are for T=300K where experimental results are available. In cases where only low temperature experimental results are available the highest temperature result is taken. All results, unless otherwise indicated, are in electron volts. The actual values for the formfactors and formfactor 'gradients' are given in Appendix C.

Silicon Bandgaps.

We begin with the main bandgaps for bulk unstrained silicon. The gaps are given in terms of the symmetry of the two participating states as denoted by figure (5.2). So that, for instance, $\Gamma - \Gamma$ denotes the smallest direct gap in silicon.

	Calculated	Experiment
$\Gamma - \Gamma$	3.44	3.48[a]
$\Gamma - \Delta$	1.11	1.11[b]
$L_3 - L_1$	3.37	3.48[a]
SSO	45meV	44meV[c]

(a) Sari and Schnatterly, 1973.

(b) Welber et al., 1975.

(c) Zwerdling et al., 1960.

The large direct gap of silicon means that the only gap of real importance in the present work is the (100) minimum which is fitted to two decimal places. The Δ-minimum is found experimentally to be 85% of the way towards the zone edge (Feher, 1959). and this agrees with the calculated result. It should be mentioned here that an 'unphysical' bandgap of about 35meV appears at the X-point for the lowest conduction-band due to using a finite number of plane-waves (a similar gap appears in Ge). There is no simple method of removing this inherent problem but it causes no problems away from this 'pseudobandgap'.

Silicon Effective Masses.

In some respects the effective masses may be considered to be the most important parameters. Consequently special consideration is made for this particular fit.

	Calculated	Experiment
$\Delta_\perp$	0.19	$0.19^{(a)}$
$\Delta_\parallel$	0.90	$0.92^{(a)}$
HH	0.30	$0.54^{(b)}$
LH	0.19	$0.15^{(b)}$
SO	0.22	$0.23^{(b)}$

(a) Hensel et al., 1965.

(b) Barber, 1967.

The silicon effective masses are seen to agree with experiment to within a few per cent with the exception of the heavy hole band mass; which is calculated to be much less than is actually observed in experiment. The relative importance of this error depends on the actual offsets of the structure being investigated. As will be discussed later (Chapter 6) the valence band offset between a germanium alloy and silicon is always such that silicon will form the barrier region. Consequently, since the barrier effective mass has little bearing on the low dimensional energy bonding states the error in the heavy-hole mass should produce little error in calculated energy solutions of a superlattice or quantum well.

It is worth noticing that both the longitudinal and transverse effective masses of the lowest lying conduction-band state have been fitted exactly. It is these states which will play the biggest part in the following work by forming the well-states in the conduction band.

Germanium Bandgaps.

	Calculated	Experiment
$\Gamma - L$	0.66	$0.66^{(a)}$
$\Gamma - \Gamma$	0.77	$0.79^{(b)}$
$\Gamma - \Delta$	0.84	$0.87^{(c)}$
SSO	0.30	$0.29^{(d)}$

(a) Macfarlane et al., 1957.

(b) Aspnes, 1973.

(c) Braunstein et al., 1958.

(d) Kane, 1956.

In germanium the Δ, Γ and L gaps all lie within 0.4eV of each other and so an effort must be made to fit them all as accurately as possible. The $\Gamma - L$ bandgap is the smallest which has been fitted to two decimal places. The direct gap is difficult to measure but is generally taken to be 0.795eV at 300K. The position of the Δ-minimum is open to even more uncertainty and any comparison between experiment and calculation should be given little weighting. For germanium the spin split-off separation is large (0.3eV as compared to only 0.044eV for silicon) and is fitted to within five per cent.

Germanium Effective Masses.

	Calculated	Experiment
L_6^-	0.072	$0.081^{(a)}$
Γ_7^-	0.053	$0.042^{(b)}$
HH	0.33	$0.29^{(c)}$
LH	0.035	$0.043^{(c)}$
SO	0.10	$0.09^{(b)}$

(a) Fink and Braunstein, 1976.

(b) Groves, 1966.

(c) Dexter et al., 1956.

All calculated masses seem to be in good agreement with experiment. As has been noted earlier due to the large valence offset of Si/Ge (highest valence band of Ge lies 0.84ev above highest for Si (Van de Walle and Martin, 1986)) the valence band effective masses tend to be more important since Ge tends to form the well regions for holes.

Hydrostatic Pressure.

As has been explained elsewhere the effects of hydrostatic pressure are introduced into the pseudopotential model independently by fitting three parameters to give the correct response of energy gaps with varying lattice constants. This section will aim to give an indication of how hydrostatic pressure effects have been modelled by a purely empirical fit. To simplify matters but without decreasing the overall accuracy of the calculation a small hydrostatic pressure is assumed to be applied to a sample of the material. It is necessary to know the change in lattice constant of the

material with this small pressure. Starting with Murnaghan's equation (Murnaghan, 1944):

$$P = \left(\frac{B_0}{B_0{}'}\right)\left[\left(\frac{a_0}{a}\right)^{3B_0{}'} - 1\right]$$

where

B_0 = Bulk Modulus.

$B_0{}'$ = Derivative of Bulk Modulus with pressure.

a_0 = Unstrained lattice constant.

a = Strained lattice constant.

P = Exerted pressure.

But for the small lattice constant changes considered here, typically 1.0% for the fitting,

$$\frac{a_0}{a} = \frac{a_0}{a_0 + \delta a}$$

$$P \approx -\left(\frac{B_0}{B_0{}'}\right)\left[3B_0{}'\frac{\delta a}{a}\right]$$

$$P = -\frac{\delta V}{V}B_0$$

This method of fitting to a small external force has the advantage of not employing the pressure derivative of the Bulk Modulus which is not accurately known. Consequently for the following comparisons changes in linear lattice constants of approximately one per cent are considered. The values given will be for the change in bandgap in electron-volts unless otherwise indicated.

Silicon Band Gaps: Effect of Hydrostatic Pressure.

	Calculated	Experiment
$\Gamma - \Gamma$	−0.050	+0.085[a]
$\Gamma - \Delta$	−0.039	−0.041[b]
$L_3 - L_1$	+0.138	+0.15[b]

(a) Welber et al., 1975.

(b) Zallen and Paul, 1967.

The variation of the $\Gamma - \Delta$ and $L_3 - L_1$ gaps with pressure can be seen to be fitted very well. The direct gap, unfortunately, moves in the wrong direction. This result is not expected to have any bearing on most calculations since the rate of change is very slow and the gap starts off very large, well away from the main region of interest: the rapidly falling Δ-minimum.

Germanium Band Gaps: Effects of Hydrostatic Pressure.

	Calculated	Experiment
$\Gamma - \Gamma$	+0.30	+0.34[a]
$\Gamma - L$	+0.113	+0.115[a]
$\Gamma - \Delta$	−0.002	slightly −ve[a]

(a) Welber et al., 1977.

These fitted variations are also in good agreement with experiment. It is worth noting that the direct bandgap's calculated rise is rather slower than is found in experiment. This may well lead to difficulties when the ordering of low dimensional X and Γ levels may depend critically on the exact positions of the strained bulk levels.
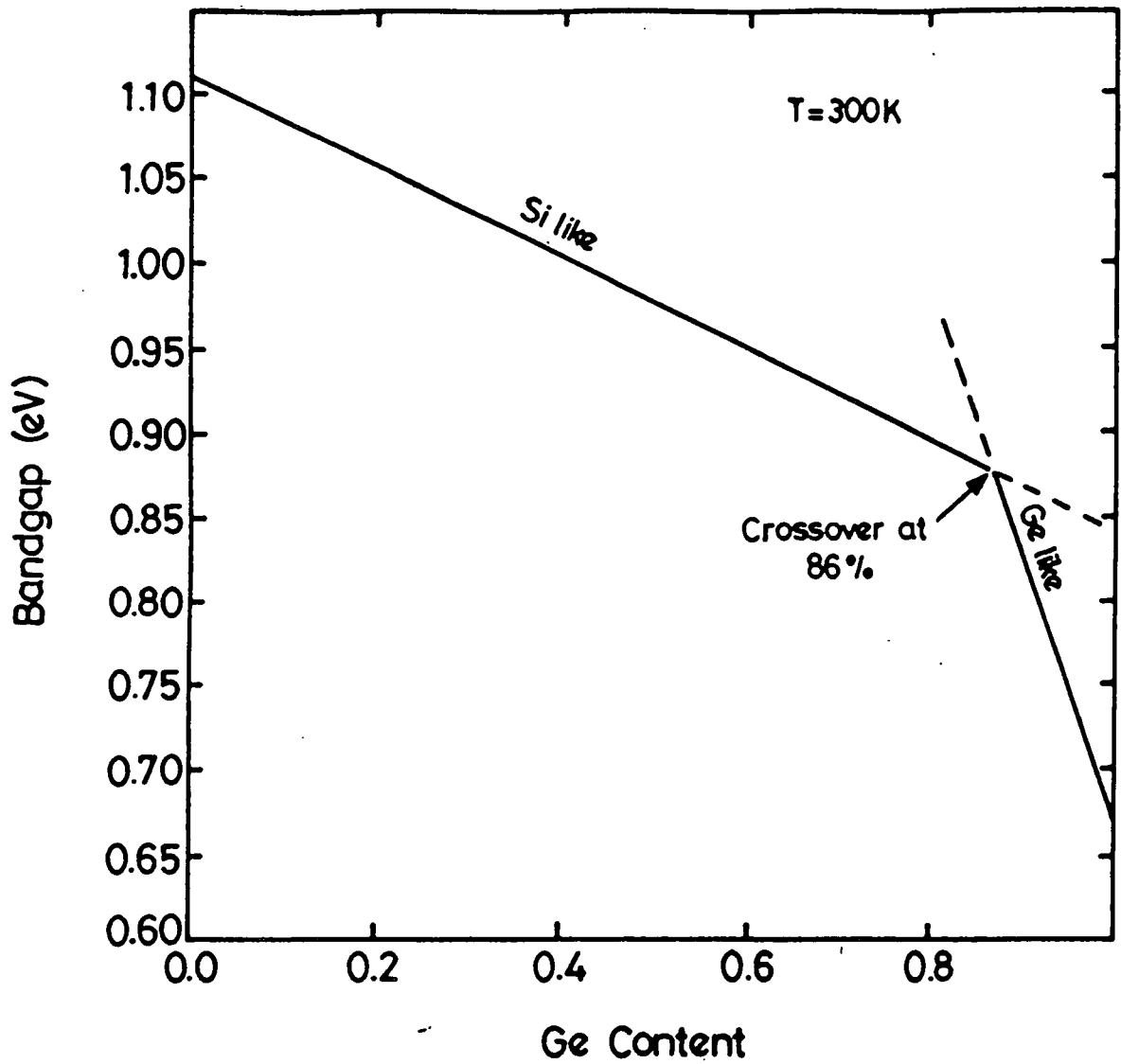
Figure (5.5)   Lowest bandgaps of Si/Ge alloys plotted against
germanium content using calculations described in the text.
The crossover at 86% indicates the point at which the alloy
changes from being silicon-like to germanium-like.

Effects of Alloying.

Although alloying cannot be said to provide an independent test of the bulk and hydrostatic pressure fittings it does provide an interesting test of the work so far done before the more stringent investigations of the effects of uniaxial pressure are undertaken.

Figure (5.5) shows the variation of the lowest bandgap of unstrained Ge_xSi_{1-x} alloy with Ge content. A virtual crystal approximation (VCA), employing the pseudopotentials and their gradients obtained above, was used. The actual calculation of the bandstructure (and hence the bandgaps) for the various alloys involves two processes. First the fact that in a Ge_xSi_{1-x} alloy the germanium atoms will lie on a smaller cubic lattice than usual whereas the silicon atoms lie on a larger one. This means that the germanium atoms can be considered to be experiencing a hydrostatic pressure and so the appropriate pseudopotential factors will be of the form:

$$V^{ge}_{alloy,G} = V^{ge}_{G} + \frac{\partial V^{ge}_{G}}{\partial a} da$$

where the change in lattice constant da depends on the amount of silicon and germanium present. The silicon formfactors become:

$$V^{si}_{alloy,G} = V^{si}_{G} + \frac{\partial V^{si}_{G}}{\partial a} da$$

It is these 'alloy' formfactors that must be combined in the correct proportion to give the bulk alloy formfactors:

$$V_{alloy,G} = (1 - x)V^{si}_{alloy,G} + xV^{ge}_{alloy,G}$$

which are used to calculate the bandstructure in the usual way.

The most important feature is the crossover from Si(Δ)-like minimum to Ge(L)-like minimum at 86% Ge concentration. This figure agrees well with experimental work (Braunstein et al, 1958) which found a crossover at 85%. It is interesting to note that in a self consistent bandstructure calculation (Podgorny et al, 1986) the crossover was calculated to be at 88%. The lines, to all intents and purposes, are linear. This does not agree with experimental results which show considerable sublinear bowing. This is partly a result of the non-inclusion of B_0' - or equivalently of taking the three parameters for the gradients at V_3, V_8 and V_{11} to be linear in q. Nevertheless the discrepancy between experiment and calculation is never greater than 50meV, which will not constitute a major error when compared with the uncertainty in the values of offsets and uniaxially strained bandgaps.

Uniaxial Pressure.

It should be noted that until now, with the exception of the alloying result, the comparison of the calculated bandgaps, effective masses and variation of gaps with hydrostatic pressure has involved no more than making the best possible fit to the experimental results. In other words no new information has been gained. When we come to carry out calculations on uniaxial strain effects we are carrying out a direct test of whether the simple model employed can be extended to more interesting and complicated results.

Experimental evidence for uniaxial strain effects is scarce for silicon

Figure (5.6) Energy versus momentum for biaxially compressed
germanium (as for the case of germanium grown on (100)
silicon) at the top of the valence band in the (100)
direction. The bands are seen to be more parabolic than
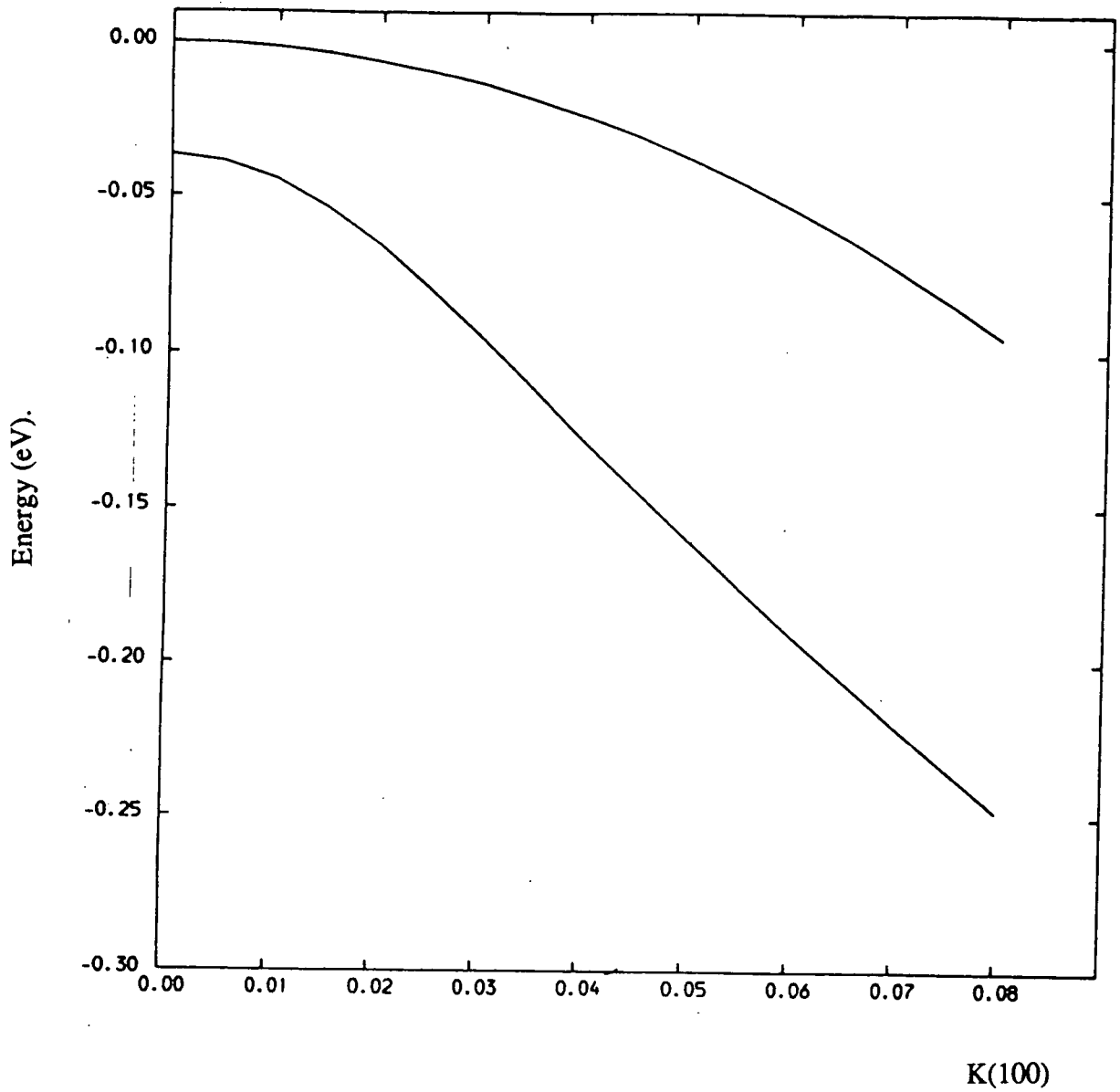those of figure (5.7).
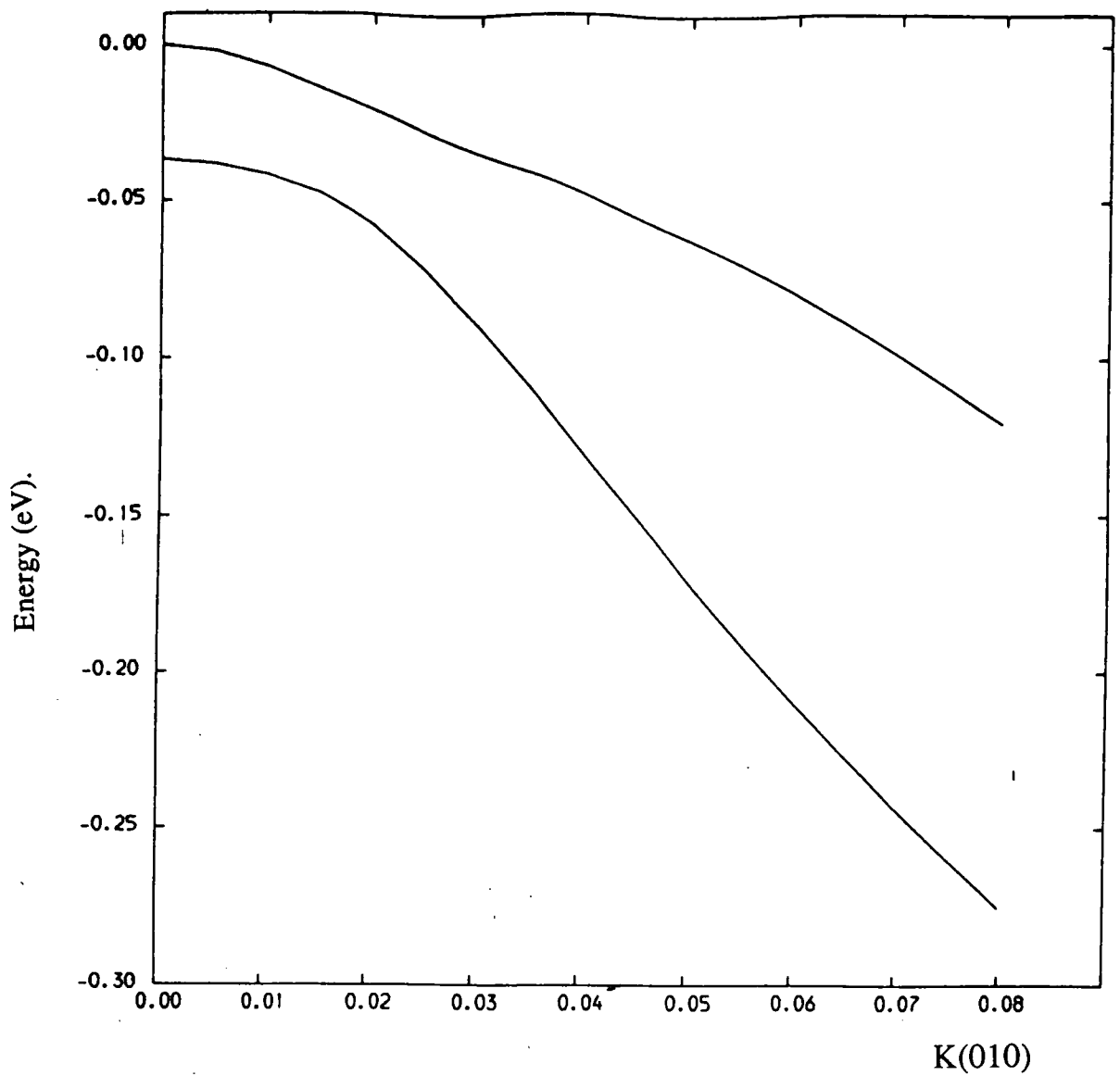
Figure (5.7) Energy versus momentum for biaxially compressed
germanium (as for the case of germanium grown on (100)
silicon) at the top of the valence band in the (010) direction.
Anticrossing effects can be observed between k=0.00 and
k=0.05 .

and germanium, consequently the results of the pseudopotential calculation will be compared with those of a straightforward deformation potential calculation (DPC) (People, 1986 and People and Jackson, 1987). DPC's may be expected to give good descriptions of the variation of bandgaps and effective masses with strain but that is all, i.e. they cannot provide a convenient method of calculating energy eigenstates of a strained crystal.

Valence Band Splitting.

The application of uniaxial pressure decreases the symmetry of the crystal and consequently reduces certain degeneracies in the Brillouin zone. As a particular example the heavy and light holes at the top of the valence band split into two states (four including spin) denoted as the $\left(\frac{3}{2}, \pm\frac{1}{2}\right)$ and $\left(\frac{3}{2}, \pm\frac{3}{2}\right)$ bands. For the case of Ge_xSi_{1-x} on a smaller substrate the $\left(\frac{3}{2}, \pm\frac{3}{2}\right)$ is the higher at the Γ point. Figure (5.6) shows the E-k relationship in the (100) direction for Ge on $Ge_{0.8}Si_{0.2}$ showing the expected parabolic bands. Figure (5.7) shows a similar plot for the (010) direction. In this case anti-crossing can be observed. This is the expected result and can be explained simply in terms of overlaps of P_x, P_y and P_z orbitals (O'Reilly, 1986).

Bandgap Variation.

Figure (5.8) shows the variation of the valence band splitting for a Ge_xSi_{1-x} alloy on a Si substrate against Ge content 'x' using the results of a pseudopotential calculation (solid line) compared with the results of a DPC (dashed lines). The two dashed lines show the extent of the error
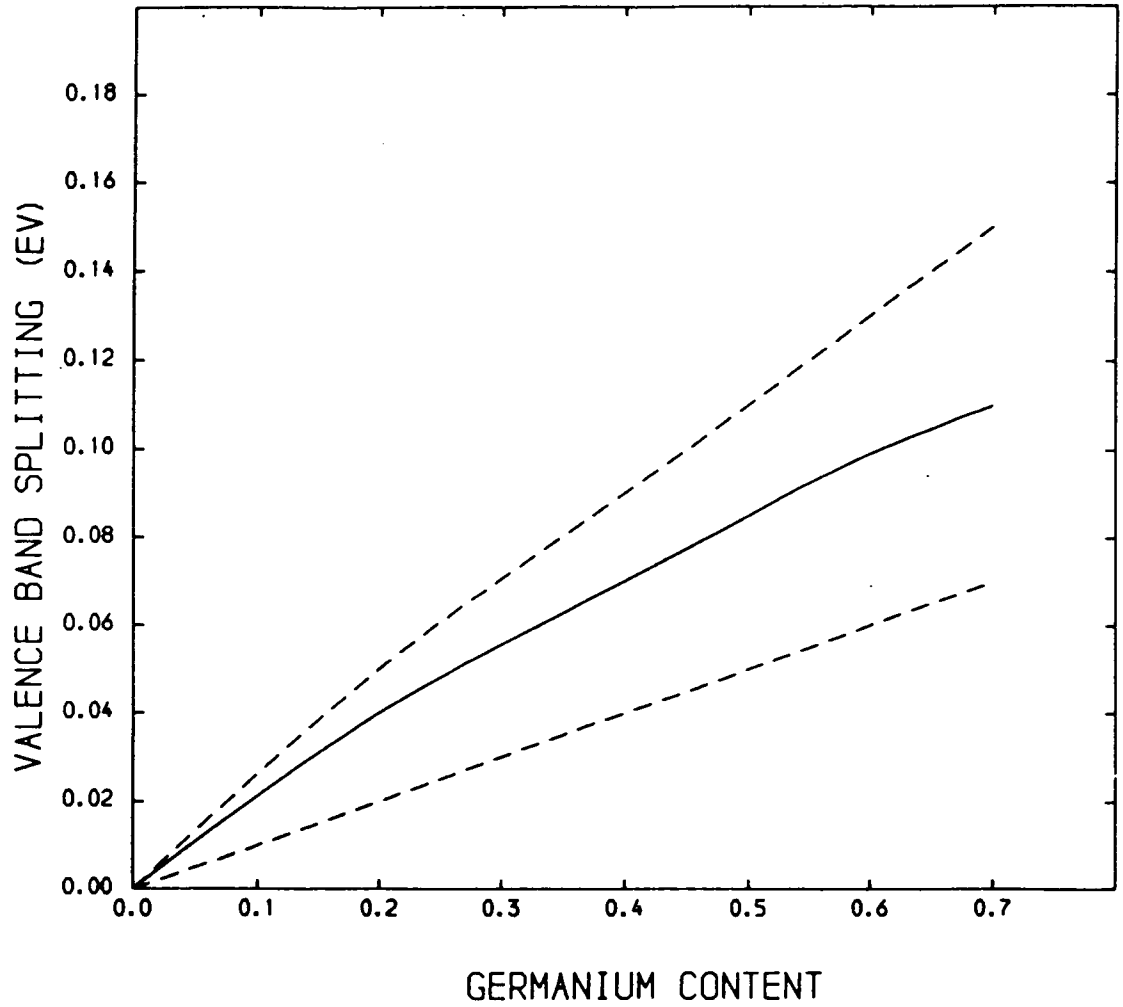
Figure (5.8)   Valence band splitting for a Ge_xSi_{1-x} alloy
grown on an unstrained Si substrate (separation between heavy
and light holes).   The continuous line   shows the results of our
pseudopotential calculations   and the broken lines show the
results of a deformation potential calculation with the separation
between the lines representing the associated error bars.

Bandgap Energy (eV) (y-axis)

Ge content of substrate. (x-axis)

Figure (5.9)   Showing the variation of the smallest bandgap of
strained silicon grown on a Ge_xSi_{1-x} alloy with germanium
content.   The continuous line shows the results of our
pseudopotential calculations and the broken lines show the
results of a deformation potential calculation   with the
separation of the lines representing the associated error bars.

associated with the DPC calculation. The central, pseudopotential result, can be seen to lie well within the outer bounds of the DPC.

Figure (5.9) gives the results of the most demanding test on the silicon fit. It shows the lowest bandgap for Si on a range of Ge_xSi_{1-x} alloys. It is important to notice that the Si is experiencing a biaxial extension and so the lowest conduction band state is the Δ-minimum in the (100) direction. This time the pseudopotential calculation does not agree as well with the DPC. For the largest strain shown, Si on $Ge_{0.6}Si_{0.4}$, the difference in the two calculations is approximately 0.1eV. The main contribution to this error seems to come from the large valence band splitting. This hypothesis is supported by the fact that a similar calculation, but without spin, raises the pseudopotential line to give a good overall agreement with the DPC. Nevertheless, this error of 0.1eV must be borne in mind for any calculation using strained silicon.

Figure (5.10) shows a plot of lowest bandgap for a Ge_xSi_{1-x} alloy on unstrained Si. Since this corresponds to the setup for most experiments and proposed devices it is the most relevant test of the fits. As can be seen the agreement between the two calculations is excellent in the range shown; the discrepancy never exceeding 25meV. Here again the pseudopotential calculation gives a virtually straight line, compared with the significantly curved lines of the DPC. As a final test for biaxial compression it is possible to compare the bandgaps for pure Ge on an unstrained Si substrate. This setup produces a very large strain in the Ge($\approx$4.2%). Figure (5.11) shows
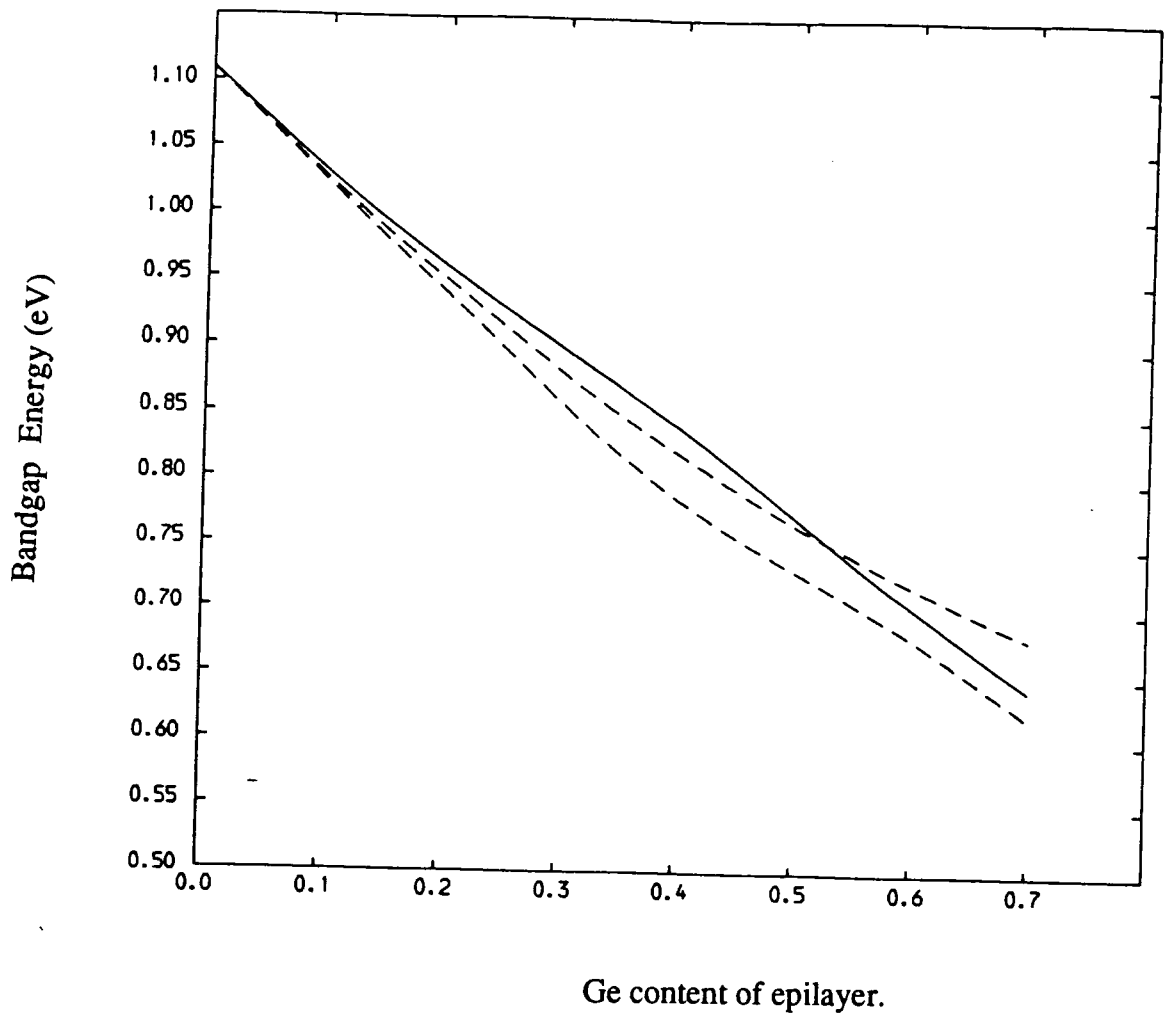
Figure (5.10)   Showing the variation of the smallest bandgap
    of a strained Ge_xSi_{1-x} alloy grown on an unstrained silicon
    substrate.   The continuous line shows the results of our
    pseudopotential calculations and the broken lines show the
    results of a deformation potential calculation,   with the
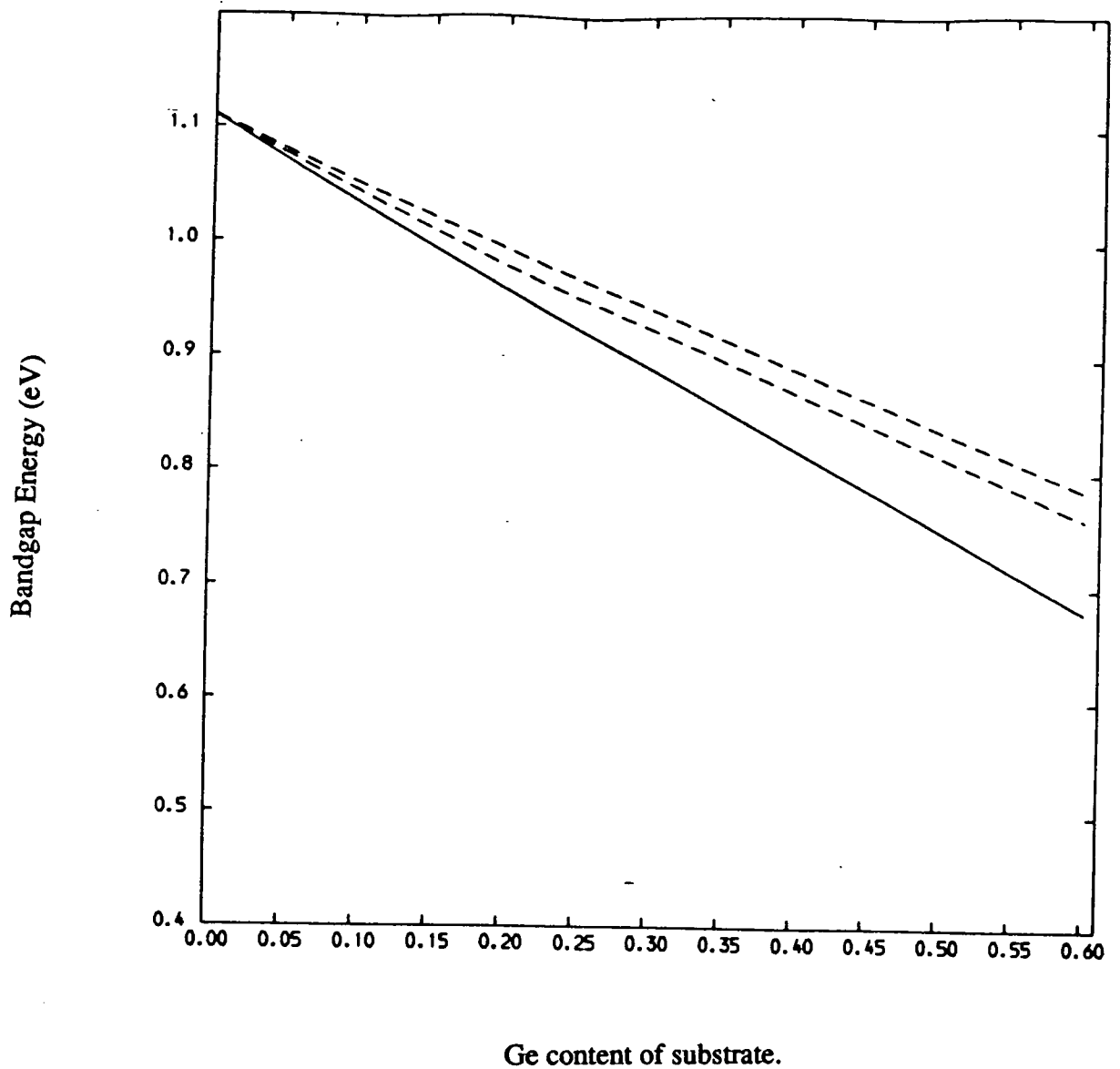   separation of the lines representing the associated error
    bars.

Γ_2' ————————— 0.780

0.680 ——————— $\Delta_1^{\|}$

$\Delta_1^{\|}$ ————————— 0.65

0.62 —————— Γ_2'

$\Delta_1^{\perp}$ ————————— 0.000   0.000 ——————— $\Delta_1^{\perp}$

$\left(\dfrac{3}{2},\dfrac{3}{2}\right)$ ————————— -0.445   -0.443 —————— $\left(\dfrac{3}{2},\dfrac{3}{2}\right)$

$\left(\dfrac{3}{2},\dfrac{1}{2}\right)$ ————————— -0.595   -0.600 —————— $\left(\dfrac{3}{2},\dfrac{1}{2}\right)$

Deformation Potential Calculation.   **Pseudopotential Calculation.**
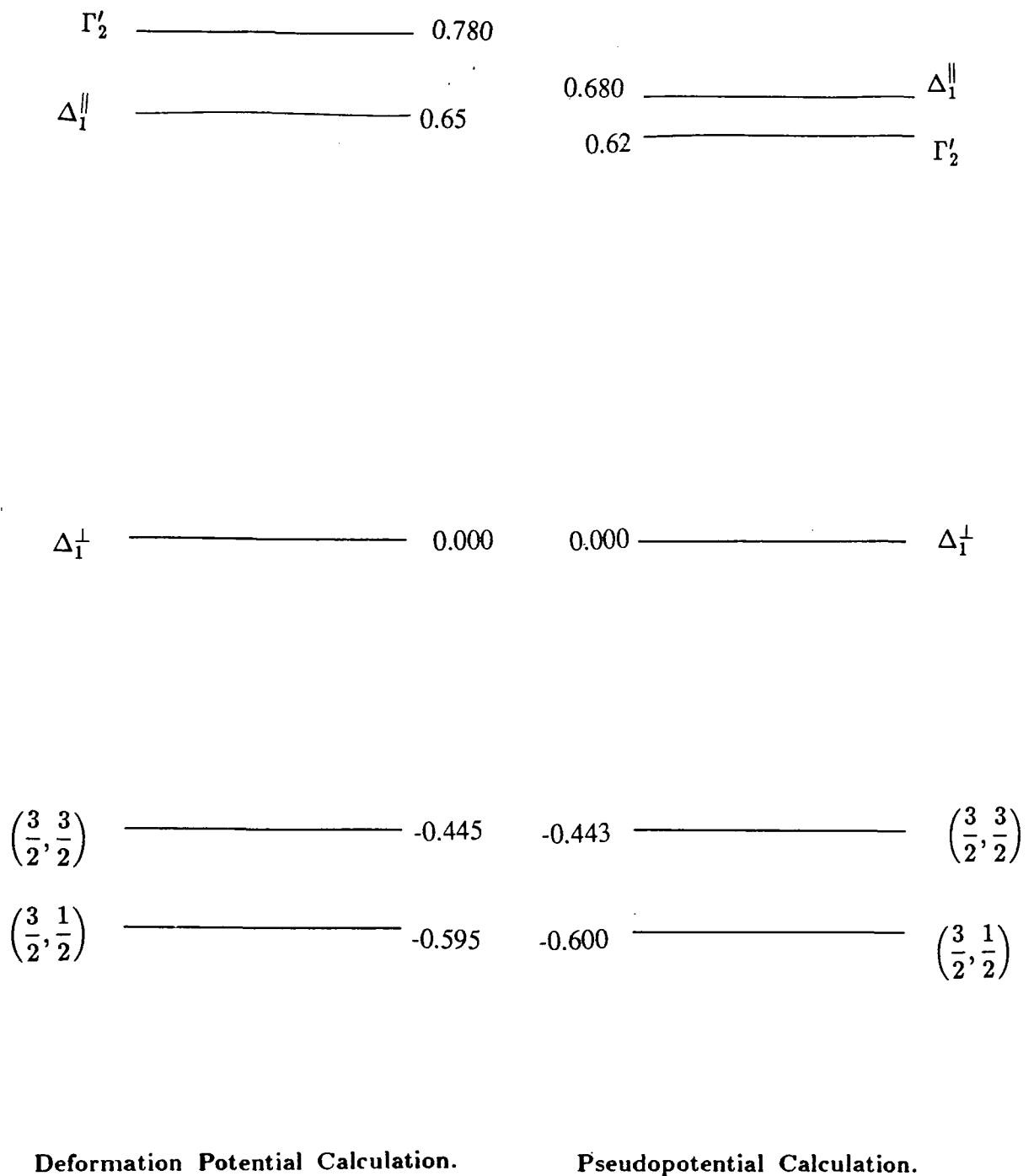
Figure (5.11)   A comparison of the energy levels for germanium grown on unstrained silicon calculated both by a deformation potential method and our pseudopotential method.   All of the levels are given in eV and the bottoms of the conduction bands have been aligned at 0.0eV.

the relevant values for the DPC and the pseudopotential calculation. The comparison is very good with the size of the bandgaps being fairly accurate. The main discrepancy is due the fact that the Γ_2' state lies slightly below the $\Delta_1^{\perp}$ minimum rather than slightly above it. This is probably due to the fact, as was mentioned earlier, that the error in the fitting of the variation of the Ge $\Gamma - \Gamma$ gap with hydrostatic pressure was quite large($\approx 10\%$). This ordering problem means that results for superlattices and quantum wells with this setup must be treated with a certain amount of caution.

Summary.

We have shown that by means of a simple technique we can model the effects of both hydrostatic and uniaxial strain of silicon and germanium to a high degree of accuracy over a wide range of physical conditions. This allows reliable calculations to be made on various Si/Ge strained systems in a manner exactly analogous to that employed in chapters 3 and 4.

Also it should be possible, with some extra fitting, due to the presence of both symmetric and antisymmetric pseudopotential formfactors, to carry out the same modelling of strain effects for III–V materials as has been carried out by others for hydrostatic pressure effects (Ko and Inkson, 1987). No attempt will be made to model the effects of strain in III-V materials in the following work but will rather concentrate on two particular Si/Ge structures with interesting physical characteristics.

CHAPTER SIX

TWO PARTICULAR EXAMPLES OF SiGe STRUCTURES

Introduction.

In chapter 5 we showed how it is possible to model the effects of strain in Si, Ge and SiGe alloys. By using the techniques of Chapter 2 we are able to calculate properties of various Si/Ge low dimensional structures such as the bandgaps or the effective masses of different bands. We can also plot wavefunctions in particular directions (along bonds for example) or averaged over unit cell faces.

In this chapter we shall bring all of these techniques together to allow us to investigate two particular examples of Si/Ge low dimensional structures. We shall finish by considering a Si_4Ge_4 superlattice but we shall begin by investigating a quantum well in which the effects of the indirect bandgaps will be shown to play a major part.

The Strained Quantum Well.

In comparison to the III-V alloy low dimensional structures, little theoretical work has been done on the corresponding Si/Ge structures. Two exceptions have dealt with $Ge_{0.25}Si_{0.75}(Si/Ge_{0.5}Si_{0.5})$ superlattices (Morrison et al, 1986 and de Sterke and Hall, 1987) which represents a struc-

ture in which the strain is shared equally through the superlattice. In this section, however, we shall consider the conduction band states of a $Ge_{0.25}Si_{0.75}/Si/Ge_{0.25}Si_{0.75}$ quantum well. This configuration allows us to consider the effects of slightly straining the silicon on an alloy substrate in such a way that the silicon forms the conduction band well, in the (100) direction – as would be required for device applications where the electrons will travel in the elemental material, avoiding alloy scattering.

To calculate the energy levels of a $Ge_{0.25}Si_{0.75}/Si/Ge_{0.25}Si_{0.75}$ quantum well it is necessary to determine various offsets. We have, from the literature, a theoretical value for the valence band offset ignoring spin-orbit splitting and strain effects which is given by:

$$\Delta E_v = (0.74 - 0.53x)x \qquad\qquad 6.1$$

where x is the proportional content of Ge (People, 1986). For the present case $x = 0.25$, but we must also incorporate the effects of spin and strain into the value of ΔE_v.

Using the methods of chapter 5 we find that the strain splitting at the top of the valence band for the silicon is 0.137eV; with the topmost band moving up 0.044eV with respect to its original position. We shall ignore the effects of spin on the silicon portion of the quantum well. In the alloy there is no strain splitting but there is a spin-split-off separation of approximately one quarter of that of bulk germanium (assuming linear interpolation for alloys) i.e. 0.075eV. We can assume that the introduction
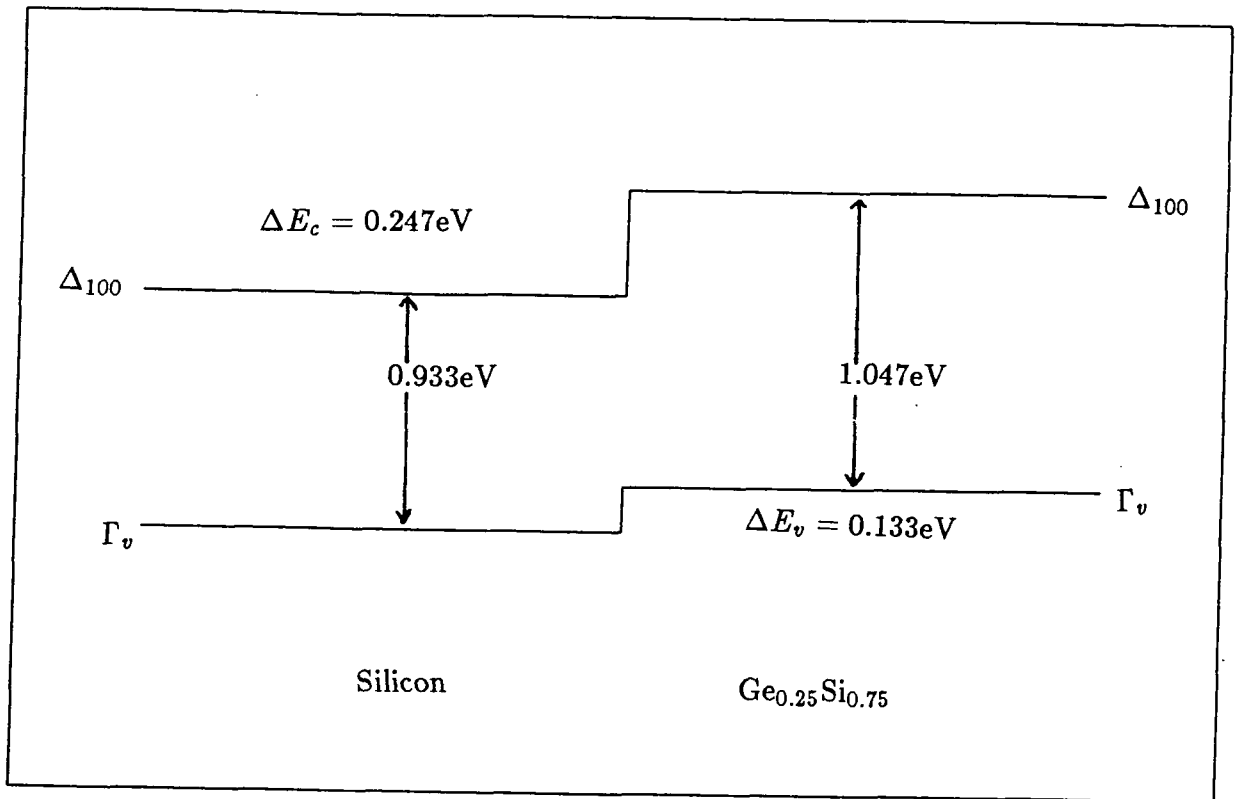
Figure (6.1) Band offsets for the $Ge_{0.25}Si_{0.75}/Si/Ge_{0.25}Si_{0.75}$ quantum well discussed in the text.

of the spin-split-off effects to the alloy forces the top of the valence band up by 0.025eV and the SSO component down by 0.05eV (maintaining a 'centre of energy' at the same point in the bandstructure). This gives, then, a valence band offset of

$$\Delta E_v = (0.74 - 0.53 \times 0.25)0.25 - 0.044 + 0.025 = 0.133\text{eV}$$

It is important to note that this estimate of the offset is prone to error both from the original equation (6.1), which is based on calculations on elemental structures (Van de Walle and Martin, 1986) but also from some of the implicit assumptions which have been made to include the effects of strain and spin. In particular the assumption of linear effects with alloying and strain cannot be totally justified. More will be said on the errors associated with the valence band offset in the concluding sections of this chapter. But here we shall just comment that this work on the $Ge_{0.25}Si_{0.75}/Si/Ge_{0.25}Si_{0.75}$ quantum well will be more involved with the qualitative nature of the energy levels rather than the specific values of bandgaps.

Using values for the bulk bandgaps taken from chapter 5 and the value of ΔE_v as calculated above we obtain the overall band offsets of figure (6.1). With this information and the correct expansions of the complex bandstructure we can employ the methods of chapter 2 to calculate the energy levels in the (100) direction of the $Ge_{0.25}Si_{0.75}/Si/Ge_{0.25}Si_{0.75}$ quantum well as a function of width. The results of such a calculation
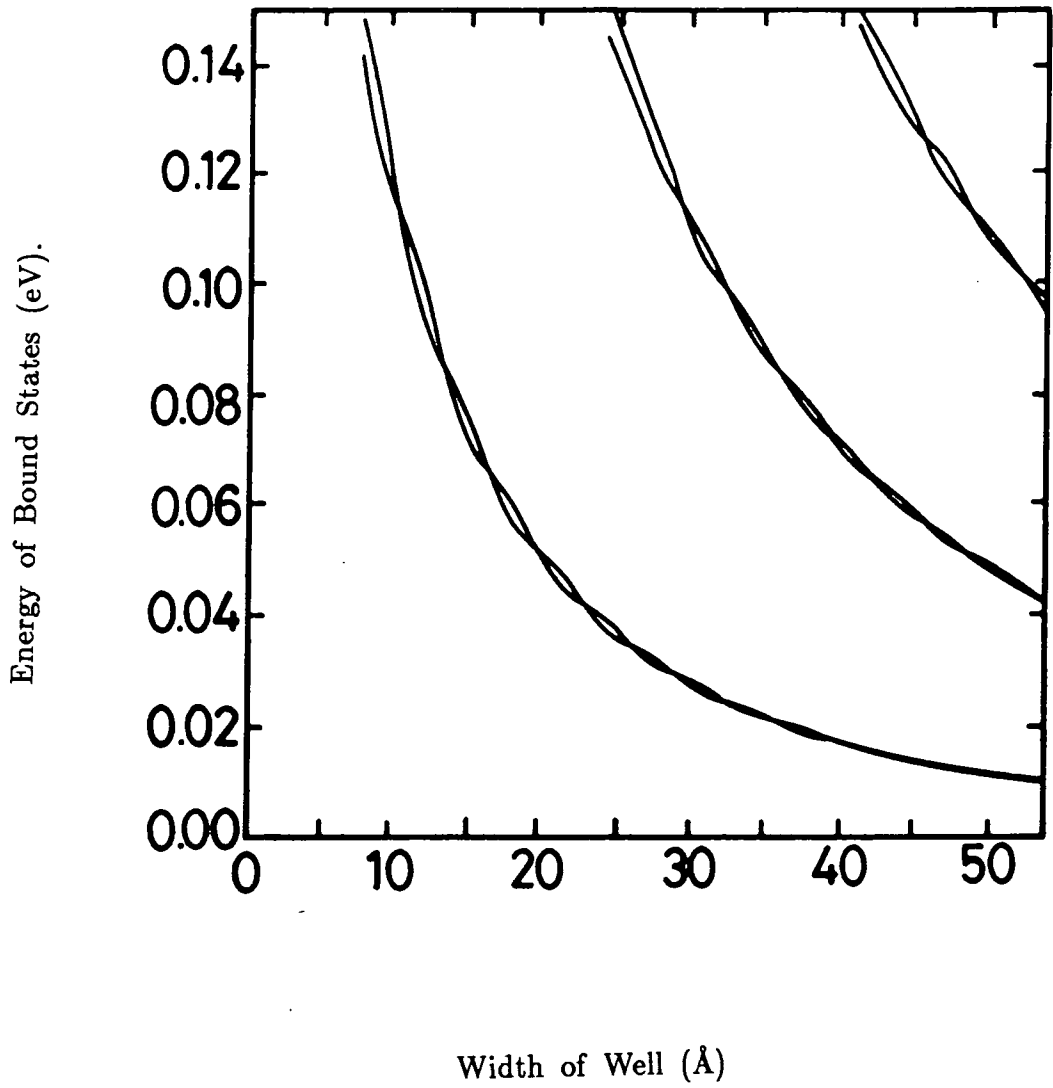
Figure (6.2) Energy levels of quantum well plotted against well
width for states at the bottom of the conduction band over a
range of 55 Ångstroms.

can be seen in figure (6.2) over a range of 0.14eV. It should be noted that the calculations have also been carried out for fractional (i.e. physically non-obtainable) widths in order to give a clearer indication of the oscillatory nature of the splitting effect.

If only the gross features of figure (6.2) are considered we can see the usual drop in energy of any particular 'state' with increasing width of well. It is evident, however, that some extra physics is at work since each level is actually formed from two 'quasi-degenerate' states which are coupled together by some mechanism. To try and find some indication as to what is happening between the pairs of states we have plotted out the averaged charge densities for a well width of 42.1Å for the two lowest states (which have a small splitting unobservable in figure (6.2)) in figure (6.3) which were found to be identical and both having the form expected of a ground state. Similarly for the third and fourth states, in figure (6.4), we obtain the averaged charge density plot one would expect for a first excited state for both components. In other words it seems as if we have two ground states and two first excited states existing within the quantum well.

The explanation for these phenomena can perhaps best be understood with reference to the schematic bandstructure of figure (6.5) – which shows that at a particular energy we have four states with similar wavevector magnitudes, rather than the two we might assume from a straightforward effective mass model – and by consideration of a simplistic one-dimensional effective mass type model. We shall, for simplicity, consider an infinite
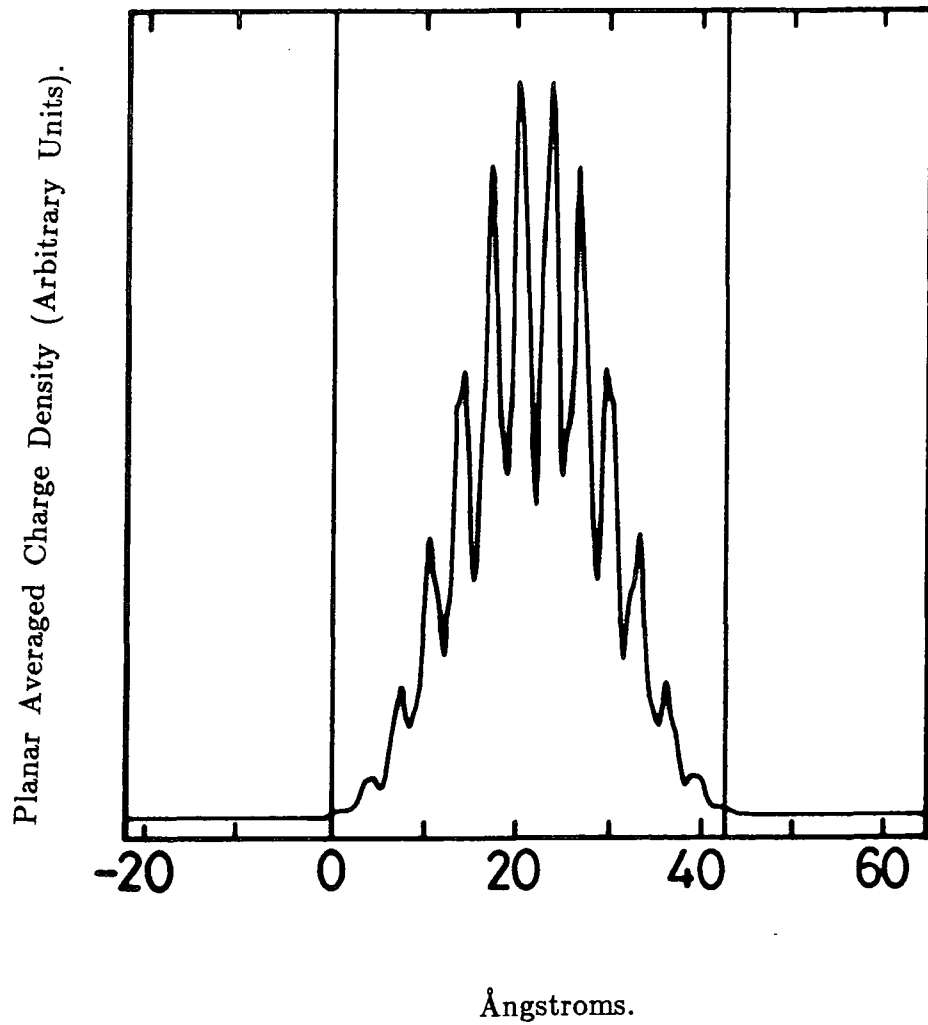
Figure (6.3)   Averaged charge density for the lowest state of the quantum well in the (100) direction.   The second lowest state is identical (see text for discussion).
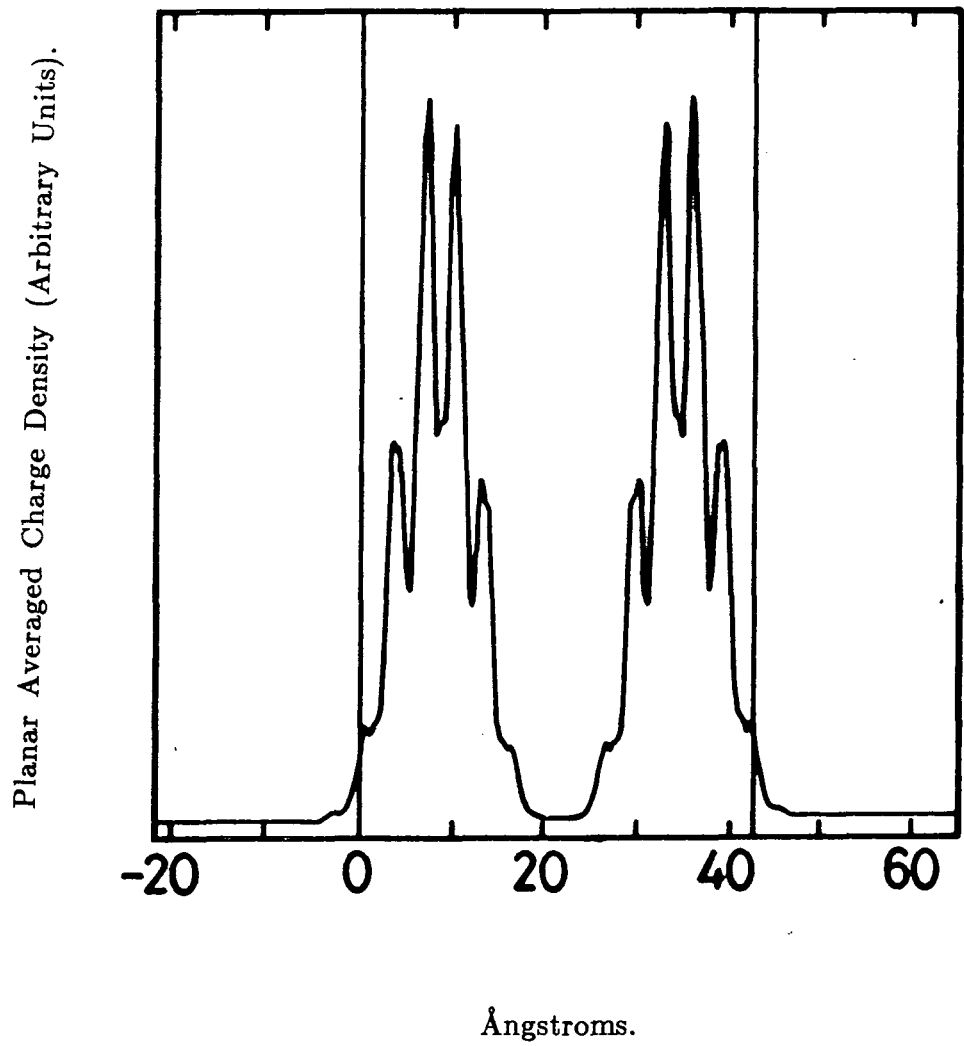
Figure (6.4) Averaged charge density for the third lowest state of the quantum well in the (100) direction. The fourth lowest state is identical (see text for discussion).

quantum well such that

$$V(x) = \infty, -W/2 > x > W/2$$

$$V(x) = 0, -W/2 < x < W/2$$

We have solutions of the form e^{ikx} and e^{iqx} in the well region. Since the potential is symmetric in this simplified model we know from elementary quantum mechanics (Schiff, 1949) that the eigenfunctions must have a definite parity. For the lowest symmetric state we can hypothesise a normalised state of the form

$$\Psi = \mu \cos kx + \lambda \cos qx \qquad 6.2$$

and impose the condition that $\Psi = 0$ at $x = \frac{W}{2}$ to give

$$\frac{\mu}{\lambda} = \frac{-\cos qW/2}{\cos kW/2} \qquad 6.3$$

Now, if we hypothesise that a second state can be constructed of a similar form to Ψ but at a slightly different energy and hence with slightly different values of k and q, we can write this state as

$$\hat{\Psi} = \hat{\lambda} \cos \hat{k}x - \hat{\mu} \cos \hat{q}x \qquad 6.4$$

to give

$$\frac{\hat{\lambda}}{\hat{\mu}} = \frac{\cos \hat{q}W/2}{\cos \hat{k}W/2} \qquad 6.5$$

The energy of the state Ψ may be expected to be given by an expression of the form

$$E_\Psi \propto \frac{\lambda^2 k^2}{m_k} + \frac{\mu^2 q^2}{m_q} + (\text{crossterms in k and q}) \qquad 6.6$$

whereas for $\hat{\Psi}$;

$$E_{\hat{\Psi}} \propto \frac{\hat{\mu}^2 \hat{k}^2}{m_k} + \frac{\hat{\lambda}^2 \hat{q}^2}{m_q} + (\text{crossterms in } \hat{k} \text{ and } \hat{q}\ ) \qquad 6.7$$

Where m_k and m_q are the effective masses appropriate to the bulk states at the energies E_ψ and $E_{\hat{\psi}}$. The question now arises as to whether it is possible to find a 'configuration' in which $E_\psi = E_{\hat{\psi}}$. For such a case $\hat{k} \to k$ and $\hat{q} \to q$. Also, we may expect, at least to a first approximation, the cross terms in 6.6 and 6.7 are equal. Subtracting equation 6.6 from equation 6.7 we find that

$$\hat{\mu}^2 = \lambda^2$$

$$\mu^2 = \hat{\lambda}^2$$

Which give, using equations 6.3 and 6.5;

$$\cos qW/2 = \pm \cos kW/2$$

which has the general solutions

$$qW/2 = n\pi \pm \frac{kW}{2} \qquad 6.8$$

where n is an integer. Rearranging equation 6.8 gives

$$q \pm k = \frac{2n\pi}{W} \qquad 6.9$$

Before examining this condition in detail it will be helpful to rescale some of the terms. If we use the dimensionless forms of k and q such that

$$q \to \frac{2\pi}{a} q$$
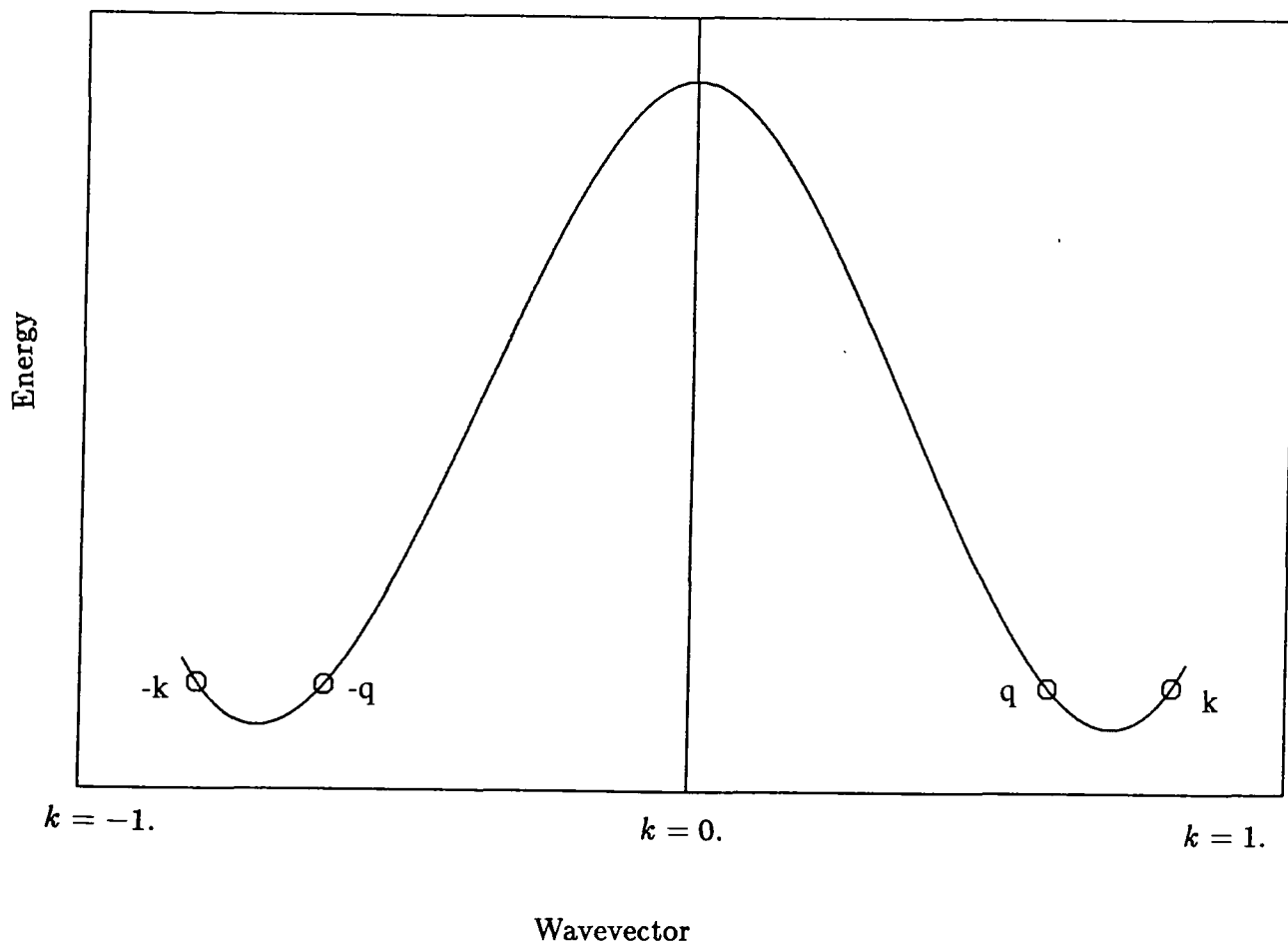
FIgure (6.5) Schematic representation of the bandstructure for
silicon at the bottom of the conduction band.   The points
k, q, -k and -q represent four states at equal energies all
four of which contribute towards forming a quantum well
state.

$$k \rightarrow \frac{2\pi}{a}k$$

where a is the lattice constant of the well material, and define a term 'w' which denotes the number of unit cells in the well

$$W = wa$$

then combining these new terms with equation 6.9 and rearranging gives

$$w = \frac{n}{q \pm k}.$$

Typically $q - k$ has a value of about 0.1 so that for the widths considered in figure 6.2 there are no solutions for w. However we can approximate $k + q$ to be 0.85×2 where 0.85 represents the value of the wavevector at which the turning point exists in the bandstructure. This gives, then,

$$w = \frac{n}{2 \times 0.85}. \qquad 6.10$$

This simple model also predicts that the maximum splitting of the doublets reduces with increasing well width – since as the well gets wider the average energy of the doublet falls and $k \rightarrow q$ and $m_k \rightarrow m_q$ — in agreement with the full calculation.

A more rigorous, but physically less clear, discussion of this problem has been given using an envelope function approximation for an infinite quantum well (de Sterke and Hall, 1987). This work also predicts that the splitting of the quasi-degenerate states will be as given in equation 6.10.
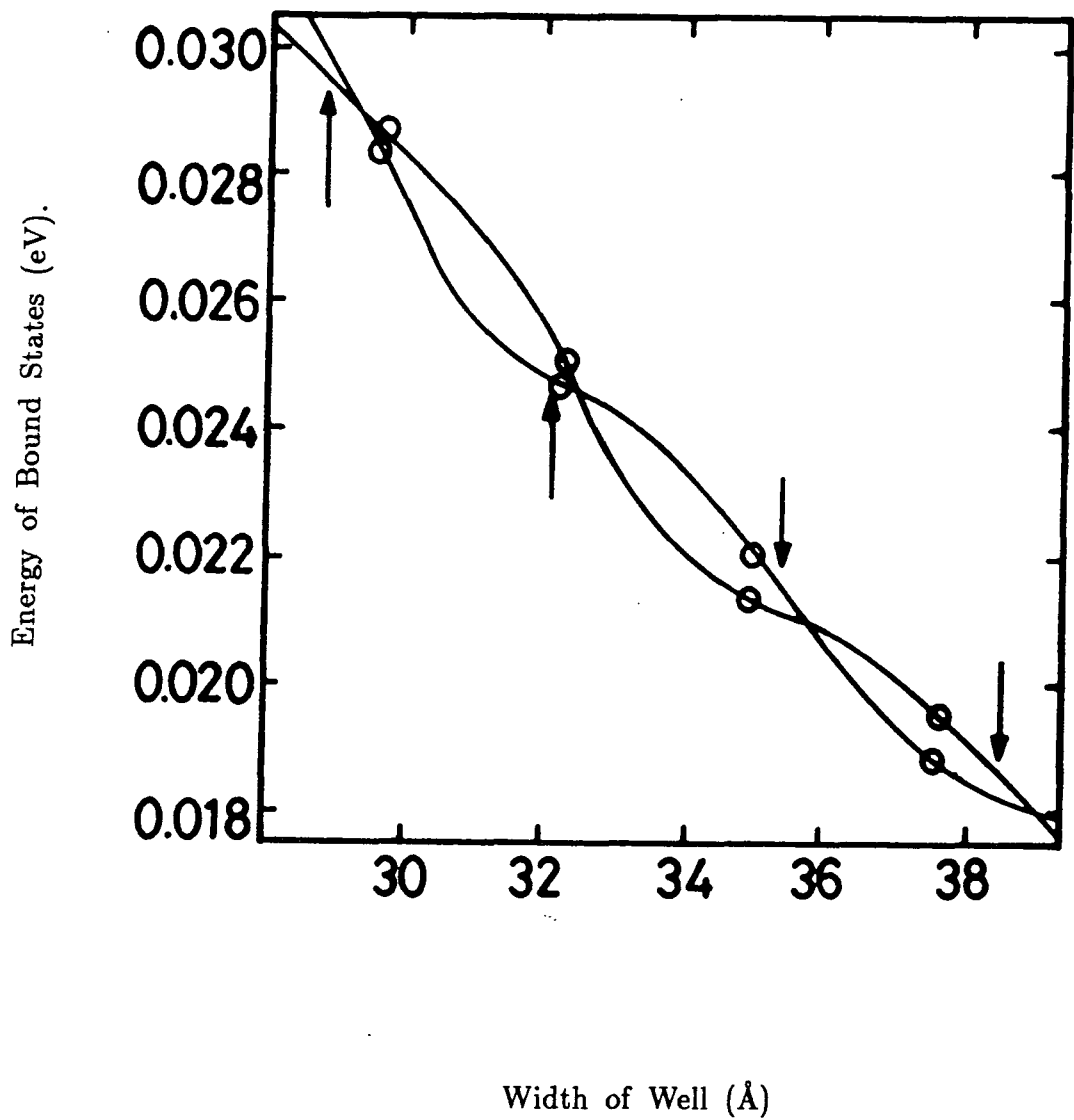
Figure (6.6) An expanded version of Figure (6.2). Physically realisable widths are indicated by open circles. Predicted crossings are shown by arrows.

Figure (6.6) shows an expanded version of figure (6.2) for the 28Å to 40Å well width range. Also shown, by arrows, are the widths predicted by equation 6.2 at which the splittings go to zero for an infinite quantum well. The agreement is good; especially when we remember that the $Ge_{0.25}Si_{0.75}/Si/Ge_{0.25}Si_{0.75}$ quantum well is not infinite and that our calculation uses realistic bandstructure.

We may ask whether these splittings will be physically observable. The separation between two quasi-degenerate states is of the order of 2meV (the actual size of the maximum splittings increases with decreasing well width) and is, therefore, unlikely to be observed at room temperature but may show up for very low temperature experiments.

This section has shown that the indirect nature of silicon results in some unusual properties when low dimensional structures are produced. In the next few sections we shall turn our attention to a particularly important superlattice configuration.

The Si_4Ge_4/Si Superlattice.

In this section we shall consider a Si_4Ge_4 superlattice grown on a Si(100) substrate. The impetus for this calculation came from an electroreflectance experiment carried out on a $(Si_4Ge_4)_5$ quantum well (Pearsall et al, 1987) which was able to report on various optical transitions which could not be explained in terms of the bandstructure of bulk silicon or germanium or in terms of any defect-related phenomena. Consequently it was necessary to conclude that the extra transitions were due to features in the superlattice

bandstructure.

The transitions which it was necessary to explain in terms of a low dimensional structure model occurred at 0.76, 1.25 and 2.31eV (Pearsall, 1987) and a weaker transition at 1.8eV (Hybertsen and Schluter, 1987). Electroreflectance was used as the experimental method since it is very sensitive, as much as a thousand times as sensitive as simple absorption or luminescence measurements, and will usually only pick out direct transitions.

In the concluding part of this chapter we shall attempt to explain the magnitude of these observed transitions and investigate their nature, and in particular, due to its important technological applications, whether the transition at 0.76eV is direct or indirect. Rather than do a calculation for the specific structure mentioned above we shall follow other workers and investigate a Si_4Ge_4 superlattice and then try to estimate the error involved.

Other Theoretical Investigations.

We begin our investigation of the $Si_4Ge_4/Si(100)$ superlattice by giving a short summary of the work of others. Theoretical response to the experimental results was comparatively swift. The first paper to appear claiming to explain the results used a deformation potential method to work out offsets and bandgaps and combined this information with a position dependent effective mass theory (People and Jackson, 1987). These authors found that the lowest transition, occurring at 0.76eV, could be direct if one considered surface roughness at the interfaces. This amounts to disregarding selection rules concerning the in-plane momentum.

Soon after, a tight-binding calculation was carried out which found similar results (Brey and Tejedor, 1987). Here the authors suggested that the 0.76eV transition could be interpreted as direct if the superlattice wavevector was not regarded as a good quantum number – due to the lack of infinite periodicity in the growth direction. But this calculation also had the problem of having a poor description of the conduction band states – as for all tight binding calculations, especially for indirect materials.

Most calculations carried out since these first two have used a local density function approximation (LDA) (Hybertsen et al, 1987, Froyen et al, 1987 and Ciraci et al, 1988). All of these LDA calculations found that the 0.76eV transition could not be considered to be direct but was rather an indirect transition to a non-zonefolded in-plane state. Unfortunately, however, since the LDA calculations are notoriously bad at predicting bandgaps these results have to be viewed with a certain amount of caution.

Another paper on the $Si_4Ge_4/Si(100)$ superlattice using a 'non self-consistent pseudopotential method' (Wong et al, 1988) argued that the indirect transition was an unlikely explanation since an indirect transition must be accompanied by defects or well width fluctuations or have a large electron-phonon coupling. These authors assert that these are unlikely 'coincidences'. On carrying out a full superlattice calculation they find that in the usual – Poisson ratio determined lattice constants – configuration that the smallest direct bandgap has a magnitude of 1.2eV. Consequently the authors have assumed an *ad hoc* explanation whereby the germanium lattice

constant in the growth direction actually retains its bulk values. They believe that this could be physically realisable if there was a small amount of 'bond bending' and broken bonds in the system.

It is true to say, therefore, that the details of the Si_4Ge_4/Si superlattice have not been resolved unambiguously. In particular the nature of the lowest, 0.76eV, transition – with its important opto-electronic potential – remains unexplained.

Consequently, we shall use our complex bandstructure matching technique to model the superlattice. This will allow us, as was shown in chapter 5, to use a good description of all participating bands – which cannot be done by a tightbinding calculation – and of the bandgaps – which cannot be done by an LDA calculation.

The Calculation.

We begin by discussing the various offsets of the Si_4Ge_4/Si structure. Since silicon forms the substrate for the superlattice the silicon layers of the superlattice will be unstrained and consequently its bandstructure – which is relevant to the offsets – will be as in the bulk. So, we have a twofold (fourfold with the inclusion of spin) degenerate state at the top of the valence band, and an indirect gap in the (100) direction, which is degenerate with the minima in the (001) and (010) directions, of 1.1eV. The direct Γ-Γ gap is 3.4eV and will not affect the present calculation. (For a more detailed account of the silicon bandstructure see chapter 5). In contradistinction the germanium is experiencing a large lateral contraction (lattice constants of
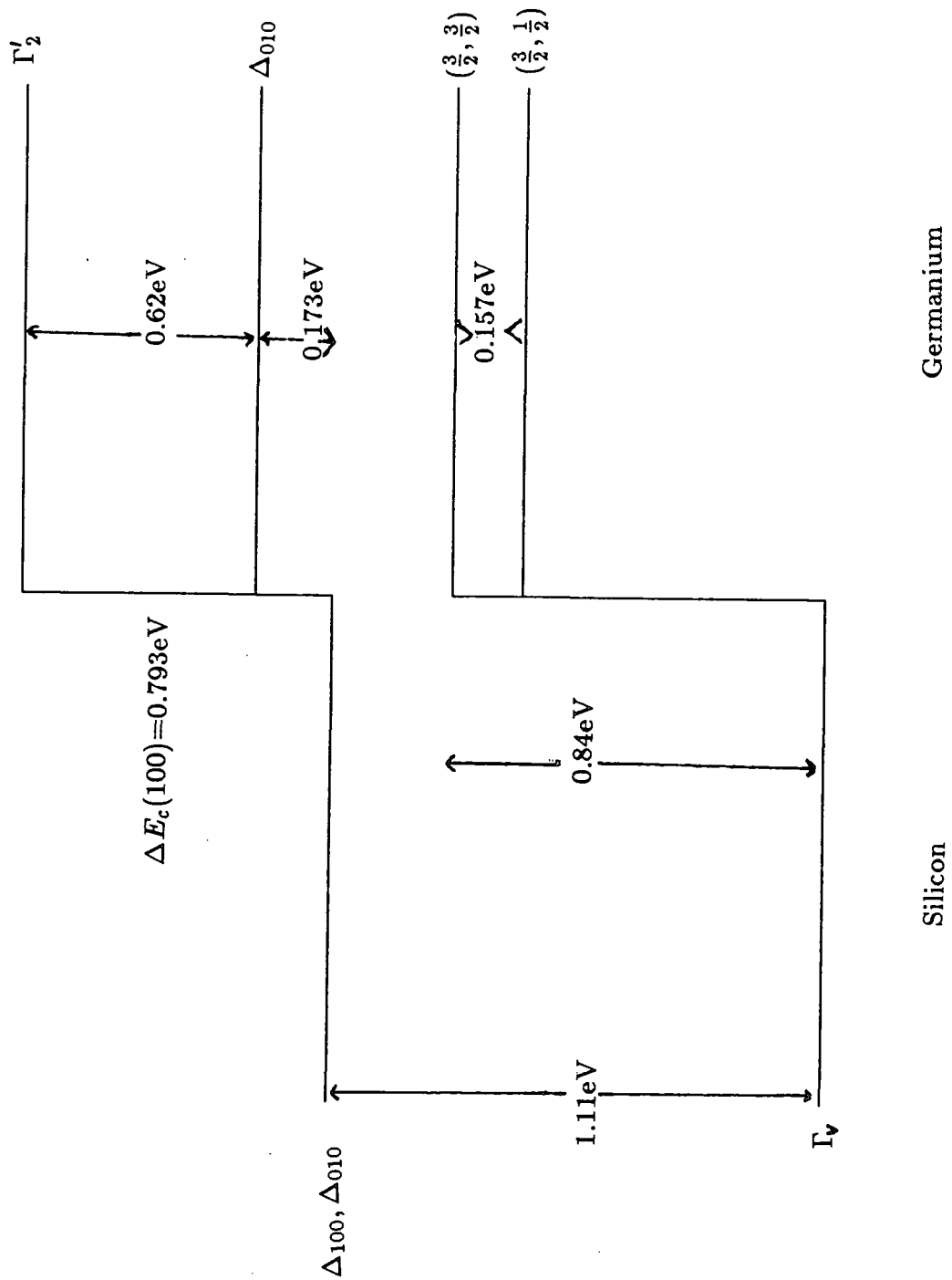
Figure (6.7) The offsets for the $(Si)_4Ge)_4/Si(100)$ superlattice discussed in the text.

silicon and germanium differ by about 4%), and consequently is extended in the growth direction. This splits the degeneracy at the top of the valence band with the $(\frac{3}{2},\frac{1}{2})$ state falling 0.157eV below the $(\frac{3}{2},\frac{3}{2})$ state. The strain also splits the Δ_{100} and Δ_{010} states in the conduction band with the degenerate (010) and (001) states dropping in energy and the (100) states rising in energy with respect to the bulk values. The effect of this splitting is to produce two sets of states separated by 1.063eV.

The valence band offset is taken from a purely theoretical LDA calculation (Van de Walle and Martin, 1986) which predicts a separation of 0.84eV between the top of the two valence bands. Combining all of the information on bandgaps and valence band offsets we obtain an overall structure as shown in Figure (6.7).

Perhaps the most important feature to notice in Figure (6.7) is the small Δ_{010}-Δ_{010} well which forms in the conduction band offsets of the structure. We can see instantly that there must be a superlattice in-plane state with an energy less than 0.173eV above the bottom of the bulk silicon conduction band with an in-plane vector which we would expect to have a magnitude of about 85% of the silicon bulk Brillouin zone-edge wavevector. We shall see later, by using a full calculation, that this is the case and in fact this is an important state in the present investigation of the bandstructure of the superlattice.

Using the offsets of Figure (6.7) the bandstructure of chapter 5 and the methods of chapter 2 we can calculate the bandstructure of the
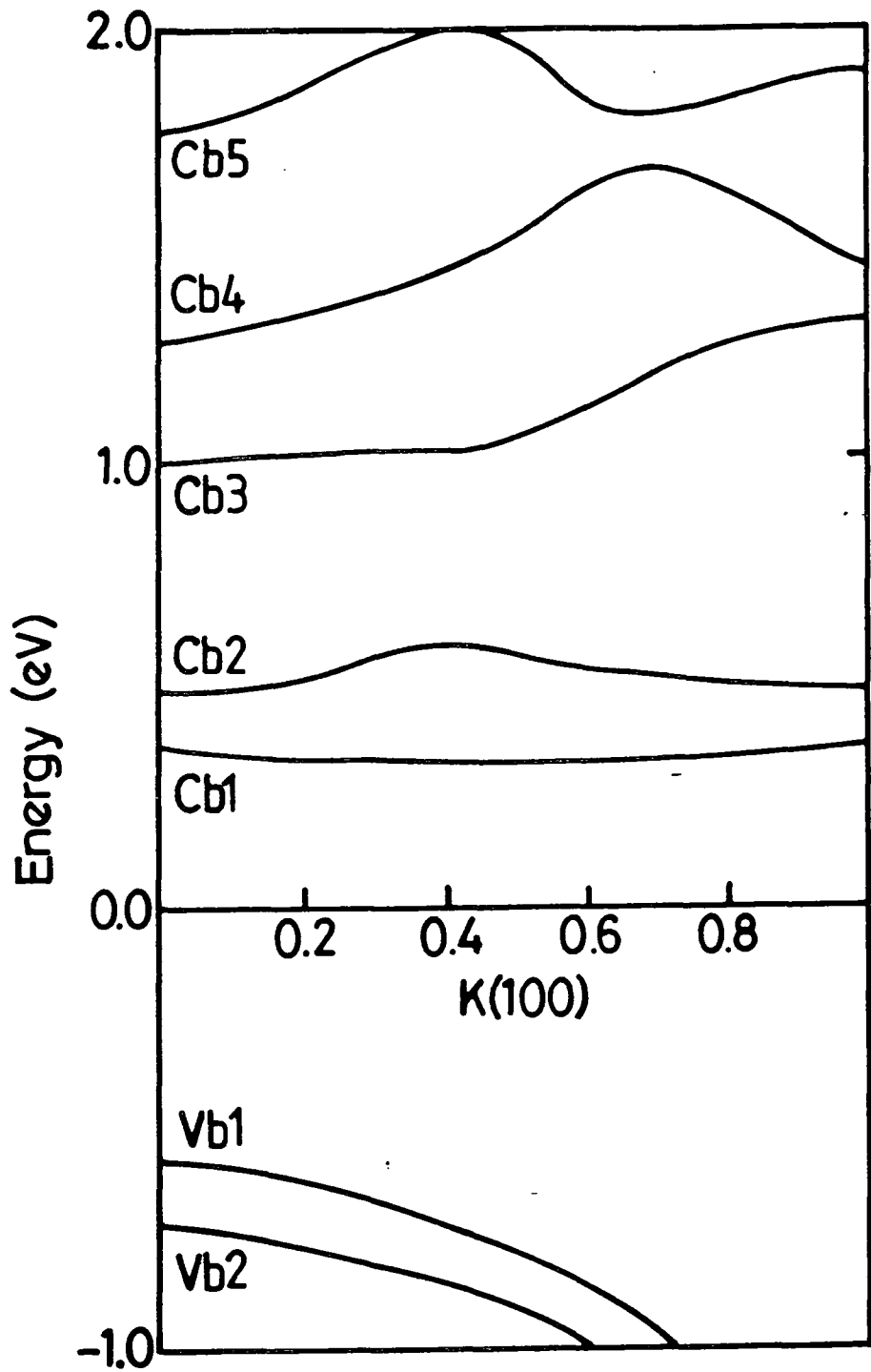
Figure (6.8)   Bandstructure for the $(Si)_4(Ge)_4$ superlattice in the
(100) direction. The top two valence and bottom five
conduction bands are shown.

superlattice. Since the bandstructure perpendicular to the direction of growth will resemble that of the bulk materials we shall not consider the energy levels in the plane of the superlattice. However, the bandstructure in the direction of growth can be expected to display new structure and this can be seen to be the case in Figure (6.8) which shows the top two valence bands and bottom five conduction bands of the superlattice plotted in the (100) direction.

Although fairly rich in character the bandstructure is what one might expect from a zonefolding model. In particular the flatness of the cb1 state can be considered to be a direct consequence of the double folding of the silicon bulk bandstructure between $0.75 < K < 1.00$ (where K is measured in units of $5.6 \times 10^7 \text{cm}^{-1}$). Also from a zonefolding approach we may consider that the states cb1, cb2 and cb3, cb4 are actually paired off at K=0 since they come from the same regions of the bandstructure. This concept will be important when we consider the nature of optical matrix elements later in this chapter.

The actual values of the energy levels, taking the zero of energy to be the bottom of the bulk silicon conduction band, are in eV,

cb1	cb2	cb3	cb4	cb5	vb1	vb2
0.366	0.492	1.015	1.278	1.786	-0.596	-0.728

(Although the superlattice is actually indirect in the growth direction the bowing is less than 10meV and we shall not consider its effect here).

By using the numbers in the table it can be seen that, if they are allowed, the two lowest transitions occur at 0.962 and 1.088eV. If the lower of these transitions is to be associated with the direct 0.76eV transition of the experiment then it is necessary to consider the errors of both the experiment and the calculation.

For the calculation it is difficult to give a precise value for the errors. We expect the errors due to the calculation itself – after the bulk bandstructure and the offsets are known – to be insignificant, with any error due to charge redistribution being negligible (Van de Walle and Martin, 1986). The uncertainty in the bulk bandstructure with components coming from the bandgaps and effective masses can be found from an overview of chapter 5. It seems that the error associated with any state can be considered to be less than 50meV. The uncertainty associated with the offsets, on the other hand, is difficult to give in a quantitative manner but we can get a qualitative feel for the effects of a 0.1eV, say, decrease in the Si/Ge offset. With the valence band offset 0.1eV smaller we expect the valence band states vb1 and vb2 – mainly residing in the germanium – to be virtually unaffected with respect to the bottom of the well (assuming that the 0.84 or 0.74eV well can be approximated by an infinite well model). This means that the energy level falls 0.1eV with respect to the bottom of the silicon conduction band. A similar argument holds in the conduction band for the Δ_{100} states except in this case the well is formed by the silicon and so the effect is to keep the well state in the same position
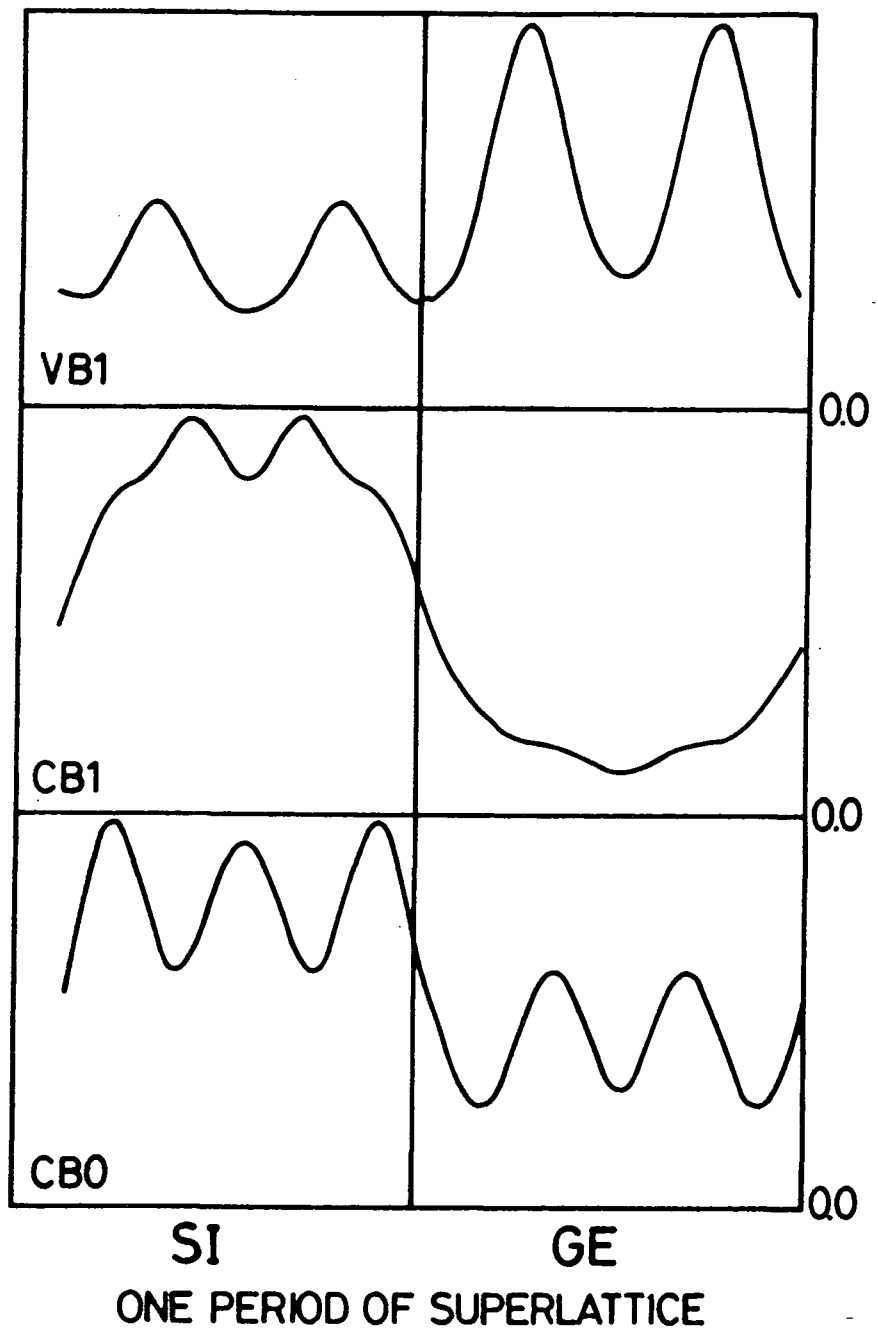
Figure (6.9) Planar averaged charge density plots for cb0, cb1 and vb1 superlattice states.

relative to the bottom of the bulk silicon conduction band. Although the argument may be considered to be a poor approximation, especially since the barriers are very thin (≈ 5.5Å), we may expect the general idea of the transition energy decreasing fairly linearly with offset to hold. Until now, unfortunately, there has been no direct experimental verification of the offset and so it has been necessary to take the already mentioned theoretical offset (Van de Walle and Martin, 1986) with an expected uncertainty of about 0.1eV. To sum up; the errors associated with the bandstructure calculation will be less than 50meV but with an added error due to the uncertainty in the offset. The experimental error for the lowest transition is given to be ± 0.14eV (Pearsall et al, 1986). The experimental and calculational errors taken together leave us with a highest possible experimental value of about 0.90eV and a lower bound for the calculation of 0.90eV. Combined with the uncertainty of the offset it becomes clear that in terms of size of energy transitions the problem of the lowest direct transition remains unclear.

Matrix Elements.

In order to investigate the direct transitions more closely we must consider the role of matrix elements. In electroreflectance experiments the appropriate factor is the optical matrix element of the form

$$| < \psi_f |\mathbf{e}.\mathbf{p}| \psi_i > |^2$$

(Aspnes, 1980). For the particular experiment that we are considering here we need only consider radiation polarised perpendicular to the direction of

growth. So, we need to calculate an integral of the form

$$\int \psi_f^* P_y \psi_i d\tau \qquad\qquad 6.11$$

where the integral is now over all space, taking into account both the barrier and well regions, and P_y is the momentum operator appropriate to the 'y' direction (which can be used without loss of generality). We shall show here that the integral can be evaluated in a straightforward but computationally laborious manner when using our plane wave expansion of the eigenstates. We shall assume that the wavefunction has been normalised for all functions considered so that

$$\int \psi_f^* \psi_f d\tau = 1$$

as is shown in appendix D. Where the integral is taken over the area of the face of a unit cell in the plane perpendicular to the direction of growth and over one period of the superlattice in the direction of growth. We need, then, to expand the expression (6.11) in terms of the plane-wave basis functions. Considering, for simplicity of notation, only the contribution to the matrix element from the germanium region we can write for the conduction band;

$$\sum_j \sum_g C_j a_g^j \exp(i(q_j + g_x)x) \exp(i(\mathbf{k_2} + \mathbf{g_2})\mathbf{r_2})$$

and for the valence band:

$$\sum_{j'} \sum_{g'} V_{j'} b_{g'}^{j'} \exp(i(q_{j'} + g_x')x) \exp(i(\mathbf{k_2'} + \mathbf{g_2'})\mathbf{r_2})$$

where we have used the notation of chapter 2. So the contribution to (6.11)

from the germanium region is of the form:

$$M_{Ge} \propto \int d\tau \sum_{\mathbf{g}} \sum_{\mathbf{g}'} \sum_{j} \sum_{j'} V_{j'}^* C_j b_{g'}^{j'*} a_g^j (q_j + g_x)$$

$$\exp(i(q_j - q_{j'}^* + g_x - g_x')x) \exp(i(\mathbf{g_2} - \mathbf{g_2'} + \mathbf{k_2} - \mathbf{k_2'})\mathbf{r_2}).$$

We can see that for the transition to occur that $\mathbf{k_2} = \mathbf{k_2'}$ which is a statement of conservation of crystal momentum. Completing the integral over y and z gives:

$$M_{Ge} \propto \int dx \sum_{\mathbf{g}} \sum_{\mathbf{g}'} \sum_{j} \sum_{j'} V_{j'}^* C_j b_{g'}^{j'*} a_g^j (q_j + g_x)$$

$$\exp(i(q_j - q_{j'}^* + g_x - g_x')x)\delta_{\mathbf{g_2},\mathbf{g_2'}}.$$

This can be simplified further, by carrying out the integral over the 'x-limits', to

$$M_{Ge} \propto \sum_{\mathbf{g}} \sum_{\mathbf{g}'} \sum_{j} \sum_{j'} \frac{V_{j'}^* C_j b_{g'}^{j'*} a_g^j (q_j + g_x)}{(g_x - g_x' + q_j - q_{j'}^*)} \exp(i(q_j - q_{j'}^* + g_x - g_x')x)\delta_{\mathbf{g_2},\mathbf{g_2'}}\Big|_{x_1}^{x_2}.$$

Where x_1 and x_2 represent the limits of the x coordinate of a germanium layer. A similar 'material dependent' matrix element can be produced for the silicon layer. The overall matrix element is given by a linear combination of the silicon and germanium matrix elements and for the Si_4Ge_4 superlattice we have

$$M \approx M_{Ge} + M_{Si}.$$

Calculation of Matrix Elements.

The matrix elements and the associated transition energies between the Γ-points of vb1 and vb2 and the five conduction bands are given here.

94

Superlattice Matrix elements and energy gaps

$$P_{mn} \qquad\qquad \Delta E_{mn}(eV)$$

	vb1	vb2	vb1	vb2
cb1	0.0000	0.0000	0.962	1.094
cb2	0.0032	0.0077	1.088	1.220
cb3	0.0045	0.0013	1.611	1.743
cb4	0.0001	0.0002	1.874	2.006
cb5	1.0000	1.0000	2.382	2.514

The matrix elements have been normalised in such a way that

$$P_{5,n} = \mid < vbn|P_y|cb5 > \mid^2 = 1$$

for n=1 and 2. We see instantly that the transitions from the valence bands to cb5 are considerably bigger than the transitions to the first four conduction bands. This is easy to understand since the cb5 state is actually a bulk zone-centre state whereas cb1–4 are derived from Δ-related zone-folded states. Also we notice that the matrix elements from the valence band states to cb2 and cb3 are considerably larger than those of cb1 and cb4. This has also been explained in terms of a zonefolding picture elsewhere (Froyen et al, 1988).

In fact the vbn-cb1 transitions are seen to have matrix elements which are zero, to four decimal places, indicating that these transitions will not be seen. We are now, therefore, in a position to compare our theoretical results with those of experiment. If we assume that the vb1–cbn and vb2–cbn transitions are 'smeared out' to show just one peak in the electroreflectance spectra – perhaps giving an indication as to why the

half-widths of the experimental spectra are of the order of 0.15eV when the separation of the vb1 and vb2 states is 0.13eV – and take the average energy of the transitions. We find that the five possible transitions have energies centred at 1.02, 1.15, 1.68, 1.94 and 2.45eV. But we may expect the transitions at 1.02 and 1.94eV to be unobservable due to their small matrix elements. This leaves the transitions at 1.15, 1.68 and 2.45eV. These results compare favourably with the experimental results of 1.25±0.13, 1.80[†] and 2.31±0.12 (all in eV), especially when consideration is taken of the calculational errors, as mentioned earlier.

We may ask how the wavefunctions of various states appear in this superlattice. Figure (6.9) shows a plot of the average charge densities for the '0.76' in-plane solution 'cb0' and for cb1 and vb1. Perhaps the main point of interest for the three plots is how localised they appear. In comparison to cb0 and vb1 we see that cb1 is very localised in the silicon – as we might expect with reference to figure (6.8) which shows that cb1 is virtually dispersionless. vb1 is delocalised, with its main contribution in the germanium. cb0, which is only experiencing a potential barrier of 0.17eV, is similarly delocalised with most of its wavefunction residing in the silicon.

The fact that vb1 and cb0 are so delocalised can be considered to be partially as a consequence of the very small barrier widths ($\approx$5.5Å). It can in turn give an indication that we might expect fairly large matrix elements

---

[†] The error for this transition is not recorded in the literature (Hybertsen and Schluter, 1987).

between, say, vb1 and cb0 since there is significant real space overlap. This is very important since, as can be seen from figure (6.7), we are dealing with a type II superlattice which would usually, for larger barrier widths, make the matrix elements very small since the spatial overlap in equation (6.3) would be negligible.

We may now return to the problem of the origin of the 0.76eV transition. As pointed out earlier, with the standard offsets the in-plane non-zonefolded states are lower in energy and in fact are calculated to lie at an energy of 0.144eV which gives a 'smeared' transition energy of 0.806eV. It has been shown that the direct transitions have a one-to-one correspondence with the experimental results, so we are forced to the conclusion that it is this non-zonefolded state which is participating in the transition.

It seems, therefore, that for a Si_4Ge_4 superlattice the 0.76eV transition will be indirect in nature. But what happens when we deal with the finite $(Si_4Ge_4)_5$ structure of experiment? It has been shown (Wong and Jaros, 1988) that the effects of this change makes a negligible difference to both energy transitions and matrix elements. This result is expected to be independent of the method of calculating the bandstructure. Consequently we expect that for the $(Si_4Ge_4)_5$ structure the 0.76eV transition will be indirect.

An explanation of the exact mechanism which is allowing the indirect transition to occur is outside the scope of the present work. The most likely explanation must be that it is caused by a strong electron-phonon interaction.

Since the experiment was done at room temperature there will be no shortage of participating phonons. It would, therefore, be interesting to carry out the electroreflectance experiment at low temperatures to see whether the transition disappeared.

Summary.

In this chapter we have considered the properties of two very different structures consisting of silicon and germanium. The first, a quantum well, showed that the exact form of the bandstructure can have important consequences on the energy levels of a quantum well near the bottom of the conduction band. In particular we have shown that the presence of minima in the bandstructure away from $k = 0$ can actually form 'quasi-degenerate' states which have separations which are oscillatory with the quantum well width.

The other structure investigated consisted of an elemental super-lattice. We have investigated the bandstructure over a wide energy range and also, in order to allow a direct comparison with experiment, a process has been developed whereby the optical matrix element could be calculated giving a straightforward method of determining which transitions are allowed and which are forbidden.

Although the techniques of this thesis have been applied to these two particular structures they (that is the calculation of energy bands, energy levels and matrix elements) can be used for any silicon/germanium structure – in any physical strain configuration (as was shown in chapter 5). In

other words we have developed the means whereby the physical parameters relevant to opto-electronics can be calculated in a simple and accurate way for any Si/Ge structure. (In passing we note that similar techniques can be employed to investigate the opto-electronic properties of III-V structures once the strained, if it is required, bandstructure is known.)

CONCLUSION

Summary.

This thesis has attempted to give a flavour of the possibilities of the complex bandstructure matching technique as applied to low dimensional structures. We have shown how it is possible to first create tailored bulk bandstructure before the method itself is used. Consequently various features of the bandstructure can be produced to a good degree of accuracy. For instance if we wish to consider only the conduction band states of a device or structure then only the effective masses appropriate to that part of the bulk bandstructure need be fitted to experimental results. Whereas in optical transition calculations – as in the $(Si)_4(Ge)_4$ superlattice of chapter 6 – it is more reasonable to concentrate on bandgaps and an overall fit of the bandstructure. Once the bulk bandstructure has been found it has been shown that it is a simple – if computationally laborious – matter to find various properties of the structure. In chapters 3, 4 and 6 we showed how energy states were found. In chapters 4 and 6 we showed how charge densities could be plotted and as a straightforward extension of this in chapter 6 how optical matrix elements could be calculated.

These techniques allowed us to investigate some interesting physics. In chapter 4 we were able to consider the anti-crossing and hybridisation of states with great precision. Also the presence of an asymmetric charge density found in the quantum well as a consequence of hybridisation gave an unexpected example of the quantum mechanical principle of superposition.

In chapter 5 we showed how strain could be incorporated into our calculations allowing us to investigate the technologically important pseudomorphic Si/Ge structures as discussed in chapter 6. This final chapter showed how an indirect material such as Si, when forming a quantum well, could produce quasi-degenerate states with interesting oscillatory – with width – properties and how a calculation of a particular superlattice could model the results of experiment with great accuracy; allowing us to explain the electroreflectance spectrum.

Suggestions for Further Work.

The avenues of research opened up by the complex bandstructure matching technique are numerous, here we give just two.

i) Although little use was made of the fact, the CBMT can be used to calculate in-plane bandstructure for low dimensional structures. The detailed nature of light and heavy-hole bands in a laser and their variation with strain can be very important in the design of quantum well lasers and a systematic approach to a range of strained materials and how their in-plane bandstructure could be 'optimized' would play an important role in real device design.

ii) Because of the strengths of the method, including all the symmetry, non-parabolicities and correct bandgaps (accurate to the bulk bandstructure calculation accuracy), there is no limit to the structures that can be modelled. These include multiple quantum wells, ABCA type superlattices and the effects on such devices of electric fields which, in effect involves

considering many stepped interfaces (Monaghan and Brand, 1987).

Both sections i) and ii) can be achieved with little extension to the theory already given in the thesis and yet give us the possibilities of calculating results which are physically interesting and technologically important.

APPENDIX A

Production Of Complex Bandstructure With Spin.

A method for producing 'spinless' complex bandstructure already exists in the literature (Chung Chang and Schulman, 1982). This appendix will show how the techniques of this paper can be extended to include spin by the inclusion of two extra spin parameters.

In the plane-wave formalism the solutions to the bulk bandstructure problem are found from the matrix equation

$$(\mathbf{H} - E\mathbf{I})\mathbf{\Psi} \qquad\qquad A.1$$

where the eigenvector, $\mathbf{\Psi}$, is formed from the coefficients $a_{\mathbf{G}}$ for spin up and spin down components. The elements of $\mathbf{H}$ are given by

$$H_{\mathbf{G},\mathbf{G}',s,s'} = K^2 \delta_{\mathbf{G},\mathbf{G}'}\delta_{s,s'} + V_L(|\mathbf{G} - \mathbf{G}'|)\delta_{s,s'} + \mathrm{SOC}_{\mathbf{G},\mathbf{G}',s,s'}(\mathbf{K},\mathbf{K}').$$

where $\mathbf{G}=(\mathbf{G}_x,\mathbf{G}_y,\mathbf{G}_z)$ is a reciprocal lattice vector, $\mathbf{K} = \mathbf{q} + \mathbf{G}$, $\mathbf{q}$ is the reduced wave-vector in the first Brillouin zone, V_L is the conventional local pseudopotential term, SOC is the spin-orbit coupling term and s is a spin index.

For a particular $\mathbf{G},\mathbf{G}'$ combination the s,s' terms are taken from the appropriate position within the 2x2 matrix

$$\mathrm{SOC}_{s,s'} = -i\lambda S(\mathbf{G} - \mathbf{G}')\sigma.\mathbf{K} \times \mathbf{K}' \qquad\qquad A.2$$

where the elements of σ are those of the Pauli spin matrices $\sigma_x, \sigma_y, \sigma_z$. $S(\mathbf{G} - \mathbf{G'})$ is a structure factor which reflects the spin-orbit interactions for the individual atoms within the unit cell which we shall discuss in more detail later. λ determines the overall strength of the interaction.

As an example, one of the contributions to SOC originates from the term

$$(\sigma.\mathbf{K} \times \mathbf{K'})_x = \begin{bmatrix} 0 & \frac{1}{2} \\ \frac{1}{2} & 0 \end{bmatrix} [K_y K_z' - K_z K_y']$$

and similarly for the y and z contributions.

Conventionally in bandstructure calculations $\mathbf{q}$ is fixed and E is determined by solving A.1. For the complex bandstructure matching technique, however, E is fixed and $\mathbf{q}$ must be determined. If $\mathbf{q} = (k, \mathbf{q_2})$ where k is the unknown component in the superlattice direction then we can expand A.1 as a polynomial matrix equation in k:

$$(\mathbf{H^0} + k\mathbf{H'} + k^2\mathbf{I})\mathbf{\Psi} = 0 \qquad A.3$$

where the elements of $\mathbf{H^0}$ and $\mathbf{H'}$ are given by

$$H^0_{\mathbf{G},\mathbf{G'},s,s'} = [(\mathbf{q_2} + \mathbf{G_2})^2 + G_x^2 - E]\delta_{\mathbf{G},\mathbf{G'}}\delta_{s,s'} + V_L(|\mathbf{G} - \mathbf{G'}|)\delta_{s,s'}$$

$$- i\lambda S(\mathbf{G} - \mathbf{G'})\sigma.(\mathbf{q^0} + \mathbf{G}) \times (\mathbf{q^0} + \mathbf{G'})$$

with $\mathbf{q^0} = (0, \mathbf{q_2})$, and $\mathbf{G_2} = (G_y, G_z)$. Also;

$$H'_{\mathbf{G},\mathbf{G'},s,s'} = 2G_x \delta_{\mathbf{G},\mathbf{G'}}\delta_{s,s'} - i\lambda S(\mathbf{G} - \mathbf{G'})\sigma.[(G_z - G_z')\mathbf{j} + (G_y' - G_y)\mathbf{k}].$$

Defining $\mathbf{\Phi} = k\mathbf{\Psi}$ then we can write A.3 in another way:

$$\begin{bmatrix} \mathbf{0} & \mathbf{I} \\ -\mathbf{H^0} & -\mathbf{H'} \end{bmatrix} \begin{pmatrix} \mathbf{\Psi} \\ \mathbf{\Phi} \end{pmatrix} = k \begin{pmatrix} \mathbf{\Psi} \\ \mathbf{\Phi} \end{pmatrix} \qquad A.4$$

which can be solved to give k and Ψ for a given E and $\mathbf{q_2}$.

We shall now discuss the method by which the form of SOC in A.2 is represented computationally. From A.2 we have

$$\text{SOC}_{s,s'} = -i\lambda S(\mathbf{G} - \mathbf{G'})\sigma.\mathbf{K} \times \mathbf{K'}.$$

This can be expanded as

$$\text{SOC}_{s,s'} = [-i\lambda^S \cos((\mathbf{G} - \mathbf{G'}).\tau) + \lambda^A \sin((\mathbf{G} - \mathbf{G'}).\tau)][\sigma.\mathbf{K} \times \mathbf{K'}] \qquad A.5$$

(Chelikowsky and Cohen, 1976). Where antisymmetric and symmetric values of λ have been defined such that

$$\lambda^S = \frac{S_\mu(S_\alpha + 1)}{2}$$

and

$$\lambda^A = \frac{S_\mu(S_\alpha - 1)}{2}.$$

It is these spin parameters S_μ and S_α which will be given in appendices B and C.

APPENDIX B

Formfactors for GaAs and AlAs.

The following tables give the symmetric and antisymmetric pseudopotential formfactors for GaAs and AlAs using a 65 plane-wave expansion with spin included (Gell et al, 1986) which are used in chapter 3. The formfactors are given in Rydbergs. The factors S_μ and S_α are additional parameters which regulate the size of spin effects – and in particular S_μ determines the size of the spin split-off separation at the top of the valence band – as explained in appendix A.

GaAs Pseudopotential Formfactors.

	Formfactors
V^S_3	−0.2396
V^S_8	+0.0126
V^S_{11}	+0.0600
V^A_3	+0.0700
V^A_4	+0.0500
V^A_{11}	+0.0100
S_μ	+0.001479
S_α	+1.38

AlAs Pseudopotential Formfactors.

	Formfactors
V^S_3	−0.2307
V^S_8	+0.0254
V^S_{11}	+0.0700
V^A_3	+0.0725
V^A_4	+0.0625
V^A_{11}	−0.0075
S_μ	+0.001382
S_α	+1.38

APPENDIX C

Formfactors for Silicon and Germanium.

The following tables give the symmetric pseudopotential formfactors for silicon and germanium for a 65 plane-wave expansion with spin included. All formfactors are given in Rydbergs the 'gradients' are given in Rydbergs per unit lattice constant. The factors S_μ and S_α regulate the size of spin effects – and in particular S_μ determines the size of the spin split-off separation at the top of the valence band.

Silicon Pseudopotential Formfactors.

	Formfactors
V_3	−0.226
V_8	+0.0488
V_{11}	+0.0777
S_μ	+0.00028
S_α	+1.0

Germanium Pseudopotential Formfactors.

	Formfactors
V_3	−0.2325
V_8	+0.0071
V_{11}	+0.0561
S_μ	+0.00165
S_α	+1.0

The next two tables give the gradients about the points $G^2 = 3, 8$ and 11. Their physical meaning and use are explained in Chapter 5.

Silicon Formfactor Gradients.

	Gradients
G_3	+0.1944
G_8	+0.220
G_{11}	−0.1105

Germanium Formfactor Gradients.

	Gradients
G_3	+0.2750
G_8	+0.1525
G_{11}	−0.010

APPENDIX D

Normalisation of Wavefunctions.

In the calculation of matrix elements in chapter 6 it was assumed that the superlattice wavefunctions being dealt with are normalised, i.e. that

$$O(\psi, \psi) = \int \psi^* \psi d\tau = 1, \qquad\qquad D.1$$

where the integral is taken over an appropriate subsystem of the superlattice. Since some of the Bloch functions which go to make up the superlattice wavefunctions are of a complex nature the exact meaning of (D.1) may be open to question. It will be shown here that the evaluation of (D.1) is actually quite straightforward and well defined, and that it is always possible to redefine ψ such that $O(\psi, \psi) = 1$.

Assuming;

$$\psi = \sum_i \sum_g A_i a_g^i e^{ik_i x} e^{ig \cdot r} e^{ik_2 \cdot r_2}. \qquad\qquad D.2$$

Where we have assumed the notation of chapters 2 and 6 for a (100) superlattice. Inserting (D.2) into (D.1) we can write:

$$M = \int d\tau \sum_i \sum_j \sum_g \sum_{g'} a_g^{i*} A_i^* a_{g'}^j A_j e^{i(k_j - k_i^*)x} e^{i(g' - g^*) r} \qquad D.3$$

Integrating over y and z planes both over, say, L periods.

$$M = \int dx \sum_i \sum_j \sum_g \sum_{g'} a_g^{i*} A_i^* a_{g'}^j A_j e^{i(k_j - k_i^* + g_x' - g_x)x} L^2 (2\pi)^2 \delta_{g_2, g_2'} \qquad D.4$$

Now, (D.4) must be treated carefully since we have terms of the form $k_j - k_i^* + g_x' - g_x$ which may be zero if $k_j = k_i^*$ and $g_x = g_x'$. Nevertheless, we can write

$$M = (2\pi L)^2 \left[\sum_i \sum_j \sum_g \sum_{g'} a_g^{i*} A_i^* a_{g'}^j A_j \delta_{g_2,g_2'} H(x) \right]_{x_1}^{x_2} \qquad D.5$$

where x_1 and x_2 are the x limits of the region over which the integration takes place and

$$H(x) = \frac{e^{i(k_j - k_i^* + g_x' - g_x)x}}{i(k_j - k_i^* + g_x' - g_x)}, \qquad \text{if } k_j - k_i^* + g_x' - g_x \neq 0$$

$$H(x) = x, \qquad \qquad \text{if } k_j - k_i^* + g_x' - g_x = 0 \qquad D.6$$

The expressions (D.5) and (D.6) allow M to be calculated and so a normalised function of the form

$$\psi_{\text{normal}} = \frac{\psi}{\sqrt{M}}$$

where ψ is defined in (D.2) and $O(\psi_{\text{normal}}, \psi_{\text{normal}}) = 1$.

APPENDIX E

Computational Details.

In chapter 2 a rather abstract and mathematical approach was given to the bandstructure matching technique. Since any real calculation based on this method must be carried out computationally in this appendix two of the main numerical methods used to make the calculations solvable and efficient will be given.

Number of Basis Functions.

With a 65 plane wave expansion it is possible to fold the 65 g's down to 25 two dimensional g's per spin orientation (where we use the notation of chapter 2). The question arises whether it is necessary to use all 25 two dimensional g's in order to model the low dimensional structures accurately or is it sufficient to use a subset of the g_2's? There are two competing aspects to this problem:

(i) The number of g_2's used determines the number of bulk wavevectors used in the LDS wavefunction expansion as explained in chapter 2. If all 25 g_2's are used it will necessitate using values of wavevector which have large decay constants and which will not be expected to contribute to the wavefunctions since they will have decayed away to very small values over a short range.

(ii) In certain cases, such as when we deal with states coming from

the X-minima in the conduction band we may expect that the overall p-like nature of the minimum will require higher order components of g – in the extreme case, for example, we would not expect the (0,0) g_2 to be able to model the odd parity of a p-state.

It turns out that the number of g_2's which must be used can be reduced. Because of the point raised in the previous paragraph we expect the minimum usable number to be material dependent, but for a straightforward GaAs/AlGaAs(direct gap material) it is actually possible to reduce the number of g_2's to 5 with less than a 4meV change in any conduction band state. This not only allows a great saving in computing time – since numerical subroutines such as the 'NAG-library' used for this work increase in running time with the cube of the order of the determinant or matrices being evaluated – but also tends to decrease the possibility of serious rounding errors associated with the calculation.

Limiting Exponentials.

Since the complex bandstructure matching technique produces terms which are of the form e^{ikw} with k imaginary it is possible to have terms in the various sums of chapter 2 such as 2.19 and 2.23 which have very large components. These large values can cause numerical difficulties. These problems have been noted by other workers (Mailhiot and Smith, 1986) who have used various rearrangement techniques to solve the problem. In this work we have taken a more straightforward and pragmatic approach based on physical understanding. Any state which has an imaginary component

of wavevector decays away from an interface. If the imaginary part of k is large for a particular bulk solution the exponential term will fall to a very small value a short distance from the interface. In a sense, then, this term does not 'see' any other interface and will not contribute to the energy of the eigenstate or the form of the wavefunction to any extent away from the interface.

Consequently we do not expect the exact value of kw to be crucial in the detailed calculation. This idea is introduced into our method by replacing e^{ikw} – where k is imaginary – by e^{LIM} where LIM is a value chosen to eliminate the computational problems but not significantly affect the quantum well solutions.

An investigation of the effect of using various values of LIM was carried out on the conduction band states of an AlGaAs quantum well. It was found that for values of $5 < LIM < 30$ the same energy solutions were obtained with increasingly worse results being obtained as we move further outside this range. For much of the work carried out in this thesis the value of LIM chosen was 10 although for each new calculation – as in the case of determining how many g_2's to use – an initial investigation must be carried out to evaluate the optimum value.

REFERENCES

Arthur J.R.,
1968, J. Appl. Phys., **39**, 4032.

Aspnes D.E.,
1973, Surface Science, **37**, 418.

Aspnes D.E.,
1980, Handbook of Semiconductors, North Holland Publishing.

Aspnes D.E. and Studna A.A.,
1973, Phys. Rev. B., **7**, 4605.

Aspnes D.E., Olsen C.G. and Lynch D.W.,
1976, Phys. Rev. Lett., **37**, 766.

Barber H.D.,
1967, Solid State Electron., **10**, 1039.

Bassani F. and Brust D.,
1963, Phys. Rev., **131**, 1524.

Bastard G.,
1981, Phys. Rev. B., **24**, 5693.

Bastard G.,
1985, Superlattices and Microstructures, **1**, 265.

Batey J. and Wright S.L.,
1985, J. Appl. Phys., **59**, 200.

Bean J.C., Feldman L.C., Fiory A.T, Nakahara S. and Robinson I.K,
1984, J. Vac. Sci. Technol., **A2**, 436.

Bimburg D., Bludau W., Linnebach R. and Bauser E.,
1981, Solid State Commun., **37**, 987.

Brand S. and Abram R.A.,
1983, J. Phys. C., **16**, 6111.

Brand S. and Hughes D.T.,
1987, Semicond. Sci. Technol., **2**, 607.

Brand S., Monaghan S. and Szydlik P.P.,
1987, Semicond. Sci. Technol., **2**, 123.

Braunstein R., Moore A.R. and Herman F.,
1958, Phys. Rev., **109**, 695.

Braunstein R. and Kane E.O.,
1962, J. Phys. Chem., **23**, 422.

Brey L. and Tejedor C.,
1987, Phys. Rev. Lett., **59**, 1023.

Burt M.G. and Inkson J.C.,
1976, J. Phys. D., **9**, 45.

Cardona M., Suemoto T., Christensen N.E., Isu T. and Ploog K.,
1987, Phys. Rev. B., **36**, 5906.

Chelikowsky J.R and Cohen M.L.,
1976, Phys. Rev. B., **14**, 556.

Ciraci S. and Batra I.P.,
1988, Phys. Rev. B., **38**, 1835.

Chung-Chang Y. and Schulman J.N.,
1982, Phys. Rev. B., **25**, 3975.

Chung-Chang Y. and Schulman J.N.,
1985, Phys. Rev. B., **31**, 2069.

Cohen M.L. and Heine V.,
1970, Solid State Physics, vol. 24, Academic Press.

Cornwell J.F.,
1969, Group Theory and Electronic Energy Bands, North-Holland Publishing.

Dawson P., Duggan G., Ralph H.I., Woodbridge K. and t'Hooft G.W.,
1985, Superlattices and Microstructures, **1**, 231.

De Sterke C. M. and Hall D.G.,
1987, Phys. Rev. B., **35**, 1380.

Dexter R.N., Zeiger H.J. and Lax B.,
1956, Phys. Rev., **104**, 637.

Dingle R., Wiegmann W. and Henry C.H.,
1974, Phys. Rev. Lett., **33**, 827.

Dumke W.P., Lorenz M.R. and Pettit G.D.,
1972, Phys. Rev. B., **5**, 2978.

Esaki L. and Tsu R.,
1970, IBM J. Res. Develop., **14**, 61.

Esaki L. and Chang L.L,
1974, Phys. Rev. Lett., **33**, 495.

Feher G.,
1959, Phys. Rev., **114**, 1219.

Ferraz A.C. and Srivastava G.P.,
1986, Semicond. Sci. Technol., **1**, 169.

Fink D. and Braunstein R.,
1976, Phys. Status Soldi b, **73**, 361.

Froyen S., Wood D.M. and Zunger A.,
1988, Phys. Rev. B., **37**, 6893.

Gell M.A., Ninno D., Jaros M, Herbert D.C.,
1986, Phys. Rev. B., **34**, 2416.

Gilbert T.G, and Gurman S.J.,
1987, Superlattices and Microstructures, **37**, 6893.

Goroff I. and Kleinman L.,
1963, Phys. Rev., **132**, 1080.

Groves S.H.,
1966, Phys. Rev. Lett., **17**, 643.

Heine V.,
1963, Proc. Phys. Soc., **81**, 300.

Hensel, J.C., Hasegawa H. and Nakayama M.,
1965, Phys. Rev., **138**, A225.

Hughes D.T.,
1987, Report produced for internal distribution at R.S.R.E. Malvern.

Hughes D.T. and Brand S.,
1987, Journal de Physique, **C5**, 565.

Hughes D.T. and Brand S.,
1989, Superlattices and Microstructures, **5**, 185.

Hull R., Bean J.C, Cerdeira F., Fiory A.T. and Gibson J.M.,
1986, Appl. Phys. Lett., **48**, 56.

Hybertsen M.S. and Schluter M.,
1987, Phys. Rev. B., **36**, 9683.

Inkson J.C.,
1986 Proceedings of the SERC LDS Summer School.

Ishibashi A., Mori Y., Itabashi M. and Watanabe M.,
1985, J. Appl. Phys., **58**, 2691.

Kamimura H. and Nakayama T.,
1987, Comments Cond. Mat. Phys., **13**, 143.

Kane E.D.,
1956, J. Phys. Chem. Solids, **1**, 83.

Ko D. and Inkson J.N.,
1988, Semicond. Sci. Technol., **3**, 7691.

Ko D. and Inkson J.N.,
1987, Semicond. Sci. Technol., **2**, 442.

Kroemer H., Wu-Yi Chien, Harris J.S. and Edwall D.D.,
1980, Appl. Phys. Lett., **36**, 295.

Lee S., Sanchez-Dehesa J. and Dow J.D.,
1985, Phys. Rev. B., **32**, 1152.

Macfarlane G.G., Mclean T.P., Quarrington J.E. and Roberts V.,
1957, Phys. Rev., **108**, 1377.

Mailhiot C., McGill T.C. and Smith D.L.,
1984, J. Vac. Sci. Technol., **B2**, 371.

Mailhiot C and Smith D.L,
1986, Phys. Rev. B., **33**, 8360.

Manasevit H.M.,
1968, Appl. Phys. Lett., **12**, 136.

Marsh A.C. and Inkson J.C.,
1986, Semicond. Sci. Technol., **1**, 285.

Martinez G.
1980, Handbook of Semiconductors, North Holland Publishing.

Miller R.C., Gossard A.C., Tsang W.T. and Munteanu O.,
1982, Phys. Rev. B., **25**, 3871.

Miller R.C. and Kleinman D.A.,
1985, J. Luminescence., **30**, 520.

Monaghan S. and Brand S.,
1987, Superlattices and Microstructures, **3**, 697.

Monemar B.,
1973, Phys. Rev. B., **8**, 5711.

Moore K.J., Duggan G., Dawson P. and Foxon C.T.,
1988, Phys. Rev. B., **38**, 5535.

Morrison I., Jaros M. and Wong K.B.,
1986, J. Phys. C., **19**, L239.

Mukherji D. and Nag B.R.,
1975, Phys. Rev. B., **12**, 4338.

Murnaghan F.D.,
1944, Proc. Nat. Acad. Sci., **30**, 244.

Nara S.,
1987, Jap. Journ. Appl. Phys., **26**, 690.

Ninno D., Gell M.A. and Jaros M.,
1986, J. Phys. C., **19**, 3845.

Onton A.,
Proc. 10th Int. Conf. Phys. Semicond. 1970.

O'Reilly E.P.,
1986, Semicond. Sci. Technol., **1**, 128.

O'Reilly E.P. and Witchlow G.P.,
1987, Solid State Commun., **62**, 653.

Parker G.H. and Mead C.A.,
1968, Phys. Rev. Lett., **21**, 605.

Pearsall T.P., Bevk J., Feldman L.C., Bonar J.M., Mannaerts J.P. and Ourmazd A.,
1987, Phys. Rev. Lett., **58**, 729.

People R.,
1986, Journal of Q.E., **22**, 1696.

People R. and Bean J.C.,
1985, Appl. Phys. Lett., **47**, 322.

People R. and Jackson S.A.,
1987, Phys. Rev. B., **36**, 1310.

Podgorny M., Wolfgarten G. and Pollmann J.,
1986, J. Phys.C., **19**, L141.

Sari S.O. and Schnatterly S.E.,
1973, Surface Science, **37**, 328.

Schiff L.I.,
Quantum Mechanics, 1949, McGraw-Hill.

Schulman J.N. and McGill T.C.,
1981, Phys. Rev. B., **23**, 4149.

Sturge M.D.,
1962, Phys. Rev., **127**, 649.

Szydlik P.P.,
1986 Private Communication.

Tamm I.,
1932, Phys. Z. Sowjet, **1**, 732.

Taylor R.I.,
Ph.D. Thesis. University of Durham, 1987.

Taylor R.I. and Burt M.G.,
1987, Semicond. Sci. Technol., **2**, 485.

Van de Walle C.G. and Martin R.,
1986, Phys. Rev. B., **34**, 5621.

Weimann G and Schlapp W.,
1985, Appl. Phys. Lett., **46**, 411.

Welber B., Kim C.K., Cardona M. and Rodriguez S.,
1975, Solid State Commun., **17**, 1021.

Wong K.B. and Jaros M.,
1988, Appl. Phys. Lett., **53**, 657.

Wong K.B., Jaros M., Morrison I. and Hagon J.P.,
1988, Phys. Rev. Lett., **60**, 2221.

Zallen R. and Paul W.,
1967, Phys. Rev., **155**, 703.

Zwerdling S., Button K.J., Lax B. and Roth L.M.,
1960, Phys. Rev. Lett., **4**, 173.